Raman Spectroscopy Characterization of Anharmonicity

and Alloying Effects in Semiconductor Materials

by

Sampriti Bagchi

A Dissertation Presented in Partial Fulfillment
of the Requirements for the Degree
Doctor of Philosophy

Approved September 2011 by the
Graduate Supervisory Committee:

José Menéndez, Chair
Michael Treacy
Fernando Ponce
Kong-Thon Tsen
Peter Rez

ARIZONA STATE UNIVERSITY

December 2011

ABSTRACT

The chemical sensitivity and spatial resolution of Raman spectroscopy, combined with the sensitivity of modern systems that can easily detect single atomic layers, have made this technique a preferred choice for the strain characterization of complex systems such as nanoscale complementary metal-oxide-semiconductor - CMOS - devices. A disadvantage of Raman spectroscopy, however, is that the shifts associated with strain are not related to the geometrical deformations in any obvious way, so that careful calibrations are needed to determine the anharmonic coefficients (p, q and r) that relate strain to Raman shifts. A new set of measurements of the Raman shift in strained Ge films grown on relaxed SiGe buffer layers deposited on Si substrates is presented, and thereby, a new consistent set of values for the parameters p and q for Ge has been proposed.

In this dissertation the study of the vibrational properties of $Ge_{1-x}Sn_x$ alloys has also been reported. The temperature dependence of the Raman spectrum of Ge-rich Ge_{1-x} Sn_x and $Ge_{1-x-y}Si_{x}Sn_y$ alloys has been determined in the 10 K - 450 K range. The Raman line shift and width changes as a function of temperature are found to be virtually identical to those observed in bulk Ge. This result shows that the anharmonic decay process responsible for the temperature dependence is extremely robust against the alloy perturbation.

for my grandparents,

my dadu, dida and thakurma

who would take pride in every small step I took……

ACKNOWLEDGMENTS

I would like to express my deepest appreciation and thanks to my guide and advisor, Dr. José Menéndez, for his guidance throughout the duration of my stay at ASU. He not only supported me in my research but also on a personal level. He was always there for me whenever I needed him.

I am extremely grateful to Dr. Christian Poweleit for providing me with all the training and continuous assistance for running the experiments. Without him my research would not have been possible.

I would like to thank Dr. Fernando Ponce and Dr. Michael Treacy for providing me with confidence and believing in me. They would get my spirits up in the event of any eventuality. Dr. K. T. Tsen deserves a special mention for stepping in at the last minute and being on my committee. I thank Dr. Peter Rez for his counseling and guidance in writing my thesis.

I am grateful to Dr. John Kouvetakis and his group for providing me with samples. I also gratefully acknowledge the use of facilities within the Leroy Eyring Center for Solid State Science at ASU.

Also, I would like to thank my fellow researchers and friends Dr. Rachna Singh, Dr. Jay Mathews and Dr. Hermann A. Donfack for helping with the physics and for always being there.

Finally, I would like to thank my husband Sandeep, for all his support during this journey (especially with the monumental task of formatting this thesis)

and my children Jigisha and Anusha for the many sacrifices they have made so that I could finish my work. I would also like to thank my parents and my sisters for their encouragement, understanding and support during this endeavor.

TABLE OF CONTENTS

Page

LIST OF TABLES…………………………………………………....……..viii

LIST OF FIGURES…………………………………………………………ix

CHAPTER

1 INTRODUCTION…………………….……………........................1

1.1 Motivation of the Study……………..……...……................1

1.2 Dissertation Outline…..……………….………...............4

2 CHARACTERIZATION OF SEMICONDUCTORS USING RAMAN SPECTROSCOPY.....………………………….................6

2.1 Introduction…...6

2.2 Phonons in Semiconductors……………………….........6

2.3 Anharmonic Effects on Raman-active honons…………...13

2.4 Raman Scattering by Phonons...….……………….........14

2.5 Effect of Perturbations on Vibrations…………………....19

2.6 Effect of Strain on Raman Phonons…………….............21

2.7 Effect of Alloying on Raman Phonons…………………..22

3 PHONON STRAIN-SHIFT COEFFICIENT IN Si AND Ge........25

3.1 Introduction……………………………….…….............25

3.2 Definition of Basic Parameters…………….…….……..28

3.3 Pressure and Stress Experiments……………….……............34

CHAPTER Page

3.4 Strain Experiments……………………………………….……36

3.5 Application to Silicon……………………………………40

3.5.1 Grüneisen Parameter..…………………………........40

3.5.2 Uniaxial Stress Experiments..…......…...……......44

3.5.3 Strain Experiments……………………..............46

3.6 Application to Germanium………………………………50

3.6.1 Grüneisen Parameter……………………………..50

3.6.2 Uniaxial Stress Experiments……………….……52

3.6.3 Previous Strain Experiments……………..........53

3.7 Theory………...……………………………………….……53

3.8 Reconciliation of p, q and r..55

3.9 Our Strain Experiment…..……………………….............57

3.10 Conclusion.....………………………………………..........65

4 VIBRATIONAL PROPERTIES OF GeSn ALLOYS…………...67

4.1 Introduction……………………………………...............67

4.2 Germanium…..……...………………...…...…....………68

4.3 GeSn Alloys……………………………………............72

4.4 Structural Effects in GeSn Alloys…………………......74

4.5 Experimental Details…………………………….……75

4.6 Results………………………………………………………75

4.7 Conclusions…………………………………………………85

CHAPTER Page

5 TEMPERATURE DEPENDENCE OF THE RAMAN MODES IN GeSn AND SiGeSn ALLOYS……………………...86

5.1 Introduction……………………………………............86

5.2 Alloy Vibrational Structure……………………............87

5.3 Experiment………………………………………………90

5.4 Results……………………………………………………90

5.5 Conclusion………………………………………………96

6 CONCLUSIONS…………………………………………….....98

6.1 Introduction……………………………………............98

6.2 Strain-Shift Coefficient……………………………..........98

6.3 Vibrational Properties of GeSn Alloys…………………..98

REFERENCES……………………………………..........………………..101

APPENDIX

A Permissions for Reprinted Materials….…………………….…..107

LIST OF TABLES

Table Page

3.1 Currently Recommended Values for Deformation Potentials *p*, *q* and *r*……………………………………………………………….........28

3.2 Elastic Constants for Si and Ge………………………………….……...........38

3.3 Strain-shift coefficient in Si from literature…………………....……......47

3.4 Recommended values of the Grüneisen parameter γ, shear phonon deformation potential (a_s), and deformation potentials *p*, *q* and *r*….........56

3.5 Ge compositions and layer thicknesses……………………………..........61

LIST OF FIGURES

Figure Page

2.1 Ge phonon dispersion relation………………………………………..........13

3.1 Fitting a straight line (thick line) to the pressure dependent Raman shift of Si measured at room temperature by Weinstein………………........41

3.2 Dependence of frequency-shift on volume based on Hu et al's study of the p-V relationship experimentally……………………………..........43

3.3 Plot of $d\omega/\omega$ versus $\Delta V/V_0$ for strained Si grown on SiGe. The measurements were made by Nakashima et al…………………….........48

3.4 Linear fit to the Ge mode measured by Olego at room temperature..........51

3.5 Plot of $d\omega/\omega$ versus $\Delta V/V_0$ for strained Ge grown on SiGe. The measurements were made by Menoni et al……………………………........52

3.6 Schematic diagram of the sample……………………………………...........58

3.7 Schematic Raman experimental setup……………………………...........59

3.8 Raman spectra of bulk unstrained Ge and compressively strained Ge deposited on a relaxed SiGe (57 %) Ge layer………………….........60

3.9 Raman spectra of the Ge LO phonon from the various strained Ge caps deposited on relaxed SiGe buffer layers…………………………........62

3.10 Schematic diagram of X-ray optics for in-plane diffraction……….........63

3.11 Plot of the strain-induced Raman shift of the Ge-Ge LO phonon in strained Ge………………………………………………………….........64

Figure Page

4.1 Electronic band structure of Ge……………………………………….........69

4.2 (a) Transition from indirect to direct band gap in Ge with the application of biaxial tensile strain. (b) Energy gaps in Ge at the Γ- and L- points as a function of tensile strain…………………….............71

4.3 Electronic band structure of α-Sn………………………………….........73

4.4 Raman spectra of $Ge_{0.985}Sn_{0.015}$ alloy in z (x, y) $\bar{z}$ geometry………..........76

4.5 Raman spectra of $Ge_{0.985}Sn_{0.015}$ alloy in z (x, x) $\bar{z}$ geometry………..........77

4.6 Normalized Ge-Ge mode in $Ge_{1-x}Sn_x$ alloys...79

4.7 Dependence of Ge-Ge mode in $Ge_{1-x}Sn_x$ alloys on Sn concentration.......81

4.8 (a) Plot of the asymmetry in the lineshapes as a function of Sn concentration and (b) Plot of the difference between the linewidths of the Ge-Ge Raman peaks and bulk Ge……………………….............84

5.1 Calculated phonon density of states and *frequency- resolved final state spectrum* for Ge…………………………………………….........89

5.2 Raman spectrum of GeSn obtained with 532 nm excitation at temperatures 10K, 200K and 400K…………………………….............91

5.3 (a) Linewidths for Ge, GeSn and SiGeSn as a function of temperature. (b) Linewidth difference between GeSn and Ge and between SiGeSn and Ge……….……………..................……………………….............92

5.4 (a) Peak frequencies ω(*T*) of the Raman modes in Ge, GeSn and SiGeSn as a function of temperature *T*. (b) Line shift difference

Figure		Page

between GeSn and Ge and between SiGeSn and Ge....................................93

5.5 Plot of the difference between the linewidths of the Ge-Ge Raman peaks and bulk Ge and plot of the asymmetry in the lineshapes as a function of Sn concentration..95

CHAPTER 1

INTRODUCTION

1.1 Motivation of the Study

Silicon technology has been dominating the semiconductor industry in high-speed microelectronics[1] and optoelectronic[2] applications, excluding direct-gap applications. Group-IV alloys, namely GeSi, have played a pivotal role in the growing field of Si photonics [3] and commercial microprocessors[4]. Because of the ease with which these alloys can be grown epitaxially on Si and the low cost of Si substrates, these alloys are preferred over group-III-V alloys of comparable functionality[5]. Modern semiconductor optoelectronic devices are almost all made by heterostructures which are accompanied by strain[6]. Earlier efforts focused on reducing the strain to eliminate device degradation. But as the film growth technology has advanced and device sizes have shrunk, strain effects are found to be a useful tool to change the optoelectronic device characteristics and enhance their performance through its effects on the band structure.

Strain engineering applications of GeSi alloys are possible due to the large lattice mismatch between Ge and Si. Strain engineered GeSi structures improve carrier mobilities resulting in increased device speeds. GeSi virtual substrates[7, 8] are an excellent platform for integration of high speed heterostructure metal-oxide-semiconductor field-effect transistors – MOSFETs - onto silicon substrates. By using strained Si layers grown upon a relaxed SiGe buffer layer, mobility enhancements over bulk Si of roughly 80% for electrons[9] and 60% for holes[10] are

attainable. Whereas strained Ge layers grown on a relaxed SiGe substrate have shown a hole mobility enhancement of nearly eight times that of co-processed bulk Si devices[11].

Raman scattering is a useful technique for characterizing strain in compound semiconductor microstructures[12]. But for an accurate characterization, one needs to know the *phonon deformation potentials* (DPs), or *the strain-shift coefficient*. DPs are the derivative of the optical phonon frequency with respect to an elastic deformation of the lattice. The strain-shift coefficient for the Raman-active mode has been extensively measured in Si[13,14]. However, little work has been done for its Ge counterpart. The only published work we are aware of is that of Pezzzoli et al[15] at very low strain levels. Part of this thesis will focus on determining the strain-shift coefficient of the Raman mode of Ge at strain levels comparable to those of technological interest.

The large lattice mismatch between Si and Ge also leads to unmanageable strain effects when Ge is grown directly on Si substrates. In photovoltaic applications where thick Ge layers need to be incorporated, the generation of strain-relieving threading dislocations is a deterrent as it degrades device performance. Further, in near-IR detectors (which are of current interest in the industry) targeting the 1.53 – 1.68 μm spectral range, pure Ge-on-Si is in principle an excellent candidate, but due to its lattice mismatch with Si, it is difficult to grow defect-free films. In addition, Ge is an indirect band gap material. Its direct gap absorption edge lies outside the spectral range of the near-

IR detectors. Hence the industry has been on the lookout for alternatives. Recently Bauer et al[16] have grown single crystals of GeSn alloys directly on Si using ultrahigh vacuum CVD. The large lattice mismatch with the Si substrate is accommodated by Lomer-type edge dislocations. These films are fully compatible with complementary metal-oxide-semiconductor -CMOS- devices. Unstrained $Ge_{1-x}Sn_x$ alloys are predicted to exhibit a direct band gap with increasing Sn composition. The addition of Sn into Ge decreases the direct band gap systematically with increasing Sn concentration[17]. Hence, the electrical and optical properties of such alloys can be controlled over a wide range of compositions[18]. The indirect to direct transition is estimated to be at $x = 0.1$[19]. Mathews et al[20] have shown that with the presence of tensile strain the Sn composition required for the crossover point can be reduced. Hence, to engineer the optical properties of the $Ge_{1-x}Sn_x$ alloys, one should be able to determine the strain and Sn composition accurately. Since optical phonon modes of these alloys are affected by the strain and composition, an optical characterization technique, such as Raman spectroscopy seems an ideal technique for this purpose. In this thesis we have measured the compositional dependence of the Ge-Ge mode of the Raman spectrum of the $Ge_{1-x}Sn_x$ alloy.

For device manufacturers heating is a source of major concern as a cause of device failure. Measurement of the local temperature rise is of great significance. Since Raman frequency and linewidth are strongly temperature dependent[21], these can be used as parameters for temperature measurements with

great simplicity and accuracy. We have measured the temperature dependence of the lineshifts and linewidths of Ge, GeSn and SiGeSn.

1.2 Dissertation Outline

Chapter 2 reviews the vibrational properties of semiconductors. The theory of Raman scattering is explained using the classical and semi-classical approach. The effect of perturbations, including alloying and strain effects, on vibrational properties is also discussed.

In chapter 3 we have discussed the LO phonon modes in strained Ge grown on relaxed SiGe. The strain induced shift of the Raman frequency and the corresponding x-ray strain measurements have been used to calculate the strain-shift coefficient for the Ge-Ge mode in pure Ge.

Chapter 4 discusses the vibrational properties of GeSn alloys. The Raman spectrum of each GeSn sample shows a strong peak corresponding to the Ge-Ge phonon mode. We also observe the disorder-activated (DA) Ge-Ge mode in the $z(x, x)\bar{z}$ geometry. We have studied the compositional dependence of the Ge-Ge mode which can be explained in terms of bond distortion and mass perturbation.

The temperature dependence of the lineshifts and the linewidths of the LO phonon in GeSn and SiGeSn is discussed in chapter 5. This temperature dependence is the result of anharmonicity. The anharmonic decay of optical phonons implies that when an optical phonon of frequency ω decays into two phonons of frequencies ω_1 and ω_2, the linewidth contains a temperature dependent factor. We find that the temperature dependence of the Raman width and shift is

the same, within experimental error, as the temperature dependence observed in bulk Ge.

Chapter 6 summarizes the results of the strain-shift coefficient of the Ge-Ge mode in pure Ge and the vibrational properties of the GeSn alloys along with their temperature dependence.

CHAPTER 2

CHARACTERIZATION OF SEMICONDUCTORS USING RAMAN SPECTROSCOPY

2.1 Introduction

Inelastic light scattering is a highly attractive tool for the characterization of semiconductors because of its contactless and non-destructive nature. The polarization properties, frequencies and intensities of semiconductor Raman spectra is used for the identification of materials and their crystalline structure, measurements of stress and strain, studying doping levels and alloy semiconductors.

This chapter aims to explain the capabilities of Raman scattering as a characterization tool for semiconductors. The beginning section of this chapter defines the basic concepts of lattice dynamics and Raman spectra in semiconductors. This is followed by sections describing the applications relevant to this thesis.

2.2 Phonons in Semiconductor

The vibrations of atoms about their equilibrium positions determine many of the physical properties of crystals. The vibrational properties of atoms derive from the many-electron states. For non-metallic systems, electronic and vibrational energies are well separated. Vibrational energies are typically about 25 meV at room temperature whereas the lowest electronic energies are about 1 eV (in Si and Ge). Hence the Born-Oppenheimer approximation can be used to

describe the eigenstates of such systems as products of coupled vibrational and electronic states:

$$\Psi_{n\nu}(\boldsymbol{x},\boldsymbol{u}) = \phi_n(\boldsymbol{x},\boldsymbol{u})\Psi_{n\nu}(\boldsymbol{u}) \tag{2.1}$$

where ν and *n* are the vibrational and electronic quantum numbers respectively. The many-electron states $\Phi_n(\boldsymbol{x},\boldsymbol{u})$ depend parametrically on the atoms' displacements, represented collectively by $\boldsymbol{u}$, and on the electronic coordinates $\boldsymbol{x}$. These states are eigenfunctions of the many electron problem for fixed atomic configuration $\boldsymbol{u}$:

$$[T_E + V_{EE}(\boldsymbol{x}) + V_{\boldsymbol{EN}}(\boldsymbol{x},\boldsymbol{u}) + V_{\boldsymbol{NN}}(\boldsymbol{u})]\,\phi_n(\boldsymbol{x},\boldsymbol{u}) = \mathrm{E}_n(\boldsymbol{u})\phi_n(\boldsymbol{x},\boldsymbol{u}) \tag{2.2}$$

where T_E is the electronic kinetic energy operator and $V_{NN}(\boldsymbol{u})$ is the nuclear-nuclear potential energy operator. Then, assuming that as the atoms move, the system remains in its many-electron ground state, the vibrations are determined by taking the effective potential energy function (the crystalline potential) for the atoms to be equal to the many-electron ground state energy eigenvalue

$$\mathrm{V}(\mathbf{u}) \equiv \mathrm{E}_0(\mathbf{u}) \tag{2.3}$$

The atomic equilibrium configuration is defined by the minimum of V. The atoms' displacements from equilibrium are given by the 3n x N dimensional displacement vector

$$\mathbf{u} \equiv \{\mathrm{u}_\alpha(\ell k)\} \tag{2.4}$$

where ℓ = 1,…., N labels the unit cells of the system, *k* labels each atom in the unit cell and α denotes the atomic position (*x*, *y* or *z*) of each atom in this cell.

For small displacements, the total crystalline potential can be expanded about the equilibrium lattice configuration in a Taylor series as:

$$V = V_0 + \sum_{\ell k \alpha} \frac{\partial V}{\partial u_\alpha(\ell, k)}\bigg|_0 u_\alpha(\ell, k) + \frac{1}{2}\sum_{\ell k \alpha}\sum_{\ell' k' \beta} \frac{\partial^2 V}{\partial u_\alpha(\ell, k)\partial u_\beta(\ell', k')}\bigg|_0 u_\alpha(\ell, k) u_\beta(\ell', k') + \ \dots \tag{2.5}$$

At equilibrium the sum of the forces acting on the system must be zero. Hence,

$$\sum_{\ell k \alpha} \frac{\partial V}{\partial u_\alpha(\ell, k)}\bigg|_0 = 0 \tag{2.6}$$

Also, V_0 does not affect vibrations (it represents the binding energy of the crystals) and hence can be set to zero. So the quadratic term is the first non-vanishing term in the crystal potential. The cubic and other higher order terms are the anharmonic terms in the potential. Thus, within the harmonic approximation, the potential energy of the system is given by

$$V = \frac{1}{2}\sum_{\ell k}\sum_{\ell' k'} \phi_{\alpha\beta}(\ell k, \ell' k') u_\alpha(\ell, k) u_\beta(\ell', k') \tag{2.7}$$

where $\mathbf{\Phi}$ is the 3Nn x 3Nn interatomic force-constant matrix, with the derivatives evaluated at the equilibrium configuration $u = 0$

$$\mathbf{\Phi} \equiv \left\{ \phi_{\alpha\beta}(\ell k, \ell' k') = \frac{\partial^2 V(u)}{\partial u_\alpha(\ell, k)\partial u_\beta(\ell', k')}\bigg|_0 \right\} \tag{2.8}$$

V(u) is the crystalline potential and the atomic displacements are represented collectively by u.

Then the vibrational Hamiltonian is given by

$$H = \frac{1}{2}(\boldsymbol{p}^{+}\boldsymbol{M}^{-1}\boldsymbol{p} + \boldsymbol{u}^{+}\boldsymbol{\Phi}\boldsymbol{u}) \qquad (2.9)$$

where the diagonal matrix

$$\boldsymbol{M} = m_k \delta_{ll'} \delta_{kk'} \delta_{\alpha\beta} \qquad (2.10)$$

contains the atoms' masses with m_k being the mass of the k_{th} atom and **p** contains their momenta.

Under the harmonic approximation the equations of motion for the atoms are given by

$$m_k \ddot{u}_\alpha(\ell, k) = -\frac{\partial V}{\partial u_\alpha(\ell, k)}$$

$$= -\sum_{\ell' k' \beta} \phi_{\alpha\beta}(\ell k, \ell' k') u_\beta(\ell', k') \qquad (2.11)$$

Assuming a plane wave solution of the form

$$u_{\ell k}(\boldsymbol{q}, \omega) = u_{\ell k} exp\{i[\boldsymbol{q}.\boldsymbol{R}(\ell) - \omega t]\} \qquad (2.12)$$

the normal mode frequencies are the solutions of the eigenvalue problem

$$(\boldsymbol{\Phi} - \omega_f^2 \boldsymbol{M})\boldsymbol{\psi}(f) = 0 \qquad (2.13)$$

where $\boldsymbol{\psi}(f) = \psi(\ell\alpha|f)$ is the eigenvector corresponding to lattice motion with frequency ω_f where f = 1,……,3Nn represents the modes ,$\boldsymbol{\Phi}$ is the 3nN x 3nN force constant matrix, and **M** is the diagonal matrix as defined in equations 2.8 and 2.10 respectively.

Since both the force constant and mass matrices are real and symmetric, the eigenvectors of equation 2.13 satisfy the completeness and orthonormality conditions with respect to **M**:

$$\sum_{f=1}^{3nN} \boldsymbol{M}\,\boldsymbol{\psi}(f)\boldsymbol{\psi}^{+}(f) = \boldsymbol{I} \tag{2.14}$$

and

$$\boldsymbol{\psi}^{+}(f\,)\boldsymbol{M}\boldsymbol{\psi}(f') = \delta_{ff'} \tag{2.15}$$

so that the 3nN dimensional displacement vector $\boldsymbol{u}$ can be written as a linear combination of these eigenvectors through

$$\boldsymbol{u} = \sum_f \boldsymbol{\psi}(f) Q_f \tag{2.16}$$

where Q_f are the normal coordinates of the system and are defined as

$$Q_f = \psi^{+}(f)\boldsymbol{M}\overline{\boldsymbol{u}} \tag{2.17}$$

Using equations 2.13, 2.15 and 2.16, it can be shown that the Hamiltonian for the lattice is given by

$$H = \frac{1}{2}\sum_f\left(\dot{Q}_f^2 + \omega_f^2 Q_f^2\right) \tag{2.18}$$

The normal coordinate transformation is valid in both the classical and quantum mechanical treatment of the vibrational problem. This is the classical case and describes a collection of independent harmonic oscillators. The equation of motion in normal coordinates becomes

$$\ddot{Q}_f + \omega_f^2 Q_f = 0 \tag{2.19}$$

In the quantum mechanical case, Q_f and $\dot{Q}_f$ are considered as operators satisfying commutation relations $[Q_f, \dot{Q}_{f'}] = i\hbar\delta_{ff'}$. The vibrational Hamiltonian can be written as

$$H = \sum_f \hbar\omega_f \left(a_f^{+} a_f + \frac{1}{2}\right) \tag{2.20}$$

where

$$a_f = \frac{1}{\sqrt{2\hbar\omega_f}}\left(\dot{Q}_f - i\omega_f Q_f\right) \quad (2.21)$$

is the annihilation operator for mode *f*.

The corresponding eigen energies are given by

$$E_{\{n_f\}} = \sum_f \hbar\omega_f\left(n_f + \frac{1}{2}\right) \quad (2.22)$$

where n_f = 0, 1, 2…, the number of quanta $\hbar\omega_f$ in mode *f*.

In both the classical and the quantum cases, the mode frequencies ω_f and the corresponding eigenvectors $\boldsymbol{\psi}(f)$ have to be obtained from the eigenvalue equation 2.13. which can be rewritten as

$$\sum_{\ell' k' \beta}\left[\phi_{\alpha\beta}(\ell k, \ell' k') - \omega_f^2 m_k \delta_{\ell\ell'}\delta_{kk'}\delta_{\alpha\beta}\right]\psi(\ell' k' \beta|f) = 0 \quad (2.23)$$

Applying Bloch's theorem to a periodic solid, the solution to equation 2.23 can be expressed as plane waves of the form

$$\psi_\alpha(\ell k|\boldsymbol{q}j) = \frac{e_\alpha(k|\boldsymbol{q}j)}{\sqrt{NM(k)}} exp[i\boldsymbol{q}.\boldsymbol{R}(\ell k)] \quad (2.24)$$

here $\mathbf{R}(\ell k)$ denotes the equilibrium position of the k_{th} atom in the ℓ_{th} primitive cell and

$$\{e_\alpha(k|\mathbf{q}j)\} \equiv \mathbf{e}(\mathbf{q}j) \quad (2.25)$$

are the phonon polarization vectors which satisfy the orthonormality and completeness relations given by

$$\boldsymbol{e}^+(\boldsymbol{q}j)\,\boldsymbol{e}(\boldsymbol{q}j') = \delta_{jj'} \quad (2.26)$$

where j = 1, 2, 3,….,3n label the polarization branches. Equation 2.23 reduces to

$$\sum_{\ell' k' \beta} \frac{\phi_{\alpha\beta}(\ell k, \ell' k')}{\sqrt{m_k m_{k'}}} exp[i\boldsymbol{q}.\boldsymbol{R}(\ell' k')] e_\beta(k'|\boldsymbol{q}j) = \omega_f^2 exp[i\boldsymbol{q}.\boldsymbol{R}(\ell k)] e_\alpha(k|\boldsymbol{q}j)$$

(2.27)

which can be written as

$$\sum_{kk'} \left[D_{\alpha\beta}(kk'|\boldsymbol{q}) - \omega^2(\boldsymbol{q})\delta_{kk'}\delta_{\alpha\beta}\right] e(kk'|\boldsymbol{q}j) = 0 \quad (2.28)$$

where

$$D_{\alpha\beta}(kk'|\boldsymbol{q}) = \frac{1}{\sqrt{m_k m_{k'}}} \sum_{\ell'} \phi_{\alpha\beta}(\ell k, \ell' k') exp\{i\boldsymbol{q}.[\boldsymbol{R}(\ell) - \boldsymbol{R}(\ell')]\} \quad (2.29)$$

The previous equation can be written in matrix form as

$$[\boldsymbol{D}(\boldsymbol{q}) - \omega^2(\boldsymbol{q})\boldsymbol{I}]\boldsymbol{e}(\boldsymbol{q}j) = 0 \quad (2.30)$$

where **D**($\boldsymbol{q}$) is called the dynamical matrix.

Hence, we see that the plane wave solution 2.24 decouples the eigenvalue problem in equation 2.13 into N sets of 3n x 3n problems, one for each wave vector $\boldsymbol{q}$ (equation 2.30). For a non-trivial solution,

$$|\boldsymbol{D}(\boldsymbol{q}) - \omega^2(\boldsymbol{q})\boldsymbol{I}| = 0 \quad (2.31)$$

The index *f*, which labels the 3nN independent solutions to equation 2.13, is split into N wave vectors $\boldsymbol{q}$ and a branch index *j* that runs from 1 through 3*n*. These 3*n* harmonic eigenvalues $\omega_j(\boldsymbol{q})$ represent the phonon dispersion curves which can be measured using inelastic neutron scattering (INS) and therefore represent the contact point between theory and experiment. For a three dimensional crystal the dispersion relation contains 3 acoustic branches and 3*n*-3 optic branches. Fig. 2.1 shows the phonon dispersion curve for Ge.

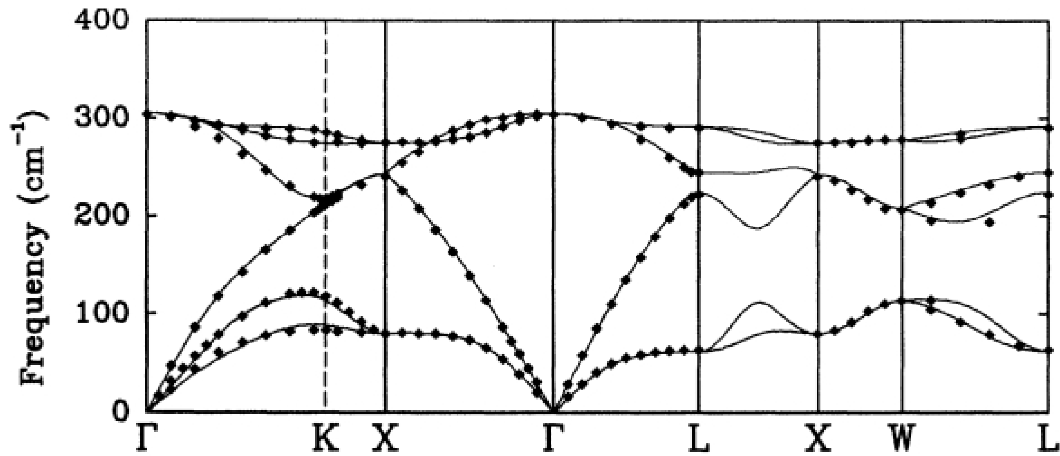

Figure 2.1 Ge phonon dispersion relation [22]. Copyright (1991) by the American Physical Society.

Since Raman spectroscopy is kinematically restricted to $\mathbf{q} \approx 0$ phonons, its role as a probe of the lattice dynamics of semiconductors is limited. However, since second order Raman scattering involves pairs of phonons with wave vectors $\mathbf{q}_1$ and $\mathbf{q}_2$ such that $\mathbf{q}_1 + \mathbf{q}_2 \approx 0$, it can be used to explore phonon frequencies away from $\mathbf{q} = 0$. In tetrahedral semiconductors the polarized second order Raman spectrum is essentially proportional to the phonon density of states[23].

2.3 Anharmonic Effects on Raman-Active Phonons

Till now we have discussed vibrations within the harmonic approximation, which neglects third- and higher-order terms of the crystalline potential. Within the harmonic approximation, the phonon modes are treated as independent oscillators, and once excited persist indefinitely and hence have an infinite lifetime. While this is a very good approximation, it is unable to account for many effects, such as thermal conductivity, thermal expansion, temperature- and pressure- dependent force and elastic constants, useful for characterization

purposes. An understanding of the interactions (anharmonicity) between the normal modes of these atomic vibrations is required for a detailed description of these physical properties.

In the presence of the higher-order terms (anharmonic perturbations), the phonon lifetime becomes finite, which manifests itself as the width of a phonon peak measured using spectroscopic techniques like Raman scattering. The lifetime of long-wavelength longitudinal optical (LO) phonons in polar semiconductors, is particularly important for applications. These lifetimes are typically of the order of few picoseconds. These phonons couple strongly to electrons and the resulting scattering rates depend directly on the phonon population, which is largest for the longest anharmonic lifetimes[24]. With density functional theory it has been possible to calculate anharmonic effects, such as widths, shapes, and shifts of Raman modes[25] and two-phonon absorption spectra in silicon and germanium[26].

Higher-order anharmonic effects can be treated by combining DFPT and frozen-phonon methods, and developing both methods may prove important to widening the scope of multiphonon interactions and their effects which can be realistically studied from theory.

2.4 Raman Scattering by Phonons

Consider the case of elastically reflected light. Let the field of the incident light be given by

$$\mathbf{E}\,(t) = \mathbf{E}_L \cos\omega_L(t) \tag{2.32}$$

Then the polarization induced in the material can be written as[27]

$$P_i(t) = \sum_j \chi_{ij}(\mathbf{u})\, E_{Lj} \cos\omega_L(t)$$

$$= \mathrm{Re} \sum_j \chi_{ij}(\mathbf{u})\, E_{Lj} \exp(-i\omega_L t)$$

$$= \frac{1}{2} \sum_j [\, \chi_{ij}(\mathbf{u}) \exp(-i\omega_L t) + \chi^*_{ij}(\mathbf{u}) \exp(i\omega_L t)\,]\, E_{Lj}$$

(2.33)

where χ_{ij} is the system's electronic susceptibility tensor. χ is a function of ω_L. The scattering cross section of the electromagnetic radiation produced by this time-dependent polarization is given by the radiated power per unit solid angle $d\Omega$ divided by the incident intensity. Thus, we get[27]

$$\frac{d\sigma}{d\Omega} = \frac{\omega_L^4 V^2}{c^4} |\sum_{ij} e_{Si}\ \chi_{ij} e_{Lj}|^2 \qquad (2.34)$$

where V is the volume of the scattering medium and $\mathbf{e}_S$ and $\mathbf{e}_L$are the unit polarization vectors for the scattered and incident radiation respectively. So the scattering cross section is proportional to the square of the magnitude of the fluctuations in χ:

$$\frac{d\sigma}{d\Omega} \propto\ \chi^*_{ij}(\boldsymbol{u})\chi_{i'j'}(\boldsymbol{u}) \qquad (2.35)$$

χ depends on the electronic structure of the system and changes as the atoms vibrate about their mean positions. Since in semiconductors, vibrational frequencies are much lower than the frequencies related to electronic transitions, we can consider the electronic susceptibility for a frozen atomic configuration **u.** So we will average $\chi^*_{ij}(\boldsymbol{u})\chi_{i'j'}(\boldsymbol{u})$ over all possible configurations of the lattice:

$$\langle \chi^*_{ij}\ \chi_{i'j'} \rangle = \frac{1}{Z_{vib}} \sum_{\nu\nu'} e^{-\beta E_\nu} \langle \nu | \chi^*_{ij}(\boldsymbol{u}) | \nu' \rangle \langle \nu' | \chi_{i'j'}(\boldsymbol{u}) | \nu \rangle \qquad (2.36)$$

where ν is the vibrational state of the system and Z_{vib} is the partition function. We

have assumed that the phonon frequency $\omega_{\nu\nu'}$ is infinitely sharp. So the observed Raman line will be a δ-function, $\delta\,(\omega_f - \omega_{\nu\nu'})$ as a function of the Raman shift ω_f . Now we can define the Raman differential cross section as

$$\frac{d^2\sigma}{d\Omega d\omega} = \frac{\omega_L^4 V^2}{c^4} |\sum_{ij} e_{Si}\ \chi_{ij} e_{Lj}|^2\, \delta\,(\omega_f\ \text{-}\ \omega_{\nu\nu'}) \tag{2.37}$$

Using the relation

$$\delta(\omega - \omega_{\nu\nu'}) = \frac{1}{2\pi}\int_{-\infty}^{\infty} dt\ e^{-i(\omega-\omega_{\nu\nu'})t} \tag{2.38}$$

we can write

$$\langle \chi_{ij}^*\ \chi_{i'j'} \rangle\ \delta(\omega - \omega_{\nu\nu'}) =$$

$$\frac{1}{2\pi}\int_{-\infty}^{\infty} dt\ e^{-i\omega t} \frac{1}{Z_{vib}} \sum_{\nu\nu'} e^{-\beta E_\nu} \left\langle \nu \middle| \chi_{ij}^*(\boldsymbol{u}) e^{i\omega_{\nu\nu'}t} \middle| \nu' \right\rangle \left\langle \nu' \middle| \chi_{i'j'}(\boldsymbol{u}) \middle| \nu \right\rangle \tag{2.39}$$

Now

$$\left\langle \nu \middle| \chi_{ij}^*(\boldsymbol{u}) e^{i\omega_{\nu\nu'}t} \middle| \nu' \right\rangle = \left\langle \nu \middle| e^{i\omega_\nu t} \chi_{ij}^*(\boldsymbol{u}) e^{-i\omega_{\nu'}t} \middle| \nu' \right\rangle \tag{2.40}$$

Using the Heisenberg representation

$$\chi_{ij}^*(\boldsymbol{u}, t) = e^{\frac{iHt}{\hbar}} \chi_{ij}^*(\boldsymbol{u}) e^{-iHt/\hbar} \tag{2.41}$$

we can write

$$\langle \chi_{ij}^*\ \chi_{i'j'} \rangle\ \delta(\omega - \omega_{\nu\nu'}) = \frac{1}{2\pi}\int_{-\infty}^{\infty} dt\ e^{-i\omega t} \langle \chi_{ij}^*(\boldsymbol{u}, t)\ \chi_{i'j'}(\boldsymbol{u}) \rangle \tag{2.42}$$

For small displacements from equilibrium, the susceptibility can be expanded as

$$\chi_{ij}(\boldsymbol{u}) = \chi_{ij}(\boldsymbol{0}) + \sum_{nk\delta} \frac{\partial \chi_{ij}}{\partial u_\delta(nk)} u_\delta(nk) + \cdots \tag{2.43}$$

Writing the displacements of the atoms in terms of the normal coordinates

$$\boldsymbol{u} = \sum_f \psi(f) Q_f \tag{2.44}$$

we get

$$\chi_{ij}(\boldsymbol{u}) = \chi_{ij}(\mathbf{0}) + \sum_f \frac{\partial \chi_{ij}(\boldsymbol{u})}{\partial Q_f}\bigg|_0 Q_f$$

$$= \chi_{ij}(\mathbf{0}) + \sum_f \chi_{ij,f} Q_f \quad (2.45)$$

where $$\sum_f \chi_{ij,f} Q_f = \sum_f \frac{\partial \chi_{ij}(\boldsymbol{u})}{\partial Q_f}\bigg|_0 Q_f \quad (2.46)$$

Using equation (2.45) we can write

$$\chi_{ij}^*(\boldsymbol{u},t)\chi_{i'j'}(\boldsymbol{u})$$

$$= \chi_{ij}^*(\mathbf{0})\chi_{i'j'}(\mathbf{0}) + \sum_{f'} \chi_{ij}^*(\mathbf{0})\chi_{i'j',f'} Q_{f'}$$

$$+ \sum_f \chi_{i'j'}\, \chi_{ij,f}^*\, Q_f(t) + \sum_{ff'} \chi_{ij,f}^* Q_f(t)\, \chi_{i'j',f'}\, Q_{f'}$$

(2.47)

So when we substitute equation (2.45) in equation (2.42), we find that the first term does not contain Q_f, which gives Rayleigh scattering. For finding the thermal average for the remaining linear and quadratic terms in Q_f, we use standard results from the quantum theory of the harmonic oscillator. Using the ladder operators defined by

$$a_f|n\rangle = \sqrt{n}|n-1\rangle \quad (2.48)$$

$$a_f^+|n\rangle = \sqrt{n+1}|n+1\rangle \quad (2.49)$$

the normal coordinates can be written as

$$Q_f(t) = i\sqrt{\frac{\hbar}{2\omega_f}}(a_f e^{-i\omega t} - a_f^+ e^{i\omega t} \quad (2.50)$$

$$Q_f = i\sqrt{\frac{\hbar}{2\omega_f}}(a_f - a_f^+) \quad (2.51)$$

The thermal averages $\langle Q_{f'} \rangle = 0$ and $\langle Q_f(t) \rangle = 0$, and the thermal average for $Q_f(t)Q_{f'}$ works out to be

$$\langle Q_f(t)Q_{f'} \rangle = \frac{\hbar}{2\omega_f}\delta_{ff'}\left[\langle n_f + 1\rangle e^{-i\omega_f t} + \langle n_f\rangle e^{i\omega_f t}\right] \qquad (2.52)$$

Keeping only the term contributing to Raman scattering, we get the Raman differential cross-section as[27]

$$\frac{d^2\sigma}{d\Omega d\omega} = \frac{\hbar V^2}{2c^4}\sum_f \frac{(\omega_L - \omega_f)^4}{\omega_f}\left\{(n_f + 1)\,\delta(\omega - \omega_f) + n_f(\omega + \omega_f)\right\} \times \left|\sum_{ij} e_{Si}\chi_{ij,f}e_{Lj}\right|^2 \qquad (2.53)$$

where

$$\langle n_f \rangle = \left(e^{\frac{\hbar\omega_f}{k_B T}} - 1\right)^{-1} \qquad (2.54)$$

is the Bose-Einstein phonon occupation number for mode f and ω_f is the Raman shift. The term containing $\delta(\omega - \omega_f)$ corresponds to Stokes scattering (creation of phonon) while the term containing $\delta(\omega + \omega_f)$ corresponds to anti-Stokes scattering (annihilation of phonon).

Equation (2.53) can be used to determine the selection rules for Raman scattering. If we replace the volume susceptibility $\chi_{ij,f}$ with the volume independent Raman tensor $R_{ij,f}$, equation (2.53) can be rewritten as[27]

$$\frac{d^2\sigma}{d\Omega d\omega} = \frac{\hbar V^2}{2\mu v_c c^4}\sum_f \frac{(\omega_L - \omega_f)^4}{\omega_f}\left\{(n_f + 1)\,\delta(\omega - \omega_f) + n_f(\omega + \omega_f)\right\} \times \left|\sum_{ij} e_{Si}R_{ij,f}e_{Lj}\right|^2 \qquad (2.55)$$

where

$$\chi_{ij,f} = \frac{1}{v_c}\sqrt{\frac{1}{\mu N}}R_{ij,f} \tag{2.56}$$

and v_c and μ are the volume and the mass of the unit cell respectively.

For diamond and zinc blende-type crystals the Raman tensors for phonons polarized along the *x*-, *y*- and *z*-axis, at $\mathbf{q} = 0$, are given by[27]

$$R_{ij,x} \equiv R(x) = \begin{pmatrix} 0 & 0 & 0 \\ 0 & 0 & a \\ 0 & a & 0 \end{pmatrix}$$

$$R_{ij,y} \equiv R(y) = \begin{pmatrix} 0 & 0 & a \\ 0 & 0 & 0 \\ a & 0 & 0 \end{pmatrix}$$

$$R_{ij,z} \equiv R(z) = \begin{pmatrix} 0 & a & 0 \\ a & 0 & 0 \\ 0 & 0 & 0 \end{pmatrix}$$

(2.57)

2.5 Effect of Perturbations on Vibrations

Many interesting phenomena, such as the addition of foreign atoms, the application of stress, etc., can be described as perturbations to the vibrational properties of semiconductors, which can be studied using Raman spectroscopy. The remainder of the chapter describes how Raman spectroscopy can be used to study these perturbations.

These perturbations will change the force constants and the mass matrices, so that equation (2.13) becomes

$$\left[(\boldsymbol{\Phi} + \Delta\boldsymbol{\Phi}) - \omega_f^2(\boldsymbol{M} + \Delta\boldsymbol{M})\right]\boldsymbol{\Psi}(f) = 0 \tag{2.58}$$

here, ω_f and $\boldsymbol{\Psi}\,(f)$ are the perturbed eigenfrequencies and eigenvectors.

In practical cases the perturbations are very small. So equation (2.58) (or 2.13) can be rewritten in terms of the complete set of orthonormal unperturbed mode eigenvectors $\{\Psi_0(f)\}$ and eigenfrequencies ω_{0f}. Since the unperturbed eigenvectors are a complete set, the perturbed eigenvectors can be written as a linear combination:

$$\boldsymbol{\Psi}_\alpha(\ell k|f) = \sum_{f'}^{3nN} c_{ff'} \Psi_{0\alpha}(\ell k|f') \tag{2.59}$$

here the sum is over the unperturbed modes. The coefficients $c_{ff'}$ are the expansion coefficients of the perturbed eigenvectors in terms of the unperturbed ones. Substituting equation (2.59) in equation (2.58) we get

$$\sum_{f'}\left[\left(\omega_{of}^2 - \omega_f^2\right)\delta_{ff'} + \Delta\boldsymbol{\Phi}_{ff'} - \omega_f^2 \Delta\boldsymbol{M}_{ff'}\right]c_{ff'} = 0 \tag{2.60}$$

where

$$\Delta\boldsymbol{M}_{ff'} = \boldsymbol{\Psi}_0^+(f)\Delta\boldsymbol{M}\boldsymbol{\Psi}_{\mathbf{0}}(f') \tag{2.61}$$

and

$$\Delta\boldsymbol{\Phi}_{ff'} = \boldsymbol{\Psi}_0^+(f)\Delta\boldsymbol{\Phi}\boldsymbol{\Psi}_{\mathbf{0}}(f') \tag{2.62}$$

are the perturbed matrix elements expressed in the basis of unperturbed eigenvectors.

Equations 2.59 and 2.60 can be used as the starting point for a perturbation theory treatment. These equations can be used to treat isotopic disorder (for which $\boldsymbol{\Delta\Phi} = 0$), stress ($\Delta\mathbf{M} = 0$), and alloying, for which both the force constant and mass matrices change.

2.6 Effect of Strain on Raman phonons

Strain in a crystal changes the equilibrium position of the crystal atoms. The force constants in a strained crystal are different from those in equation (2.8) due to the anharmonic terms in the crystal potential. The force constants of the deformed crystal are now evaluated at the new equilibrium position and are given by

$$\boldsymbol{\Phi}^{\varepsilon}_{\alpha\beta}(\ell k, \ell' k') = \boldsymbol{\Phi}_{\alpha\beta}(\ell k, \ell' k') + \sum_{\zeta\eta} \frac{\partial \boldsymbol{\Phi}_{\alpha\beta}(\ell k, \ell' k')}{\partial \varepsilon_{\zeta\eta}} \varepsilon_{\zeta\eta} \tag{2.63}$$

where $\varepsilon_{\zeta\eta}$ are the components of the strain tensor (as defined by Kittel[28]).

The equation of motion (2.11) now becomes

$$m_k \ddot{u}_\alpha(\ell, k) = -\sum_{\ell' k' \beta} \boldsymbol{\Phi}_{\alpha\beta}(\ell k, \ell' k') u_\beta(\ell', k') - \sum_{\ell' k' \beta \zeta\eta} \frac{\partial \boldsymbol{\phi}_{\alpha\beta}(\ell k, \ell' k')}{\partial \varepsilon_{\zeta\eta}} \varepsilon_{\zeta\eta} u_\beta(\ell k, \ell' k') \tag{2.64}$$

If we assume a plane wave solution of the same form as equation 2.12, we obtain the same equation as (2.31). Except now ω^2 is the difference between the squares of the perturbed ω_ε and the unperturbed ω_0 frequencies. Considering that there are two atoms in a primitive cell of diamond-type or zincblende-type structures, and the fact that $\Delta\mathbf{M} = 0$, for the triply degenerate $\mathbf{q} = 0$ Raman-active mode in diamond structure systems equation 2.60 becomes[29]

$$\begin{pmatrix} p\varepsilon_{xx} + q(\varepsilon_{yy} + \varepsilon_{zz}) - \Delta\omega_i^2 & 2r\varepsilon_{xy} & 2r\varepsilon_{xz} \\ 2r\varepsilon_{xy} & p\varepsilon_{yy} + q(\varepsilon_{zz} + \varepsilon_{xx}) - \Delta\omega_i^2 & 2r\varepsilon_{yz} \\ 2r\varepsilon_{xz} & 2r\varepsilon_{yz} & p\varepsilon_{zz} + q(\varepsilon_{xx} + \varepsilon_{yy}) - \Delta\omega_i^2 \end{pmatrix} \begin{pmatrix} u_1 \\ u_2 \\ u_3 \end{pmatrix} = 0 \qquad (2.65)$$

where *p*, *q* and *r* are the symmetry allowed anharmonic parameters called the phonon deformation potentials. So in the presence of strain, the **q** = 0 optical phonon splits into three modes whose frequencies are shifted by an amount ($\Delta\omega_i$) from the unstrained phonon frequencies (ω_0). The strain shifts of the Raman-active modes are determined by the phonon deformation potentials, *p*, *q* and *r*. In principal, this can be done by setting the determinant of the coefficients of the above equation equal to zero. The applied strain components are known. The eigen vector components $\{u_1, u_2, u_3\}$ when substituted in equation (2.59) give the phonon eigenvector corresponding to the perturbed mode. The underlying analysis of the effect of strain on Raman phonons is described in detail in chapter 3.

2.7 Effect of alloying on Raman phonons

The bulk properties of the alloy $A_{1-x}B_x$, formed by mixing the atoms of two similar semiconductors (A and B), are found to be composition dependent. For such an alloy, Raman peaks correspond to three types of optical phonons; namely, A-A, A-B and B-B, which depend on the composition of the alloy. The compositional dependence of the Raman shift can be expressed as the sum of a 'mass perturbation' and a 'bond perturbation term'[27]:

$$\Delta\omega^2(x) = \Delta\omega^2_{mass}(x) + \Delta\omega^2_{bonds}(x) \quad (2.66)$$

where $\Delta\omega_{mass}$ and $\Delta\omega_{bond}$ are the Raman shifts due to mass disorder and bond distortion respectively. The mass disorder term can be written as[30]

$$\Delta\omega_{mass} = -As\omega_0 \quad (2.67)$$

here A is a proportionality constant, s is the concentration of the individual element. The mass disorder is due to the confinement caused by the different masses. The atom with the heavier mass will not be able to follow the vibrations of the lighter atom, and hence will be more or less stationary. This results in the localization of the vibrations of the lighter atom, which leads to a reduction in its vibration frequency. This is the case, for example of Si atoms in Ge. But also optic-like Ge vibrations in Si become localized due to the very different eigen vector displacement patterns.

The bond distortion term is due to the lattice mismatch of the alloying components A and B. The change in length of the relevant bond can be given by[27]:

$$\frac{\Delta R}{R} = (1 - a^{**})\frac{\Delta a}{a} \quad (2.68)$$

where a^{**} is called the topological rigidity parameter [31, 32] which is a measure of the bond's tendency to conserve its length as a function of composition. Tensile strain (lengthening of bond) generally lowers the vibration frequency whereas compressive strain (shortening of bond) tends to increase the mode frequency. The bond distortion term is written as[27]

$$\Delta\omega_{bonds} = -3\gamma\frac{\Delta R}{R}\omega_0 \quad (2.69)$$

where γ is the Grüneisen parameter and ω_0 is the unperturbed frequency. The combination of the mass disorder term and the bond distortion term[33] explain qualitatively the compositional dependence of Raman modes in alloys.

CHAPTER 3

PHONON STRAIN-SHIFT COEFFICIENTS IN Si AND Ge

3.1 Introduction

Strain-engineering is nowadays essential for nanoscale CMOS devices because it enhances carrier mobility and is compatible with large scale integration[34]. The chemical sensitivity and spatial resolution of Raman spectroscopy, combined with the sensitivity of modern systems that can easily detect single atomic layers, have made this technique a preferred choice for the strain characterization of complex systems such as nanoscale CMOS devices[35]. A disadvantage of Raman spectroscopy, however, is that the shifts associated with strain are not related to the geometrical deformations in any obvious way, so that careful calibrations are needed to determine the anharmonic coefficients that relate strain to Raman shifts.

The first-order strain dependence of long-wavelength optical phonons in diamond-cubic semiconductors is characterized by a fourth-order tensor K_{ijkl} with the same form as the elastic constant tensor C_{ijkl}[36]. Accordingly, the strain shifts of the Raman-active modes in diamond, Si, Ge, and α-Sn are determined by three-parameters, p, q, and r, which represent the phonon-anharmonic analog of the C_{11}, C_{12}, and C_{44} elastic constants. The determination of p, q, and r, whose precise meaning is discussed below, is of considerable theoretical and practical interest. On the theoretical side, the calculation of anharmonic lattice-dynamical properties provides an ultimate test of the predictive capabilities of density functional theory.

A significant body of theory has emerged focused on the *ab initio* prediction of Raman phonon anharmonic self-energies, with special emphasis on explaining the lineshape of Raman peaks and their temperature and pressure dependence. [37, 38] However, calculations of *p*, *q*, and *r* are rare, and the few results available are inconsistent. On the practical side, knowledge of these parameters is critical if Raman spectroscopy is to be used to monitor strain in semiconductor nanostructures.

Table 3.1 shows the best sets of recommended values in the literature for Si and Ge. Information about *p*, *q*, and *r* can be obtained from three types of measurements: hydrostatic pressure Raman experiments using diamond anvil cells, uniaxial stress Raman experiments on large, bulk specimens, and Raman experiments on strained thin films grown by strained-layer epitaxy. [13, 14, 29, 39, 40] However, the recommended values of *p, q,* and *r* in the literature, such as those in Table 3.1, are deduced only from uniaxial stress experiments, and they are unsatisfactory in several respects. From a theoretical perspective, we would expect *p*, *q*, and *r* to be very similar in Si and Ge when expressed in dimensionless form, since the interatomic potential in these materials are very similar and their phonon dispersion curves essentially scale with the inverse square root of the average mass. However, the quoted values for the dimensionless form of *p, q,* and *r* for Si and Ge are significantly different, and their error ranges do not overlap. From an experimental perspective, the phonon deformation potentials in Table 3.1 are not entirely consistent with direct measurements in strained films. Moreover,

the quoted errors in these direct measurements are much less than the error computed from Table 3.1, suggesting that one could use the film experiments to reduce the errors in p, q, and r estimated from the stress experiments alone. So far, no attempt has been made to combine the results of the different experiments to reduce errors and enforce consistency across the different experimental approaches. In addition, the possibility of a deviation from linearity, that is, the possibility that p, q, and r may be strain dependent, has not been discussed in the literature.

The purpose of this chapter is twofold. First, we critically re-examine all available literature for Si and Ge and we show that by combining the results from different experiments it is possible to extract a consistent set of values for the parameters p and q for both Si and Ge which are very similar when expressed in a dimensionless way—exactly as might be expected from the similarity of the interatomic potential in both materials—and consistent with all available experimental data. Critical for this analysis is to take into account the non-linear pressure-volume relationship in these semiconductors, as well as issues in the calibration of uniaxial stress rigs. In the second part of this chapter we present a new set of measurements of the Raman shift in strained Ge films grown on relaxed SiGe buffer layers deposited on Si substrates. The results are discussed in terms of the new, consistent set of p and q parameters and suggest that the combination p-q may be strain dependent. This additional complication has never before been addressed and suggests further studies will be necessary.

Table 3.1Currently recommended values for deformation potentials *p*, *q* and *r*

	Si[b]	Ge[c]
p	-1.85 ± 0.06	-1.47 ± 0.20
q	-2.31 ± 0.06	-1.93 ± 0.19
r	-0.71 ± 0.02	-1.11 ± 0.19

[b]E. Anastassakis, A. Cantarero, and M. Cardona, Phys. Rev. B **41** (11), 7529 (1990).

[c]F. Cerdeira, C. J. Buchenauer, F. H. Pollak, and M. Cardona, Phys. Rev. B **5**, 580 (1972).

3.2 Definition of Basic Parameters

To understand the possible differences between "pressure experiments", in which hydrostatic pressure is applied in a diamond anvil cell, "stress experiments", in which a large bulk specimen is subject to uniaxial stress, and "strain experiments", in which a thin film is grown fully strained on a lattice-mismatched substrate, it is critical to examine the approximations leading to the expressions commonly used to fit the experimental data. We have seen in chapter 2 that the secular equation for diamond and zinc blende semiconductors is given by (equation 2.65)

$$\begin{pmatrix} p\varepsilon_{xx} + q(\varepsilon_{yy} + \varepsilon_{zz}) - \Delta\omega_i^2 & 2r\varepsilon_{xy} & 2r\varepsilon_{xz} \\ 2r\varepsilon_{xy} & p\varepsilon_{yy} + q(\varepsilon_{zz} + \varepsilon_{xx}) - \Delta\omega_i^2 & 2r\varepsilon_{yz} \\ 2r\varepsilon_{xz} & 2r\varepsilon_{yz} & p\varepsilon_{zz} + q(\varepsilon_{xx} + \varepsilon_{yy}) - \Delta\omega_i^2 \end{pmatrix} \begin{pmatrix} u_1 \\ u_2 \\ u_3 \end{pmatrix} = 0 \quad (3.1)$$

where p, q and r are the strain deformation potentials[13] and $\Delta\omega_i^2 = \omega_\varepsilon^2 - \omega_0^2$ is the difference between the squares of the perturbed (strained) and unperturbed frequencies and x, y and z correspond to the Cartesian coordinates in the crystalline cubic cell. So the strain dependent frequency is given by

$$\begin{aligned}\Delta\omega_i^2 &= \omega_\varepsilon^2 - \omega_0^2 \\ &= (\omega_\varepsilon - \omega_0)(\omega_\varepsilon + \omega_0) \\ &\cong (\omega_\varepsilon - \omega_0)2\omega_0\end{aligned} \tag{3.2}$$

or

$$\omega_\varepsilon \approx \omega_0 + \frac{\Delta\omega_i^2}{2\omega_0} \tag{3.3}$$

For non-trivial solutions

$$\begin{vmatrix} p\varepsilon_{xx} + q\left(\varepsilon_{yy} + \varepsilon_{zz}\right) - \Delta\omega_i^2 & 2r\varepsilon_{xy} & 2r\varepsilon_{xz} \\ 2r\varepsilon_{xy} & p\varepsilon_{yy} + q\left(\varepsilon_{zz} + \varepsilon_{xx}\right) - \Delta\omega_i^2 & 2r\varepsilon_{yz} \\ 2r\varepsilon_{xz} & 2r\varepsilon_{yz} & p\varepsilon_{zz} + q\left(\varepsilon_{xx} + \varepsilon_{yy}\right) - \Delta\omega_i^2 \end{vmatrix} = 0 \tag{3.4}$$

Expanding the determinant we get

$$\begin{aligned}&\left[p\varepsilon_{xx} + q\left(\varepsilon_{yy} + \varepsilon_{zz}\right) - \Delta\omega_i^2\right]\left\{\begin{matrix}\left[p\varepsilon_{yy} + q\left(\varepsilon_{zz} + \varepsilon_{xx}\right) - \Delta\omega_i^2\right]\left[p\varepsilon_{zz} + q\left(\varepsilon_{xx} + \varepsilon_{yy}\right) - \Delta\omega_i^2\right] \\ -4r^2\varepsilon_{yz}^2\end{matrix}\right\} \\ &-2r\varepsilon_{xy}\left\{2r\varepsilon_{xy}\left[p\varepsilon_{zz} + q\left(\varepsilon_{xx} + \varepsilon_{yy}\right) - \Delta\omega_i^2\right] - 4r^2\varepsilon_{xz}\varepsilon_{yz}\right\} \\ &\quad +2r\varepsilon_{xz}\left\{4r^2\varepsilon_{xy}\varepsilon_{yz} - 2r\varepsilon_{xz}\left[p\varepsilon_{yy} + q\left(\varepsilon_{zz} + \varepsilon_{xx}\right) - \Delta\omega_i^2\right]\right\} = 0\end{aligned} \tag{3.5}$$

Now, a general strain tensor[41] can be written as

$$\boldsymbol{\varepsilon} = \begin{pmatrix} \varepsilon_{xx} & \varepsilon_{xy} & \varepsilon_{xz} \\ \varepsilon_{yx} & \varepsilon_{yy} & \varepsilon_{yz} \\ \varepsilon_{zx} & \varepsilon_{zy} & \varepsilon_{zz} \end{pmatrix} \tag{3.6}$$

Due to symmetry $(\varepsilon_{ij} = \varepsilon_{ji})$, only six independent components are required to fully describe strain. When applied to a crystal structure, the trace of the strain tensor corresponds to the hydrostatic strain (or changes in bond length only), while the off- diagonal terms correspond to anisotropic or shear components (which involves changes in bond angles).

For uniaxial stress, the off-diagonal elements of the stress tensor are zero[42]. For cubic systems the strain has in-plane $(\varepsilon_{\parallel})$ and out-of-plane $(\varepsilon_{\perp})$ components. For stress along [001] the strain tensor simplifies to

$$\boldsymbol{\varepsilon} = \begin{pmatrix} \varepsilon_{\parallel} & 0 & 0 \\ 0 & \varepsilon_{\parallel} & 0 \\ 0 & 0 & \varepsilon_{\perp} \end{pmatrix} \tag{3.7}$$

Using the elements defined in equations (3.7) , equation (3.5) can be rewritten for the case when $\varepsilon_{xx} = \varepsilon_{yy} = \varepsilon_{\parallel}$ and $\varepsilon_{zz} = \varepsilon_{\perp}$.

$$\left[p\varepsilon_{\parallel} + q\left(\varepsilon_{\parallel} + \varepsilon_{\perp}\right) - \Delta\omega_i^2\right]\left\{\left[p\varepsilon_{\parallel} + q\left(\varepsilon_{\perp} + \varepsilon_{\parallel}\right) - \Delta\omega_i^2\right]\left[p\varepsilon_{\perp} + q\left(\varepsilon_{\parallel} + \varepsilon_{\parallel}\right) - \Delta\omega_i^2\right]\right\} = 0 \tag{3.8}$$

or

$$\left[p\varepsilon_{\parallel} + q\left(\varepsilon_{\parallel} + \varepsilon_{\perp}\right) - \Delta\omega_i^2\right]^2\left[p\varepsilon_{\perp} + 2q\varepsilon_{\parallel} - \Delta\omega_i^2\right] = 0 \tag{3.9}$$

So equation (3.9) gives rise to a singlet and a doublet whose expressions are given by

$$\Delta\omega_{si}^2 = p\varepsilon_{\perp} + 2q\varepsilon_{\parallel} \tag{3.10}$$

and

$$\Delta\omega_{di}^2 = p\varepsilon_{\parallel} + q\left(\varepsilon_{\parallel} + \varepsilon_{\perp}\right) \tag{3.11}$$

Using equation (3.3) we get

$$\omega_{s\varepsilon} = \omega_0 + \frac{p\varepsilon_{\perp} + 2q\varepsilon_{\parallel}}{2\omega_0} \tag{3.12}$$

and

$$\omega_{d\varepsilon} = \omega_0 + \frac{p\varepsilon_{\parallel} + q\left(\varepsilon_{\parallel} + \varepsilon_{\perp}\right)}{2\omega_0} \tag{3.13}$$

For the diamond structure, in the absence of strain, the q ≈ 0 optical phonons are triply degenerate. Epitaxial strain along the [001] direction splits these degenerate modes into13 a singlet ($\omega_{s\varepsilon}$) with an eigenvector parallel to the strain and a doublet ($\omega_{d\varepsilon}$) with eigenvectors perpendicular to the strain. The phonon dispersion curve for Ge is shown in figure 2.1 in chapter 2. For backscattering along the [001] direction, the singlet gives rise to the longitudinal optic (LO) and the doublet gives rise to the two transverse optic (TO) phonons. Virtually all measurements of thin films in the literature, including ours, are based on the backscattering geometry, so that only the singlet mode is detected. Thus the strain correction to the observed Raman mode in our case will be

$$\Delta\omega = \frac{p\varepsilon_{\perp} + 2q\varepsilon_{\parallel}}{2w_0} \tag{3.14}$$

By contrast, in stress experiments on macroscopic specimens one can use other scattering geometries which make it possible to observe both the singlet and the doublet.

It is customary to express the shift of the measured Raman mode in terms of a Gruneisen parameter (γ) and a shear deformation potential (a_s). The

Gruneisen parameter, which can be obtained from the hydrostatic pressure shifts of the Raman modes, is defined as[13]

$$\gamma = -\frac{d \ln \omega}{d \ln V} \tag{3.15}$$

where ω is the frequency and V is the volume.

If we assume hydrostatic strain that changes the equilibrium cubic lattice constant a_0 to a,

$$\varepsilon_{xx} = \varepsilon_{yy} = \varepsilon_{zz} = \varepsilon = \frac{a - a_0}{a_0}$$

and

$$\varepsilon_{xy} = \varepsilon_{xz} = \varepsilon_{yz} = 0 \tag{3.16}$$

we obtain from equation (3.10)

$$\frac{\Delta\omega_i^2}{\omega_0^2} = \frac{p + 2q}{\omega_0^2}\varepsilon \tag{3.17}$$

or, if we approximate $\Delta\omega_i/\omega_0 = \frac{1}{2}\Delta\omega_i^2/\omega_0^2$,

$$\frac{\Delta\omega_i}{\omega_0} = \frac{p + 2q}{2\omega_0^2}\varepsilon = -\gamma\frac{\Delta V}{V_0} . \tag{3.18}$$

Here we have expressed the Gruneisen parameter γ in terms of the *p* and *q* coefficients. Now since

$$\frac{\Delta V}{V_0} = (1+\varepsilon)^3 - 1 = 3\varepsilon + 3\varepsilon^2 + \varepsilon^3 \tag{3.19}$$

we get, neglecting higher order terms

$$\frac{\Delta V}{V_0} = 3\varepsilon \tag{3.20}$$

From equations (3.18) and (3.20) we find

$$\gamma = -\frac{1}{6\omega_0^2}\left(p+2q\right) \tag{3.21}$$

Let us now assume that the cubic cell of lattice constant a_0 is distorted into a tetragonal cell of constants a and c. So the strains are now

$$\varepsilon_{xx} = \varepsilon_{yy} = \frac{a-a_0}{a_0}$$

$$\varepsilon_{zz} = \frac{c-a_0}{a_0}$$

and

$$\varepsilon_{xy} = \varepsilon_{xz} = \varepsilon_{yz} = 0 \tag{3.22}$$

Equations (3.10) and (3.11) can be rewritten as

$$\frac{\Delta\omega_{s\varepsilon}^2}{\omega_0^2} = \frac{p\varepsilon_{zz} + 2q\varepsilon_{xx}}{\omega_0^{\;2}} \tag{3.23}$$

and

$$\frac{\Delta\omega_{d\varepsilon}^2}{\omega_0^2} = \frac{p\varepsilon_{xx} + q\left(\varepsilon_{xx}+\varepsilon_{zz}\right)}{\omega_0^{\;2}} \tag{3.24}$$

This can be expressed in a more symmetrical way as

$$\frac{\Delta\omega_{s\varepsilon}^2}{\omega_0^2} = \frac{p+2q}{3\omega_0^{\;2}}\left(2\varepsilon_{xx}+\varepsilon_{zz}\right) - 2\left(\frac{p-q}{3\omega_0^{\;2}}\right)\left(\varepsilon_{xx}-\varepsilon_{zz}\right) \tag{3.25}$$

and

$$\frac{\Delta\omega_{d\varepsilon}^2}{\omega_0^2} = \frac{p+2q}{3\omega_0^{\;2}}\left(2\varepsilon_{xx}+\varepsilon_{zz}\right) + \frac{p-q}{3\omega_0^{\;2}}\left(\varepsilon_{xx}-\varepsilon_{zz}\right) \tag{3.26}$$

or

$$\frac{\Delta\omega_{s\varepsilon}^2}{\omega_0^2} = -2\gamma\left(2\varepsilon_{xx}+\varepsilon_{zz}\right) - \frac{4}{3}a_s\left(\varepsilon_{xx}-\varepsilon_{zz}\right) \tag{3.27}$$

$$\frac{\Delta\omega_{d\varepsilon}^{2}}{\omega_0^2} = -2\gamma\left(2\varepsilon_{xx} + \varepsilon_{zz}\right) + \frac{2}{3}a_s\left(\varepsilon_{xx} - \varepsilon_{zz}\right) \tag{3.28}$$

where we have defined the shear phonon deformation potential as

$$a_s = \frac{1}{2\omega_0^2}\left(p - q\right) \tag{3.29}$$

which determines mode splittings under uniaxial stress along the (001) direction. Another way to calculate the coefficients is by generating biaxial strain by heteroepitaxial growth of lattice mismatched materials. For growing epitaxially on the substrate, the layer's lattice parameter in the plane parallel to the surface of the substrate ($a_{\parallel}$) should be equal to that of the substrate. This in turn will induce a distortion in the layer's lattice parameter in the plane perpendicular to the surface of the substrate ($a_{\perp}$), producing a tetragonally strained layer. In this approach the strain has to be measured independently (by HRXRD in this work).

3.3 Pressure and Stress Experiments

One way to determine the coefficients γ and a_s is to subject the samples to hydrostatic and uniaxial stress. Anastassakis[43] was the first to measure these parameters simultaneously from stress experiments. An external stress applied along the [001] direction produces a frequency shift between the singlet and doublet modes. From these shifts γ and a_s, (or p, and q) and r can be calculated. The Grüneisen parameter γ can be obtained by subjecting the sample to hydrostatic pressure, typically via diamond anvil cells. From the strain-stress relations, we have, at an external pressure P:

$$\begin{bmatrix} -P \\ -P \\ -P \end{bmatrix} = \begin{pmatrix} C_{11} & C_{12} & C_{12} \\ C_{12} & C_{11} & C_{12} \\ C_{12} & C_{12} & C_{11} \end{pmatrix} \begin{bmatrix} \varepsilon \\ \varepsilon \\ \varepsilon \end{bmatrix} \tag{3.30}$$

or

$$P = -\left(C_{11} + 2C_{12}\right)\varepsilon = -\frac{C_{11} + 2C_{12}}{3}\frac{\Delta V}{V_0} = B_0 \frac{\Delta V}{V_0} \tag{3.31}$$

Here we have introduced the bulk modulus $B_0 = (C_{11} + 2C_{12})/3$ and used equation (3.20). From equations (3.18) and (3.31) we obtain

$$\frac{\Delta\omega_i}{\omega_0} = -\gamma\frac{\Delta V}{V_0} = -\gamma\frac{p}{B_0} \tag{3.32}$$

If uniaxial stress is applied in the *zz* direction:

$$\begin{bmatrix} 0 \\ 0 \\ -\sigma \end{bmatrix} = \begin{pmatrix} C_{11} & C_{12} & C_{12} \\ C_{12} & C_{11} & C_{12} \\ C_{12} & C_{12} & C_{11} \end{pmatrix} \begin{bmatrix} \varepsilon_{xx} \\ \varepsilon_{xx} \\ \varepsilon_{zz} \end{bmatrix} \tag{3.33}$$

This gives the following two equations:

$$(C_{11} + C_{12})\varepsilon_{xx} + C_{12}\varepsilon_{zz} = 0$$

$$2C_{12}\varepsilon_{xx} + C_{11}\varepsilon_{zz} = -\sigma$$

Solving this system we find

$$2\varepsilon_{xx} + \varepsilon_{zz} = -\frac{\sigma}{C_{11} + 2C_{12}}$$

and

$$\varepsilon_{xx} - \varepsilon_{zz} = -\frac{\sigma}{C_{11} - C_{12}} \tag{3.34}$$

Inserting these into equations (3.27) and (3.28) we obtain

$$\frac{\omega_h^2 - \omega_0^2}{\omega_0^2} = -2\gamma\left(2\varepsilon_{xx} + \varepsilon_{zz}\right) = \frac{2\gamma}{C_{11} + 2C_{12}}\sigma = \frac{2\gamma}{3B_0}\sigma \tag{3.35}$$

$$\frac{\omega_{s\varepsilon}^2 - \omega_{d\varepsilon}^2}{\omega_0^2} = -2a_s\left(\varepsilon_{xx} - \varepsilon_{zz}\right) = -\frac{2a_s}{C_{11} - C_{12}}\sigma \tag{3.36}$$

where we have defined

$$\omega_h^2 = \frac{\omega_s^2 + 2\omega_d^2}{3} + \omega_0^2 \tag{3.37}$$

A problem with this approach is that the relationship between strain and stress, assumed linear in Eqs. (3.30) and (3.34), deviates from this behavior experimentally. In the case of the pressure-volume relationship, the deviation can be expressed in terms of the so-called Murnaghan equation of state as[44]

$$\frac{\Delta V}{V_0} = \left[1 + \frac{B_0^{'}}{B_0}p\right]^{-1/B_0^{'}} - 1 \tag{3.38}$$

where $B_0' = dB_0/dp|_{p=0}$.

3.4 Strain Experiments

In recent years, the availability of strained-layer films has provided an alternative calibration method that has made it possible to bypass stress calibration issues by directly measuring the dependence of Raman frequencies on strain. This strain—typically a tetragonal distortion of the cubic symmetry—is simple enough to be characterized via x-ray studies. The Raman spectrum of the films, even very thin ones, can be easily measured with modern equipment. The

deformation potential can be obtained from the observed strain-induced Raman shift.

If a sample of cubic lattice constant a_0 is grown along the (001) direction on a substrate with lattice constant a, then the following equations define the components of the strain produced in the planes parallel and perpendicular to the substrate:

$$\varepsilon_{\parallel} = \frac{a_{\parallel} - a_0}{a_0} \tag{3.39}$$

$$\varepsilon_{\perp} = \frac{a_{\perp} - a_0}{a_0} \tag{3.40}$$

Because the sample is stress free in the *zz* direction, we have

$$\begin{bmatrix} -\sigma \\ -\sigma \\ 0 \end{bmatrix} = \begin{pmatrix} C_{11} & C_{12} & C_{12} \\ C_{12} & C_{11} & C_{12} \\ C_{12} & C_{12} & C_{11} \end{pmatrix} \begin{bmatrix} \varepsilon_{\parallel} \\ \varepsilon_{\parallel} \\ \varepsilon_{\perp} \end{bmatrix} \tag{3.41}$$

So the parallel and perpendicular components of the strain are related to each other as

$$\varepsilon_{\perp} = -2\frac{C_{12}}{C_{11}}\varepsilon_{\parallel} \tag{3.42}$$

This can also be derived from an energy minimization argument. We write the total energy as

$$\Phi_{\varepsilon} = \frac{1}{2}\sum_{IJ} C_{IJ}\varepsilon_I\varepsilon_J + \frac{1}{6}\sum_{IJK} C_{IJK}\varepsilon_I\varepsilon_J\varepsilon_K + \frac{1}{24}\sum_{IJKL} C_{IJKL}\varepsilon_I\varepsilon_J\varepsilon_K\varepsilon_L \tag{3.43}$$

Here we use the Voigt notation

$$\begin{aligned} &\varepsilon_1 = \varepsilon_{xx}; \quad \varepsilon_2 = \varepsilon_{yy}; \quad \varepsilon_3 = \varepsilon_{zz} \\ &\varepsilon_4 = 2\varepsilon_{yz} = 2\varepsilon_{zy} \\ &\varepsilon_5 = 2\varepsilon_{zx} = 2\varepsilon_{xz} \\ &\varepsilon_6 = 2\varepsilon_{xy} = 2\varepsilon_{yx} \end{aligned} \tag{3.44}$$

Keeping terms up to quadratic

$$\Phi_\varepsilon = \frac{1}{2}C_{11}\left(\varepsilon_1^2+\varepsilon_2^2+\varepsilon_3^2\right)+C_{12}\left(\varepsilon_1\varepsilon_2+\varepsilon_1\varepsilon_3+\varepsilon_2\varepsilon_3\right)+\frac{1}{2}C_{44}\left(\varepsilon_4^2+\varepsilon_5^2+\varepsilon_6^2\right) \tag{3.45}$$

which in our case becomes

$$\Phi_\varepsilon = \frac{1}{2}C_{11}\left(2\varepsilon_{xx}^2+\varepsilon_{zz}^2\right)+C_{12}\left(\varepsilon_{xx}^2+2\varepsilon_{xx}\varepsilon_{zz}\right) \tag{3.46}$$

Minimizing this energy with respect to ε_{zz}, we get equation 3.42. Equation 3.43 is useful to study higher-order corrections to equation.3.42. For Si and Ge, the third and fourth order elastic constants are known, but when we insert this in equation 3.43, the condition 3.42 is affected only by 1%.

TABLE 3.2 Elastic constants for Si and Ge from McSkimmin's data at 25°C[47]

(GPa)	Si	Ge
C_{11}	165.773	128.528
C_{12}	63.924	48.26
B_0	97.874	75.016

As mentioned before for cubic crystals, the epitaxially induced strain can be separated into a hydrostatic (also known as isotropic) and an anisotropic component. The hydrostatic strain given by

$$\varepsilon_i = 2\varepsilon_{\parallel} + \varepsilon_{\perp} \tag{3.47}$$

changes only the volume of the crystal and not the crystal symmetry, while the anisotropic strain, given by

$$\varepsilon_a = \varepsilon_{\parallel} - \varepsilon_{\perp} \tag{3.48}$$

reduces the symmetry of the crystal without changing its volume. Using equations (3.42) and (3.14) we can write

$$\Delta\omega = \omega_0 \left(\frac{q}{\omega_0^2} - \frac{C_{12} p}{C_{11}\omega_0^2} \right) \varepsilon_{\parallel} \tag{3.49}$$

The proportionality constant between the strain correction to the observed Raman mode and the strain is called the phonon strain shift coefficient. The relationship is expressed as

$$\Delta\omega = b\varepsilon_{\parallel} \tag{3.50}$$

where

$$b = \omega_0 \left(\frac{q}{\omega_0^2} - \frac{C_{12} p}{C_{11}\omega_0^2} \right) \tag{3.51}$$

is the strain shift coefficient. Rearranging terms in equations (3.21) and (3.29), and substituting in equation (3.51) we find,

$$b = \omega_0 \left[-\frac{2}{3}\left(a_s + 3\gamma\right) + \frac{2C_{12}}{3C_{11}}\left(3\gamma - 2a_s\right) \right] \tag{3.52}$$

or

$$b = 2\omega_0 \left[-\frac{a_s}{3}\left(\frac{2C_{12}}{C_{11}} + 1 \right) + \gamma \left(\frac{C_{12}}{C_{11}} - 1 \right) \right] \tag{3.53}$$

where ω_0 is the unstrained Raman frequency.We use this expression to determine the Ge-Ge vibration in Si-Ge alloys.

3.5 Application to Silicon

3.5.1 Grüneisen parameter

The pressure dependence of the Raman phonon of Si has been measured at room temperature by Weinstein[45]. His result is

$$\omega_{Si}(p) = \left(519.5 \pm 0.8\right) + \left(5.2 \pm 0.3\right) p - \left(0.07 \pm 0.02\right) p^2 \qquad (3.54)$$

where the pressure is in GPa. The curve is shown in Fig. 3.1 If we take the linear coefficient as representative of infinitesimal changes, we get

$$\gamma = -\frac{\Delta\omega}{p}\left(\frac{B_0}{\omega_0}\right) = \left(5.2 \pm 0.3\right) \times \left(\frac{97.874}{519.5}\right) = 0.98 \pm 0.05 \qquad (3.55)$$

The non-linearity of the curve can be easily displayed by attempting to fit a straight line to it. This is shown in Fig. 3.1, where the fit has been limited to the 0-2 GPa range to match the uniaxial stress data to be discussed below:

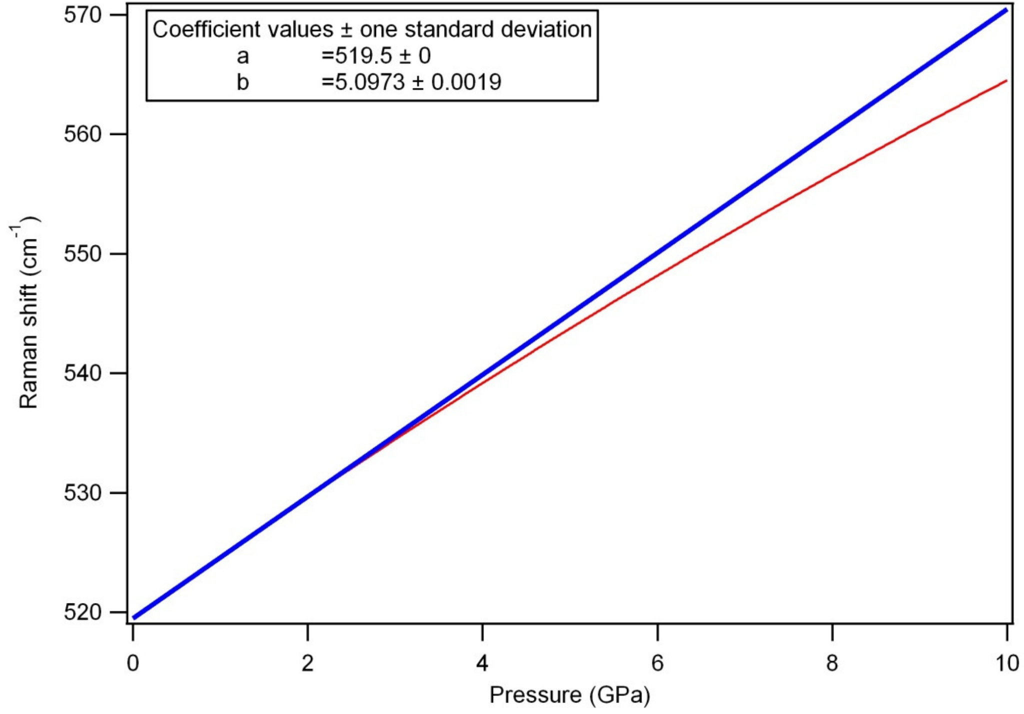

Figure 3.1 Fitting a straight line (thick line) to the pressure dependent Raman shift of Si measured at room temperature by Weinstein[45].

If we use the slope of this line as the definition of our Grüneisen parameter we obtain

$$\gamma = -\frac{\Delta\omega}{p}\left(\frac{B_0}{\omega_0}\right) = 5.0973 \times \left(\frac{97.874}{519.5}\right) = 0.96 \pm 0.05 \quad (3.56)$$

assuming the same error as in the previous determination. Measurements at 6K were carried out by Ulrich et al[46]. They find

$$\omega_{Si}(p) = 523.88(10) + 5.10(4)p - 0.062(4)p^2 \quad (3.57)$$

where the pressure is in GPa. We also digitized McSkimmin's data for C_{11} and C_{12} as a function of temperature[47]. From the digitized data we interpolate

B_0(25ºC) = 97.8187 GPa and B_0(6K) = 99.2805 GPa. Since the value at 25 ºC differs slightly from the value for B_0 at 25 ºC proposed by McSkimmin in a different paper and used in Table 3.2, we "renormalize" the 6K value as follows: So we will use B_0(6K) = 99.2805*97.874/97.8187= 99.341 GPa. Using this we obtain a Grüneisen parameter of

$$\gamma = -\frac{\Delta\omega}{p}\left(\frac{B_0}{\omega_0}\right) = 5.0973\times\left(\frac{99.341}{523.88}\right) = 0.967 \pm 0.007 \qquad (3.58)$$

So we see that the dependence on temperature of the Grüneisen parameter is non existent within experimental error.

Let us now study the effect of taking into account the non-linear pressure-volume relationship. Hu et al[48] studied the p-V relation experimentally and they find good agreement with Murnaghan's equation (3.38) using McSkimmin's values B_0 = 97.88 GPa and B_0' = 4.24.

$$\frac{\Delta V}{V_0} = \left(1 + \frac{B_0'}{B_0}p\right)^{-1/B_0'} - 1$$

Using this relation we find the curve below for room temperature data.

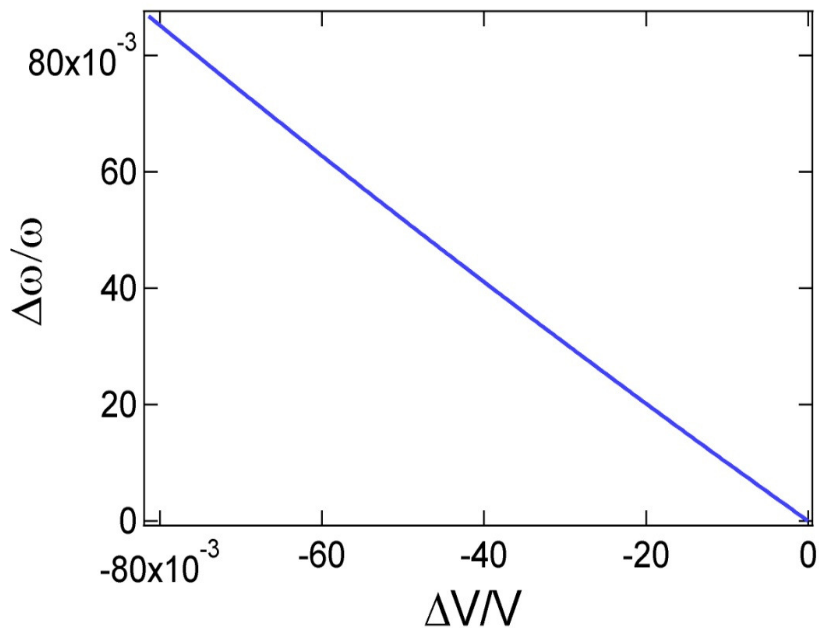

Figure 3.2 Dependence of frequency-shift on volume based on Hu et al's[5] study of the p-V relation experimentally and Weinstein's pressure measurements of the Raman shifts.

We can see that the dependence of the frequency shift on volume is now more linear than in the graph of the frequency shift versus pressure (figure 3.1). This means that the non-linearities in the pressure dependence of the frequencies are due in part to the non-linear pressure-volume relationship.

If we fit this with a quadratic polynomial over a volume range less than 0.04, the linear term is by definition the Grüneisen parameter, and we obtain $\gamma = 0.98 \pm 0.05$. This is exactly what we obtain from the quadratic fit to the pressure dependence, because for infinitesimal volume changes Murnaghan's equation is equivalent to the simple linear expression in Eq. 3.32. However, for finite volume changes the results are different. For example, if we fit a linear expression to the

pressure dependence up to 2 GPa, as discussed above, we obtain $\gamma = 0.96$, but if we fit the volume dependence with a linear expression up to the equivalent volume change of 2%, we obtain $\gamma = 1.00$, so that there is a systematic difference, on the order of 4% between experiments that assume linear dependence on pressure and experiments that assume linear dependence on volume.

3.5.2 Uniaxial stress experiments

Uniaxial stress data for Si are available from Anastassakis et al[13, 43] in two papers separated by twenty years. The 1990 paper shows results collected at 110K and with a stress up to 2 GPa. For the hydrostatic part they find $\Delta\omega_h/\sigma = 1.88 \pm 0.05$ cm^{-1}/GPa. Using equations (3.35) and (3.36) we obtain

$$\gamma = \left(\frac{\Delta\omega_h}{\sigma}\right)\frac{3B_0}{\omega_0} = \left(1.88 \pm 0.05\right) \times \frac{3\times 99.04}{523.6} = 1.07 \pm 0.03 \qquad (3.59)$$

However, the authors quote $\gamma = 1.08 \pm 0.07$. The slightly different value may be due to the values they use for B_0 and ω_0, which are not indicated. We have used the bulk modulus at 110K from our above-mentioned digitized McSkimmin data and the phonon frequency at 110K from Balkanski.[49]. The larger error bar quoted by Anastassakis is not explained in their paper and appears to contradict the error they quote for the "raw" measurements. At the same level of theory one obtains a Grüneisen parameter of $\gamma = 0.960$ from the hydrostatic pressure experiments discussed above, so that there is marginal agreement between the two experiments when using the error bars indicated by Anastassakis, and likely disagreement when using the error bars that we compute. Similarly, if we compare with the data

from Ulrich, there seems to be a meaningful discrepancy between the pressure and stress experiments.

For the singlet-doublet splitting under (001) stress, Anastassakis *et al* find $\omega_s - \omega_d$ = -1.16 ± 0.12 cm^{-1}/GPa, so that from (3.53), we obtain

$$a_s = \frac{\omega_d - \omega_s}{\sigma\omega_0}\left(C_{11} - C_{12}\right) = \frac{\left(1.16 \pm 0.12\right)}{523.6} \times 102.465 = 0.23 \pm 0.02 \qquad (3.60)$$

Here we have used the elastic constants at 110K. We can now compute the strain-shift parameter *b*, using equation (3.53)

$$b = -2\left[\frac{a_s}{3}\left(1 + \frac{C_{12}}{C_{11}}\right) + \gamma\left(1 - \frac{C_{12}}{C_{11}}\right)\right]\omega_0$$

$$= -2\left[1.0668 \times 0.612281 + 0.0757 \times 1.77544\right] \times 523.6 = -825 \pm 30 cm^{-1} \qquad (3.61)$$

Measurements at room temperature were carried out by Anastassakis himself in the 1970 paper, but he has only two data points there, and also by Chandrasekhar et al[39], using the 6471 Å excitation. However, she has fewer data points than Anastassakis in 1990. We have digitized her data and we find $\Delta\omega_h/\sigma$ = 1.64 ± 0.10 cm^{-1}/GPa. Using equations (3.35) we obtain in her case

$$\gamma = \left(\frac{\Delta\omega_h}{\sigma}\right)\frac{3B_0}{\omega_0} = \left(1.64 \pm 0.10\right) \times \frac{3 \times 97.874}{520.0} = 0.93 \pm 0.05 \qquad (3.62)$$

where we have used the Bulk modulus at room temperature and Chandrasekhar's own zero stress frequency.

Similarly, they find $\omega_s - \omega_d$ = -1.25 ± 0.16 cm^{-1}/GPa, so that from equation (3.37), we obtain

$$a_s = \frac{\omega_d - \omega_s}{\sigma\omega_0}\left(C_{11} - C_{12}\right) = \frac{\left(1.25 \pm 0.16\right)}{520.0} \times 101.849 = 0.245 \pm 0.030 \quad (3.63)$$

Here we have used the elastic constants at room temperature. We can now compute the strain-shift parameter b, using equation (3.53)

$$b = -2\left[\frac{a_s}{3}\left(1 + \frac{C_{12}}{C_{11}}\right) + \gamma\left(1 - \frac{C_{12}}{C_{11}}\right)\right]\omega_0$$

$$= -2\left[0.926 \times 0.614389 + \frac{0.2488}{3} \times 1.77122\right] \times 520.0 = -744 \pm 50 cm^{-1} \quad (3.64)$$

In summary, while the predicted strain dependence of the Si phonon frequency from the Anastassakis and Chandrasekhar experiments overlap within experimental error, there seems to be a real difference between their measured Grüneisen parameter.

3.5.3 Strain experiments

Most of the strain experiments consist of measurements of the shift in strained Si grown on relaxed SiGe. They are usually given in terms of the coefficient *b*. Table 3.3 shows this coefficient as measured by several authors.

Table 3.3 Strain-shift coefficient in Si from literature.

Author	b	Number of points	Error	γ	a_s	Max strain (%)
Nakashima(UV)[51]	-723	8	15	0.994	0.14±0.08	1.2
Canonico	-744		7	1.001	0.17±0.06	1.8
Omote[96]	-760	29	15	0.992	0.20±0.08	1.05
Wong[50]	-784	3	10	0.992	0.24±0.07	1.1
Tsang[97]	-815			0.986	0.297	0.5

(In the case of Omote and Wong we have re-evaluated their error bars)

The errors are much smaller than in the stress measurements, and the error ranges for the strain and stress measurements do not overlap, even though the stress measurements have larger errors. However, it appears that the results in Table 3.3 may be affected by systematic errors, since the results do not agree well within the quoted error ranges. To obtain the a_s value corresponding to each measurement, we extract the appropriate value of the Grüneisen parameter γ from the dependence of frequency versus volume in Fig. 3.2. For consistency, we fit the change in frequency with respect to $\Delta V/V_0$ over a similar volume range as experienced in the strain experiments. This means a volume expansion which, in the case of the Nakashima et al[51] experiment, is

$$\Delta V/V_0 \simeq 2\varepsilon_{xx} + \varepsilon_{zz} = 2\left(1 - C_{12}/C_{11}\right)\varepsilon_{xx}$$

$$= 2\times(1-0.3856)\times 0.012 = 0.014 \qquad (3.65)$$

Figure 3.3 shows a linear fit of the frequency versus volume relationship. The data has been fitted to a volume change of 0.014.

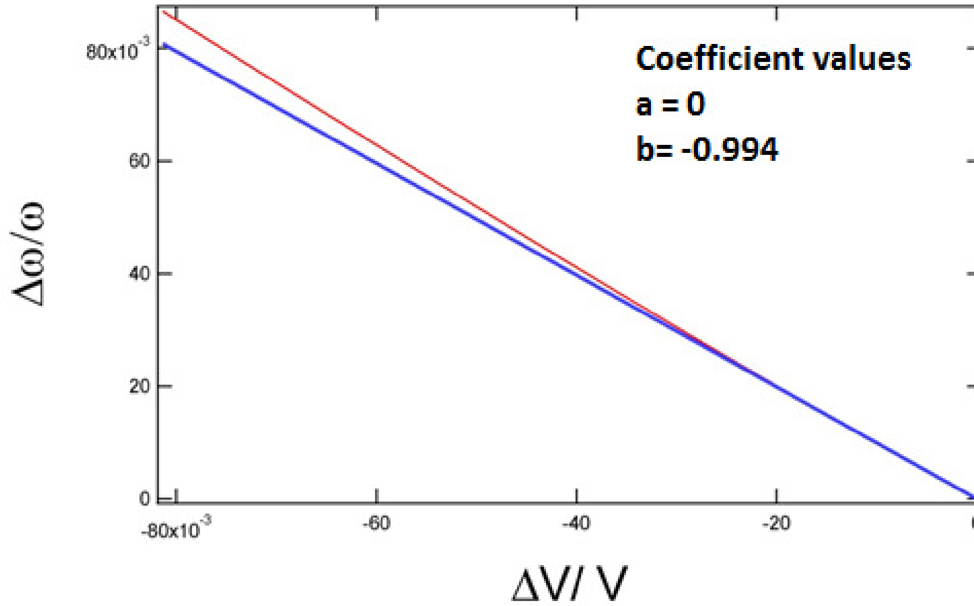

Figure 3.3 Plot of $d\omega/\omega$ versus $\Delta V/V_0$ for strained Si grown on SiGe. The measurements were made by Nakashima et al[53]. The data has been fitted with a linear fit (thick blue line).

So that in this case the "effective" Grüneisen parameter applicable to the strain experiments is $\gamma = 0.994$. Then from equation 3.53 we obtain

$$a_s = -\frac{3}{2}\frac{\frac{b}{\omega_0}+2\gamma\left(1-\frac{C_{12}}{C_{11}}\right)}{\left(1+\frac{2C_{12}}{C_{11}}\right)} \qquad (3.66)$$

$$= -\frac{3}{2}\frac{\frac{-723}{520.5}+2\times 0.994\times 0.614389}{1.77122} = 0.14 \pm 0.08$$

where we assume the same 5% error in the Grüneisen parameter. All calculated values of a_s from the strain experiments are shown in Table 3.3. The largest source of error is the uncertainty in the Grüneisen parameter. This reverses the situation relative to the stress measurements. Whereas the error in a_s in stress experiments is on the order of 10%, in the strain experiments the error is as large as 60% because the singlet-doublet splitting is not observed directly, and makes a relatively small contribution to the overall singlet shift.

A troubling aspect of the strain measurements summarized in Table 3.3, as indicated above, is the poor overlap of the different measurements given their small quoted errors. In some cases the number of experimental points is so small that the small error may be an artifact caused by the accidental alignment of the reduced number of experimental points. If we concentrate on the measurements with larger number of points, however, we still see discrepancies. Therefore, it is possible that systematic errors affect the different measurements. In this respect, it is important to point out that Omote *et al* used grazing-incidence X-ray diffraction, with which the in-plane lattice parameter of the top strained layer can be determined with a precision of 10^{-5}. This is more than one order of magnitude better than the precision of conventional X-ray diffraction measurements. For example Nakashima *et al* claim a precision of 4×10^{-4}. If their lattice constant measurements were off by this amount, their value of b could be as high as 750 cm^{-1}, and therefore agree, within error, with the results of Omote *et al*. In view of these considerations we believe that the result from Omote *et al* is the most

trustworthy value, and their error (which we computed by digitizing their data, since no errors were quoted in the original paper) the most realistic one, since it is not affected by systematic deviations in the strain estimate.

3.6 Application to Germanium

3.6.1 Grüneisen parameter

The pressure dependence of the Raman phonon of Ge has been measured at room temperature by Olego and Cardona[52]. They find

$$\omega_{Ge}(p) = \left(300.6 \pm 0.5\right) + \left(3.85 \pm 0.05\right) p - \left(0.039 \pm 0.006\right) p^2 \qquad (3.67)$$

where the pressure is in GPa. Measurements at 6K were carried out by Ulrich et al[46]. They find

$$\omega_{Ge}(p) = 304.64\left(13\right) + 4.02\left(7\right) p - 0.059\left(8\right) p^2 \qquad (3.68)$$

where the pressure is in GPa.

If we take the linear coefficient as representative of infinitesimal changes, we get for the room temperature data:

$$\gamma = -\frac{\Delta\omega}{p}\left(\frac{B_0}{\omega_0}\right) = \left(3.85 \pm 0.05\right) \times \left(\frac{75.016}{300.6}\right) = 0.96 \pm 0.01 \qquad (3.69)$$

We could also try to fit a straight line to the data over the range of the measurements, to obtain an "effective" Grüneisen parameter over 0-2 GPa range to match the uniaxial stress data to be discussed below:

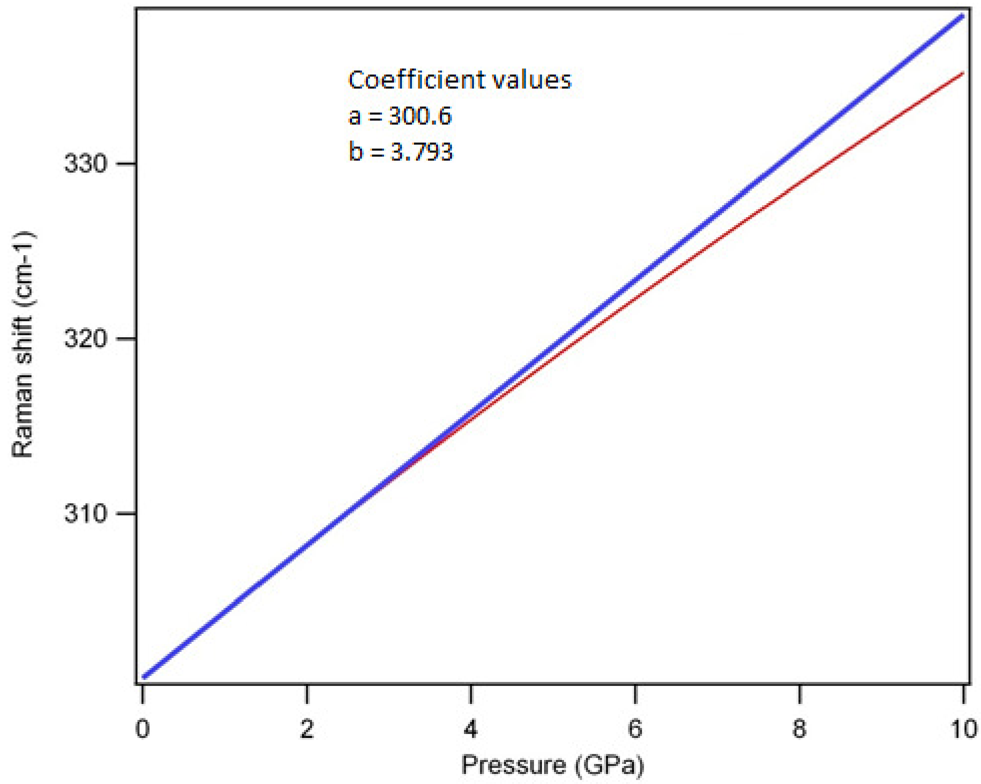

Figure 3.4 Linear fit (thick line) to the Ge mode measured by Olego [57] at room temperature.

This means that the effective Grüneisen parameter is

$$\gamma = -\frac{\Delta\omega}{p}\left(\frac{B_0}{\omega_0}\right) = 3.793 \times \left(\frac{75.016}{300.6}\right) = 0.94(6) \qquad (3.70)$$

Let us now study the effect of taking into account the non-linear pressure-volume relationship. Menoni et al[53] studied the *p*-*V* relation experimentally and they find good agreement with Murnaghan's equation using $B_0 = 74.9$ GPa and $B_0' = 3.0$. So instead of plotting the shift versus the pressure, we plot the shift

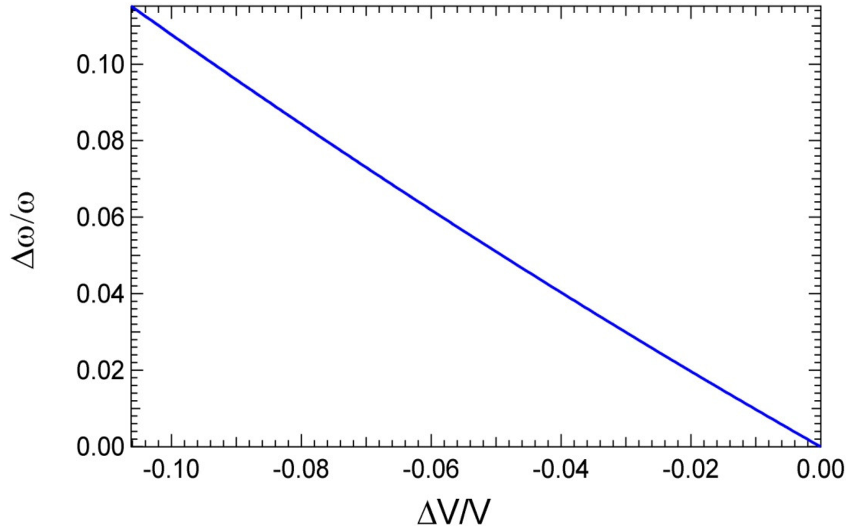

Figure 3.5 Plot of $d\omega/\omega$ versus $\Delta V/V_0$ for strained Ge grown on SiGe. The measurements were made by Menoni et al[54]. The data has been fitted with a linear fit.

relative to the change in volume in figure 3.5. This gives a linear relationship. If we fit a quadratic polynomial, the linear term is by definition the Gruneisen parameter, and we obtain $\gamma = 0.96 \pm 0.01$.

3.6.2 Uniaxial stress experiments

Cerdeira et al[8] have determined the deformation potential tensor components of Ge via uniaxial stress experiments. The values of the phonon parameters are quoted as $\gamma = 0.89 \pm 0.09$, $a_s = 0.23 \pm 0.02$ and $r = -1.11$. The error in their Grüneisen parameter brings it marginally within the range of the hydrostatic pressure experiments. To better understand this difference we have digitized Cerdeira's raw data and recomputed the parameters. For the (001) stress, their Grüneisen parameter turns out to be $\gamma = 0.82$, which appears too small. From the same data their shear coefficient turns out to be $a_s = 0.24 \pm 0.01$. If we look at

their (111) data, we find that the corresponding Gruneisen parameter is γ = 0.981 and we deduce r = 0.94. The a_s value agrees with the value quoted by Cerdeira. The Gruneisen parameter quoted by Cerdeira appears to be an average for the two directions. Using the values recommended by Cerdeira, we obtain from 3.53

$$b = -2\left[-\frac{a_s}{3}\left(\frac{2C_{12}}{C_{11}}+1\right)+\gamma\left(\frac{C_{12}}{C_{11}}-1\right)\right]\omega_0$$

$$= -2\times\left[0.89\times 0.6245+\frac{0.23}{3}\times 1.7509\right]\times 300 = -414.0\pm 40cm^{-1} \qquad (3.71)$$

3.6.3 Previous strain experiments

The only published experiment we are aware of is the work of Pezzoli et al[15]. They find b = - 440 ± 8 cm^{-1}. They have three data points with up to 0.5% strain. This means a maximum volume expansion of

$$\Delta V/V_0 \simeq 2\varepsilon_{xx}+\varepsilon_{zz} = 2\left(1-C_{12}/C_{11}\right)\varepsilon_{xx} \qquad (3.72)$$

$$= 2\times(1-0.375)\times 0.005 = 0.006 \qquad (3.73)$$

This is so small that the effective Grüneisen parameter for this case, γ = 0.965, is very close to the “exact” Grüneisen parameter γ = 0.961. Using equation (3.53), we get a_s = 0.23 ± 0.02.

3.7 Theory

Ab initio calculations were carried out by de Gironcoli[54]. According to his calculation the Si phonon frequency is 517 cm^{-1} at normal volume. It shifts under a change (increase) in relative volume of 0.06 by -30 cm^{-1} and for a volume of 0.12 by -59 cm^{-1}. This implies γ = 0.97 for the “small” expansion and and γ = 0.93

for the large expansion. In the case of Ge, the relaxed phonon is at 303 cm^{-1}. For a volume compression of -0.06 the shift is +18 cm^{-1}, and for a compression of -0.11 the shift is +39 cm^{-1}. This implies γ = 1.07 and γ = 1.18, respectively. One can clearly see the difference between Si and Ge. This suggests that the Grüneisen parameter increases for compression and decreases for expansion. De Gironcoli also calculates the strain splittings, but he only gives numbers for the Si case. He claims that for Si grown on Ge, ω_s - ω_d = 3.7 cm^{-1}

$$\omega_d - \omega_s = a_s \left(1 + \frac{2C_{12}}{C_{11}}\right) \varepsilon_{xx} \tag{3.74}$$

Using his calculated elastic constants and strains, this gives a_s = 0.104, which is small but difficult to compare with experiment due to the huge expansion. This would imply a b parameter of (from equation 3.53)

$$\begin{aligned} b &= -2\left[\gamma\left(1 - \frac{C_{12}}{C_{11}}\right) + \frac{a_s}{3}\left(1 + \frac{2C_{12}}{C_{11}}\right)\right]\omega_0 \\ &= -2\left[0.97 \times 0.623 + 0.104 \times 1.755\right] \times 517 = -688 \text{ cm}^{-1} \end{aligned} \tag{3.75}$$

Earlier calculations by Nielsen[55] yield a_s = 0.131. However, Methfessel gets a_s = 0.23[56]. Interestingly, he also gets γ = 0.99, but r = 0.97, which is in much better agreement with the experimental Ge than with the experimental Si value. This suggests that the experimental r value for Ge might be more reliable than the value quoted for Si. Very recently Hossain [57] published some new calculations. They find b = -793 for Si and b = -352 cm^{-1} for Ge. This small value for Ge is

possible because they get $\gamma = 0.96$ for Si and $\gamma = 1.23$ for Ge.

3.8 Reconciliation of *p*, *q*, and *r*

The recommended values of p, q, and r lead to Gruneisen parameters that are beyond the error bars of the hydrostatic pressure experiments and phonon strain shift coefficients b that are beyond the acceptable range as determined from strain experiments. We also note that the accidental error in the coefficient a_s as measured in uniaxial stress experiments is much less than the error obtained from strain experiments. This is because the singlet-doublet splitting is measured directly in stress experiments, whereas only the singlet is observed in conventional strain experiments.

Let us assume that the uniaxial stress experiments of Anastassakis et al are affected by a systematic error in the stress calibration. This is plausible because stress rigs are difficult to calibrate, whereas hydrostatic pressure in diamond anvil cells is well characterized by the ruby emission, as evidenced by the fact that the Weinstein, Olego, and Ulrich experiments are in excellent agreement. We could then correct for this calibration error by multiplying all results by a factor $0.96/1.07 = 0.90$ which arises from dividing the Grüneisen parameter from the more accurate pressure experiments by the Grüneisen parameter from the stress experiments. This would lead to $a_s = 0.21 \pm 0.02$. On the other hand, to obtain a value of b that can be compared with the value from the strain experiments, we must use the value that obtains from a linear fit of the *volume* dependence, which,

as indicated above, is $\gamma = 1.00$. Thus we would predict $b = -769\pm40$ cm^{-1}, perfectly consistent with the strain experiments of Omote *et al*.

If we apply the same correction to Ge, the Grüneisen parameter obtained from the stress experiments for stress in the (001) direction is $\gamma = 0.82$. On the other hand, the value that should have been measured, from the hydrostatic pressure dependence of the Raman frequency, is $\gamma = 0.94$, so that the "renormalized" value of the shear deformation potential is $a_s = 0.27\pm0.01$. Using the Grüneisen parameter $\gamma = 0.96$ from the volume dependence of the Raman frequency, we predict $b = -455\pm10$ cm^{-1}, which is close to the value $b = -440\pm8$ cm^{-1}. We notice that in the case of Ge, Cerdeira et al find very different values for γ depending on whether the stress is in the (001) or (111) directions, so that the discrepancies with the pressure experiments cannot be only due to a stress calibration issue. We thus adjust the value of a_s to bring the value of b into agreement with the Pezzoli data. This gives $a_s = 0.23$. Therefore, the values in Table 3.4 are consistent with all relevant experiments:

Table 3.4 Recommended values of the Grüneisen parameter γ, shear phonon deformation potential (a_s), and deformation potentials p, q and r.

	Si	Ge
γ	1.00 ± 0.01	0.96 ± 0.01
a_s	0.21 ± 0.02	0.23 ± 0.02
p	-1.72 ± 0.05	-1.61 ± 0.03
q	-2.14 ± 0.03	-2.07 ± 0.03

On the other hand, for the r value Anastassakis gives $r = -0.71 \pm 0.02$. From his quoted pressure dependence of the splitting, we obtain $r = -0.70 \pm 0.02$. Moreover, from our own analysis of Chandrasekhar's 111 data we obtain $\gamma = 0.923 \pm 0.13$ and $r = -0.635 \pm 0.043$. If we renormalize using $\gamma = 0.96$, we obtain $r = -0.63 \pm 0.02$ from Anastassakis and $r = -0.66 \pm 0.043$ from Chandrasekhar. The difference with the value of r for Ge is still large and we strongly suspect it is unphysical, so that this parameter needs further research.

3.9 Our strain experiment

One troubling aspect of the existing experimental data regarding epitaxially strained Ge films is the low-level of strain in the films. In this section we extend the measurements to high levels of strain of technological and fundamental interest. High quality strained Ge on relaxed SiGe buffer layers grown in the Hoyt lab at MIT were used to measure the strain shift parameter b. The sample consists of (001) p-type Si substrates, followed by a graded SiGe buffer layer, followed by a constant concentration relaxed SiGe layer, and finally capped with a thin Ge layer. Figure 3.6 shows a schematic diagram of the sample.

Figure 3.6 Schematic diagram of the sample consisting of a strained Ge layer deposited on a relaxed SiGe layer.

When the SiGe layer is grown on the Si substrate, it will be strained due to lattice mismatch. Misfit dislocations are produced to relieve excess strain. It has been shown[58] that by first growing a compositionally graded buffer layer, the threading and misfit dislocations are confined to the graded buffer, producing a relaxed, dislocation-free SiGe layer.

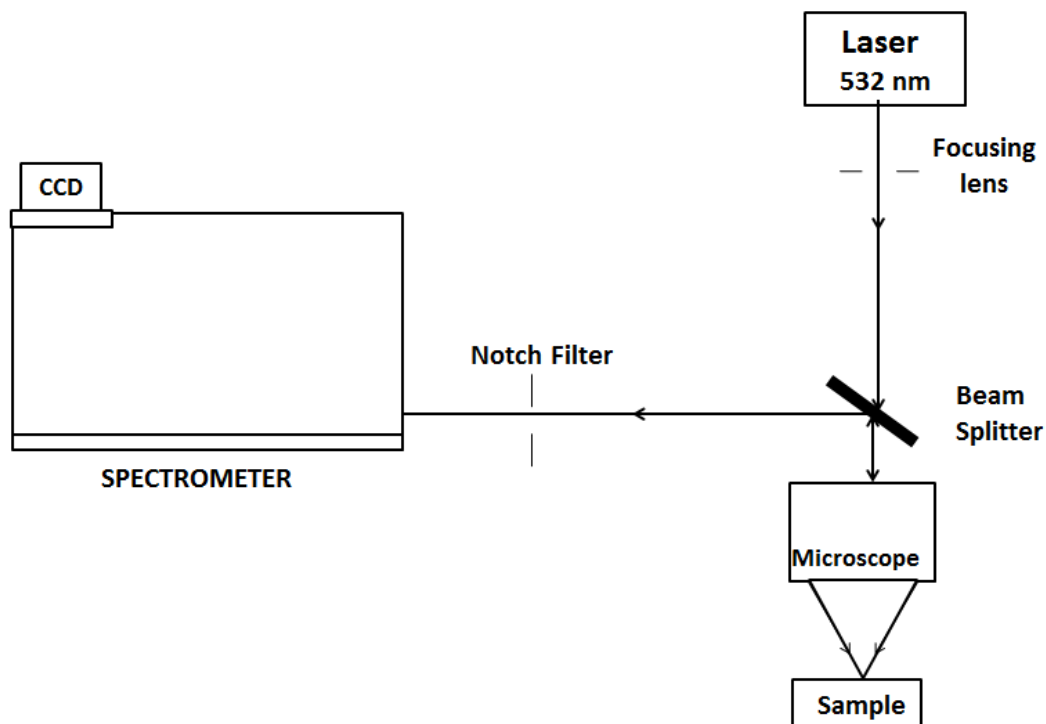

Figure 3.7 Schematic Raman experimental setup.

The Raman spectra were collected at room temperature in the backscattering configurations represented by the *Porto* convention, z (x, y) $\bar{z}$ and z (x, x) $\bar{z}$; where x, y and z correspond to the 100, 010 and 001 crystal directions respectively. In the *Porto* convention, the first and the last symbols represent the directions of the incident and the scattered beam; and the symbols inside the bracket represent the polarization directions of the incident and the scattered beams respectively. A schematic diagram of the experimental setup is shown in figure 3.7. A 532 nm laser line from a frequency doubled Nd:YAG laser with excitation power of 1mW was focused onto the sample with a microscope using a

100X objective lens. A single Acton monochromator and a liquid nitrogen-cooled charge coupled device detector were used to analyze the scattered light.

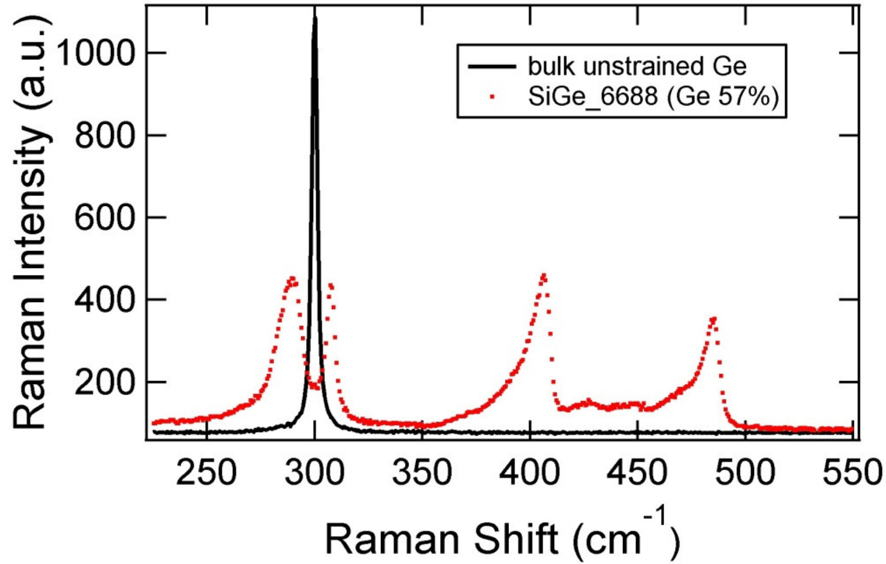

Figure 3.8 Raman spectra of bulk unstrained Ge and compressively strained Ge (dotted line) deposited on a relaxed SiGe (57% Ge) layer.

Figure 3.8 shows the Raman spectra from bulk unstrained Ge and sample #6688 (Ge 57%). The modes observed are the Ge-Ge mode in SiGe (~ 290 cm^{-1}), the Ge-Ge mode in Ge (307 cm^{-1}), the SiGe mode (375 cm^{-1}) and the Si - Si mode in SiGe (485 cm^{-1}). Since the optical penetration depth in Ge at 532 nm is much larger than the Ge cap thicknesses we can see the underlying SiGe modes in the spectra. Here, we will focus on the strain shift of the Ge-Ge mode frequency which has been fitted using a Voigt profile.

Table 3.5 Ge compositions and layer thicknesses of the samples.

Sample	Concentration x (%)	graded t_{SiGe} (μm)	const t_{SiGe} (μm)	$t_{Ge\ cap}$ (Å)
6684	40.0	4.0	0.75	71.0
6685	48.4	5.0	1.0	78.0
6688	57.0	6.0	1.0	91.0
MIT42C	48.0	5.5	1.5	70.0

The Ge compositions and layer thicknesses are shown in Table 3.5. The fully relaxed SiGe layer has a Ge content ranging from 40% to 57%. With higher Ge composition in the buffer layer, the lattice mismatch between the SiGe alloy and the Ge-cap decreases, thereby reducing the tensile strain in the Ge cap. Hence, as the strain in the Ge cap decreases, the Ge-Ge mode frequency approaches that of the unstrained bulk Ge.

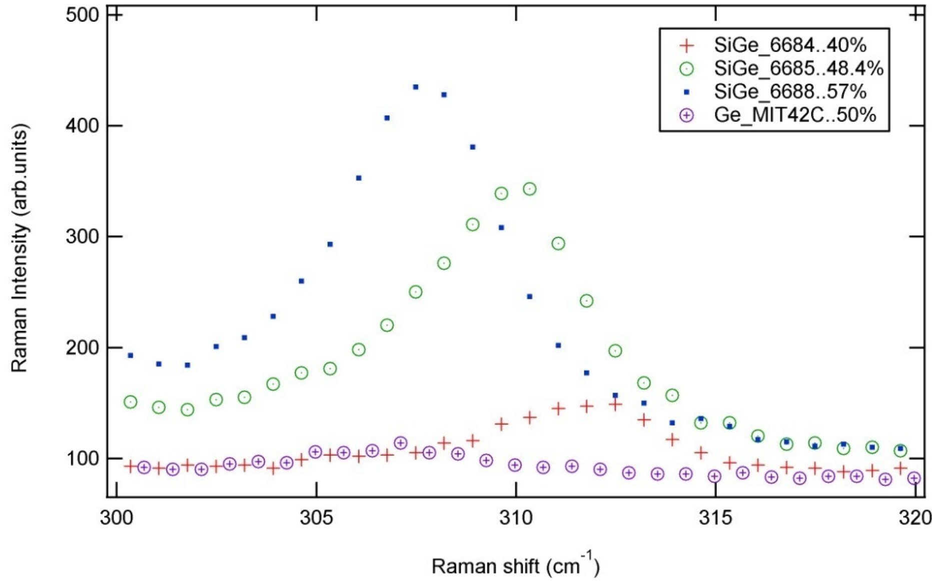

Figure 3.9 Raman spectra of the Ge LO phonon from the various strained Ge caps deposited on relaxed SiGe buffer layers.

Since the thin Ge layer is hardly detectable in our X-ray experiments, we tentatively assumed that the in plane lattice parameter in the Ge layer matches the relaxed lattice parameter of the underlying SiGe layer. This leads to $b = -425 \pm 8$ cm^{-1}, in good agreement with the results from Pezzoli et al. However, as discussed above for the case of Si, a precision of 10^{-5} in the lattice constant measurement is required to avoid introducing large errors in *b.* Therefore, we obtained grazing incidence X-ray data for our samples by collaborating with Dr. K. Omote at the X-ray Research Laboratory, Rigaku Corporation, Japan.

When the X-ray beam is incident onto the sample surface at a grazing angle (α) equal to its critical angle for total internal reflection (α_c), X-rays are

totally reflected. Under this condition, X- rays can penetrate only a few nanometers of the surface and basically propagate parallel to the surface. When, as in the geometry shown in Figure 3.10, the specimen is oriented to satisfy the angle for Bragg diffraction in the plane of the sample, a strong diffracted beam can be observed. In such an arrangement, Bragg planes normal to the sample surface are probed. The in-plane lattice parameter (in-plane strain) can be measured by performing a ϕ–$2\theta_\chi$ scan of the sample and the detector.

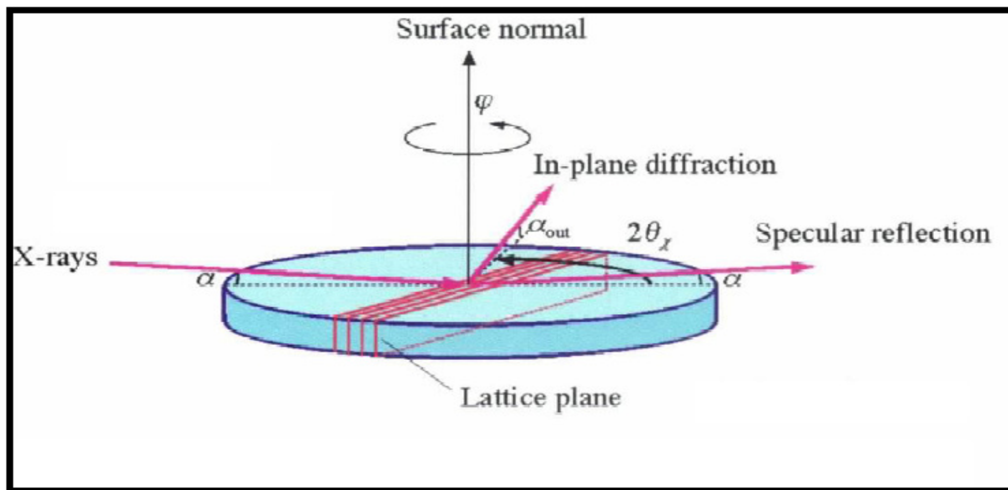

Figure 3.10 Schematic diagram of X-ray optics for in-plane diffraction.

The Rigaku ATX-G diffractometer system has been used to measure the in-plane lattice parameter of our strained Ge layers with an incident angle of 0.2^o. The Raman peak shifts are plotted in figure 3.11 versus the strains measured using this grazing incidence geometry.

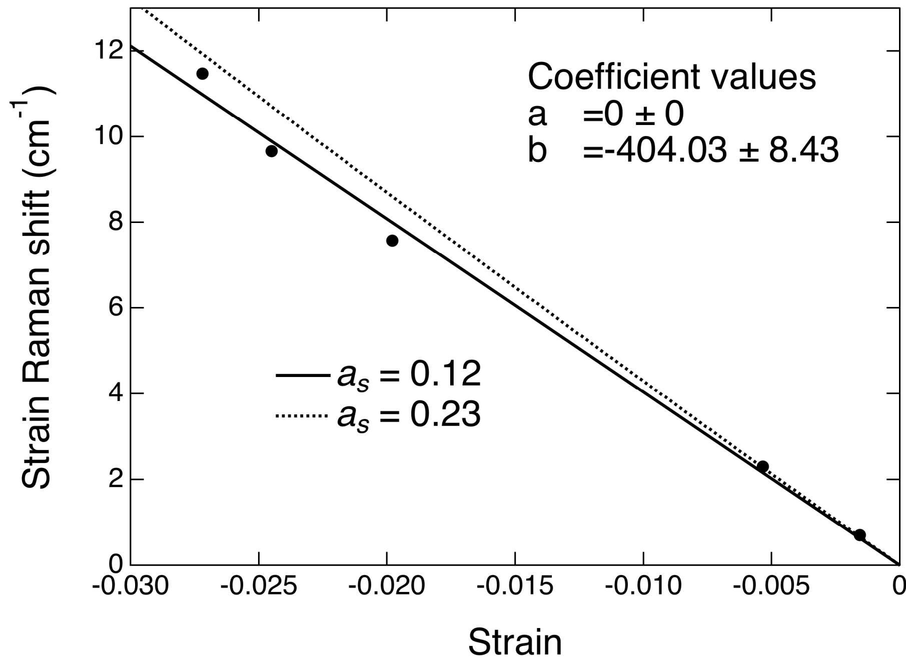

Figure 3.11 Plot of the strain-induced Raman shift of the Ge-Ge LO phonon in strained Ge. The three data points with high strain values correspond to our own data ,with strains from K. Omote. The two points with low strain are from Pezzoli (private communication).

The solid line in Fig. 3.11 is a combined fit to our data (with a small confinement correction) and Pezzoli's data. We find $b = 404 \pm 8$ cm^{-1}, below the Pezzoli value $b = 440\pm8$ cm^{-1}. The dotted line in Fig. 3.11 corresponds to the recommended valued $a_s = 0.23$ in Table 3.4. Our lower value of b implies a much smaller $a_s = 0.12$. However, it is apparent from an inspection of Fig. 3.11 that the number of data points is too small to conclude with certainty that a smaller a_s value is needed to fit the data. In fact, the deviations of the individual points from the straight line fit are not much smaller that the difference between the $a_s = 0.10$

and $a_s = 0.23$ prediction. More data points are needed to reach a definitive conclusion.

It is interesting to point out that other workers find even smaller magnitude b's for Ge. Canonico (thesis) explores strains comparable to ours and finds $b = -369 \pm 8$ cm^{-1}, from which one gets $a_s \sim 0$, which seems far too low. Moreover, from very recent wafer bending experiments by Peng et al.[59] imply an even lower value of $b = -350$ cm^{-1}.

3.10 Conclusion

We have proposed a new set of parameters p and q that are internally consistent and also consistent with all available experimental data from all sources from which information about these parameters could be obtained before our experimental work. We have also presented new data for Ge and shown a deviation from the proposed new parameter set. These deviations appear modest in the scale of Fig. 3.11, but imply a very different set of values for p and q. It is apparent for the Fig. 3.11, however, that more data points are needed to confirm a deviation. While it is not possible to draw definitive conclusions from the present data, our experiments, combined with the quoted results from Canonico and the more recent data from Peng, suggests the tantalizing possibility that the parameter a_s may have a strain dependence. (001) backscattering Raman measurements, for which only the singlet is observed, are a poor way to explore these possible anomalies, since the shifts are mainly determined by the hydrostatic component of

the strain. What is needed is experiments on lateral (110) faces from which the position of both the single and doublet can be measured.

CHAPTER 4

VIBRATIONAL PROPERTIES OF GeSn ALLOYS

4.1 Introduction

$Ge_{1-x}Sn_x$ alloys are currently of growing interest since their band gap can be engineered by varying the alloy composition. They are a possible route to making optoelectronic systems entirely from group IV materials. Jenkins and Dow[60] have predicted the creation of a direct band gap $Ge_{1-x}Sn_x$ alloy with the composition ranging from $0.2 < x < 0.6$. Ge is used as a material for photodetectors and multi-junction solar cells[61] and can be integrated with Si, but since it is not a direct band gap material it cannot be used as the basis for optical emission devices such as LEDs and lasers. $Ge_{1-x}Sn_x$ alloys present the possibility of producing direct band gap materials directly on Si which are tunable over a wide range of energies. To be able to engineer the properties of the $Ge_{1-x}Sn_x$ alloy it is important that we have the means to determine the Sn composition of the alloy accurately. Raman spectroscopy is a quick, non-destructive and contactless technique to measure the alloy composition since the optical modes of the alloy are strongly affected by composition. The group IV semiconductors have characteristic zone center vibrational mode frequencies. If we know the composition dependence of the phonon frequencies, then the composition of the alloys can be obtained with high accuracy, provided we exclude other effects which can also shift the mode frequencies.

In this chapter we discuss the compositional dependence of the Ge-Ge mode of the Raman spectrum of the $Ge_{1-x}Sn_x$ alloy. We have applied strain corrections to the Raman shift in order to decouple the composition and strain contributions.

4.2 Germanium

From Germanium's band structure diagram (Figure 4.1) we can see that it is an indirect band gap material. Its fundamental energy gap is the separation between the minimum of the conduction band L point [k = (2π/a)(1/2,1/2,1/2)] of the Brillouin zone (BZ) and the maximum of the valence band at the Γ-point [k=0,0,0], having a magnitude of 0.66 eV [62]. The lowest direct band gap[42] in Ge, involves the local minimum of the conduction band at the Γ-point and is 0.13 eV higher than the indirect band gap.

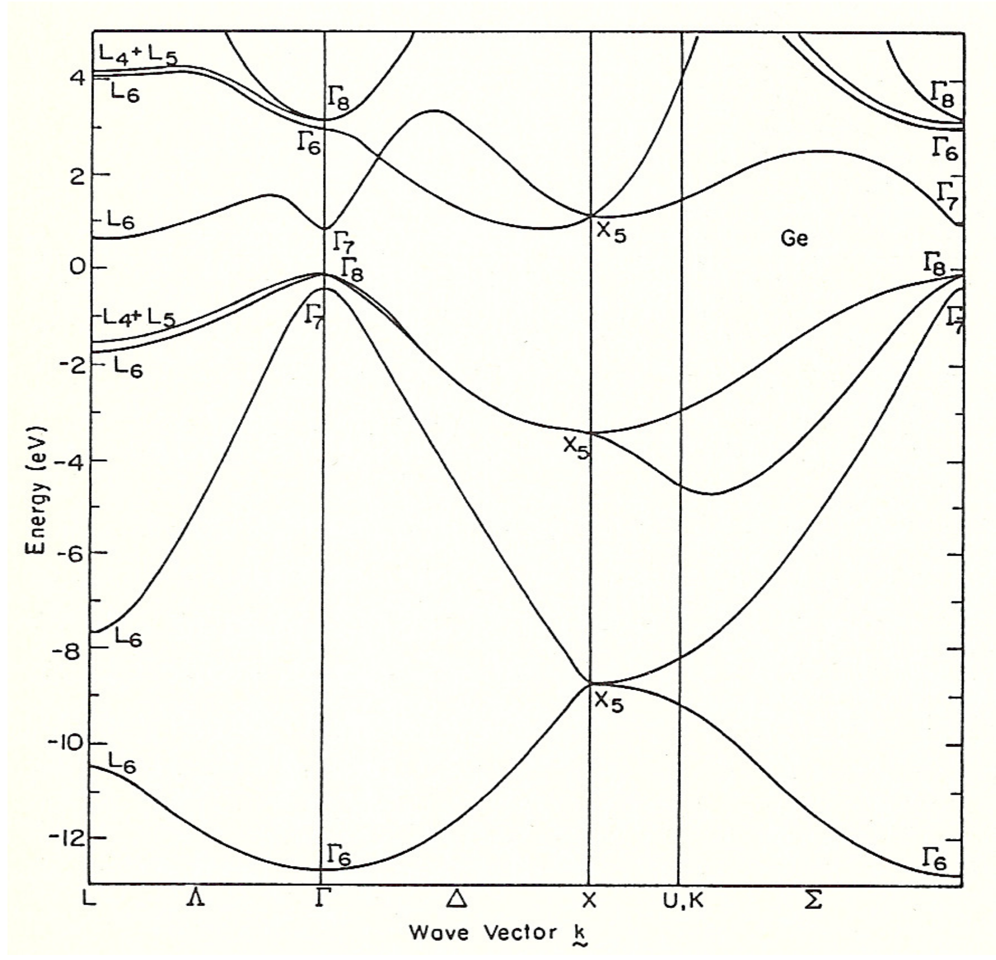

Figure 4.1 Electronic band structure of Ge. Reprinted, with permission, from *Electronic Structure and Optical properties of Semiconductors* (Springer-Verlag Berlin Heidelberg, New York 1988).

For optical transitions to occur both energy and crystal momentum have to be conserved. But at the indirect gap, the small k-vector of the photons is insufficient to satisfy crystal momentum conservation for the electron. The additional momentum required is provided by the lattice vibrations, the phonons.

Therefore, at the indirect band edge, the energy and momentum conservation describing the absorption of a photon requires that [63]

$$E_f = E_i + \hbar\omega \pm \hbar\Omega \quad (4.1)$$

and

$$\hbar\mathbf{k}_f \approx \hbar\mathbf{k}_i \pm \hbar\mathbf{q} \quad (4.2)$$

where E_i and $\boldsymbol{k}_i$ are the initial energy and wave vector of the electron, E_f and $\boldsymbol{k}_f$ are the final energy and wave vector of the electron after it absorbs a photon of frequency ω, (here we have neglected the momentum of the photon, since it is very small when compared to the momenta of the electron and the phonon), and Ω is the frequency of the phonon with wave vector q. The '+' sign indicates that a phonon has been absorbed, while the '-' sign indicates that a phonon has been emitted.

Since indirect absorption is a higher-order process involving not only the electron-photon but also the electron-phonon interaction, the absorption coefficient near the indirect band edge is much lower than that near the direct band edge, where phonon activity is not required for momentum conservation. In Ge, the indirect gap is 0.13eV smaller than the direct gap at k = 0[42] at room temperature. Below the indirect gap there is almost no absorption. Beyond that, the absorption gradually increases with energy until the direct gap is reached, where there is an abrupt increase in absorption (direct absorption edge).

The indirect and direct band gaps can be reduced in Ge by applying tensile strain to it. As a result, the absorption edge of Ge will shift to lower energies.

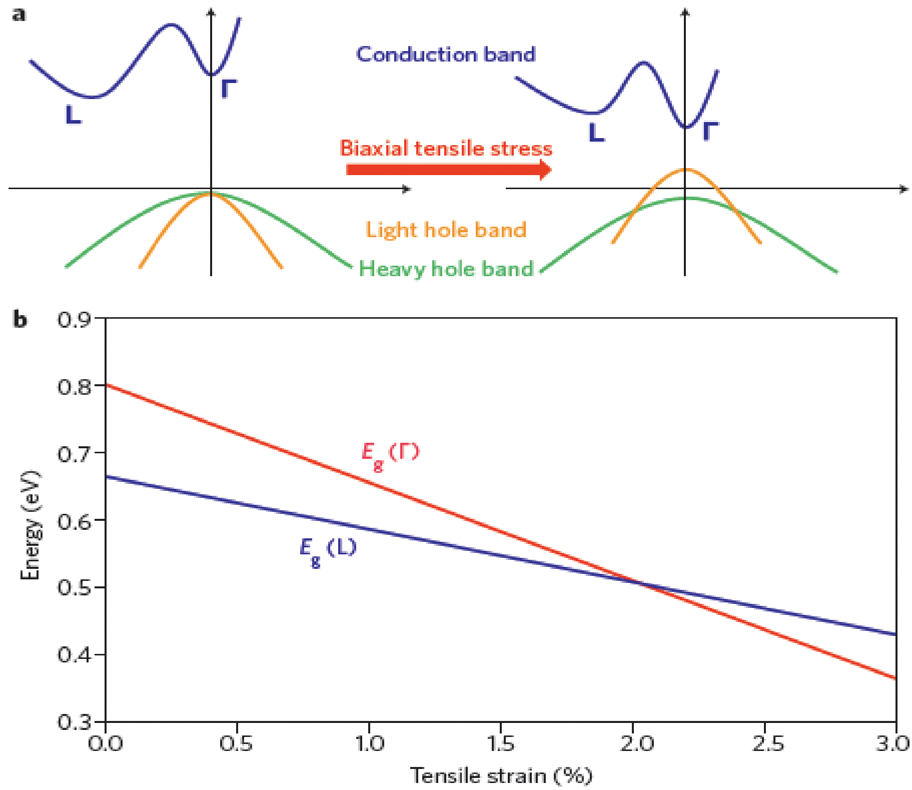

Figure 4.2 (a) Transition from indirect to direct band gap in Ge with the application of biaxial tensile strain. (b) Energy gaps in Ge at the Γ- and L- points as a function of tensile strain. Reprinted, with permission, from Nature Photonics, 4, 527 (2010).

In figure 4.2 the energy gaps in Ge at the **L**- and **Γ**- points as a function of tensile strain are plotted. We see that as the strain increases the energy of the gap at the **L**-point falls at a slower rate than the energy of the gap at the **Γ**-point. This implies that with increasing tensile strain there is a decrease in the energy difference between the the **L**- and **Γ**- points. So the band structure of Ge should transition to a direct gap material beyond a critical strain value[64]. From the plot in figure 4.2 we see that this occurs at around 2% strain.

High quality, tensile-strained thin films of Ge have been obtained by Ishikawa et al.[65] by growing Ge on Si. However, they found that the maximum amount of strain produced this way is only 0.34%. Huo et al.[66] have grown thin Ge films with tensile strain varying from 0.26% to 2.33% using graded InGaAs buffer layers. Since the 1980's many attempts have been made to grow Ge on Si epitaxially. But due to the 4.2% lattice mismatch between Ge and Si, it leads to unacceptable levels of threading dislocation densities[67, 68].

It has been shown that $Ge_{1-x}Sn_x$ alloys with high crystallinity can be grown with Sn concentrations as high as 15%[16]. This is a promising way to grow semiconductor materials tunable over band gap energies of 0 – 0.66eV.

4.3 GeSn alloys

Sn occurs in two forms. It has a tetragonal structure at room temperature (white tin or β-Sn), and a diamond cubic structure (grey tin or α-Sn) below 13.2°C. Groves and Paul[69] were the first to calculate the band structure of α-Sn in 1963. Figure 4.3 shows the electronic band structure of α-Sn. Pure α-Sn is a semimetal, ie. it has no band gap. Its valence and conduction bands overlap at the [**k** = (0,0,0)] **Γ** point.

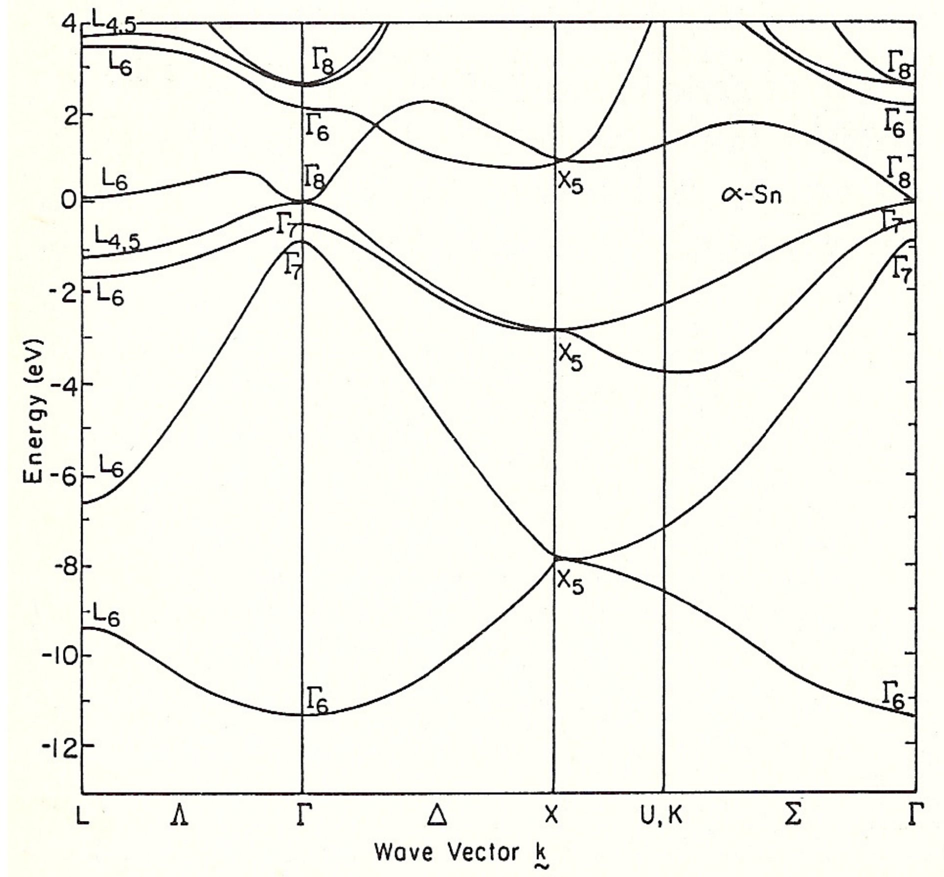

Figure 4.3 Electronic band structure of α-Sn. Reprinted, with permission, from *Electronic Structure and Optical Properties of Semiconductors* (Springer-Verlag Berlin Heidelberg, New York, 1988).

With the addition of α-Sn in Ge, the direct band gap of Ge decreases until it reaches zero. At that point GeSn becomes a semimetal. Up to that critical point GeSn should behave like a semiconductor with a fundamental gap having an energy range from 0.0eV to 0.76 eV, depending on the composition.

Hence, by alloying Ge with Sn we can grow direct band gap materials, directly on Si, over a range from 0eV to 0.76eV. This is a better alternative to achieving direct band gap by applying tensile strain in Ge-on Si films, where a

2% strain [65] is required to bring in the transition from indirect to direct whereas only 0.34% strain has been obtained by applying tensile strain [66].

4.4 Structural effects in GeSn alloys

The average lattice constants of semiconductor alloys follow Vegard's law[70] quite closely. We can then write the lattice constant of $Ge_{1-x}Sn_x$ as

$$a(x) = (1-x)a_{Ge} + xa_{Sn} \quad (4.3)$$

where a_{Ge} and a_{Sn} are the lattice constants of Ge and Sn respectively. This linear interpolation between the lattice parameters does not necessarily apply to the bond lengths[31]. Pauling [71] proposed that atomic radii are conserved quantities and remain unchanged in different chemical environments. This suggests that the bond lengths will be composition independent. The only way this is compatible with an average lattice parameter following Vegard's law, is via a severe distortion of bond angles. On the other hand, if the bond lengths themselves follow Vegard's law, the bond angles maintain their diamond-structure values at all compositions. The behavior of GeSn can be explained by adopting a degree of bond relaxation which lies between these two extremes. This is quantified by the topological rigidity parameter (or the bond relaxation parameter) defined for $A_{1-x}B_x$ alloy as [31, 32]

$$a^{**} = \frac{R_{AA}(x) - R_{BB}(x)}{R_{AA}^0 - R_{BB}^0} \quad (4.4)$$

where $R_{AA}(x)$ and $R_{BB}(x)$ are the A-A and B-B bond lengths in the alloy respectively and R_{AA}^0 and R_{BB}^0 are the bond lengths in bulk A and B respectively. From equation (4.4) we find that $a^{**} = 0$ in Vegard's limit and

$a^{**} = 1$ in Pauling's limit. Martin and Zunger [31] calculated a^{**} for GeSn to be 0.67.

4.5 Experimental details

The samples were grown on Si wafers using a specially developed CVD method in which Ge_2H_6 is combined with SnD_4 in the presence of high purity H_2 [72]. The Sn concentrations were determined using Rutherford Backscattering experiments. XRD measurements were done to measure the lattice parameters using a Panalytical X'Pert system.

The Raman spectra were collected at room temperature (experimental setup as shown in figure 3.7) in the backscattering configurations, $z\,(x, y)\,\bar{z}$ and $z\,(x, x)\,\bar{z}$; where x, y and z correspond to the 100, 010 and 001 crystal directions respectively. A 532 nm laser line from a frequency doubled Nd:YAG laser with excitation power of 1mW was focused onto the sample with a microscope using a 100X objective lens. A single Acton monochromator and a liquid nitrogen-cooled charge coupled device detector was used to analyze the scattered light.

4.6 Results

Figure 4.4 shows a typical Raman spectrum obtained with a 532nm laser line for a representative $Ge_{1-x}\,Sn_x$ alloy at room temperature. In analogy with the extensively studied $Si_{1-x}Ge_x$ alloys, we expect Raman peaks corresponding to Ge, Ge-Sn and Sn-Sn modes.

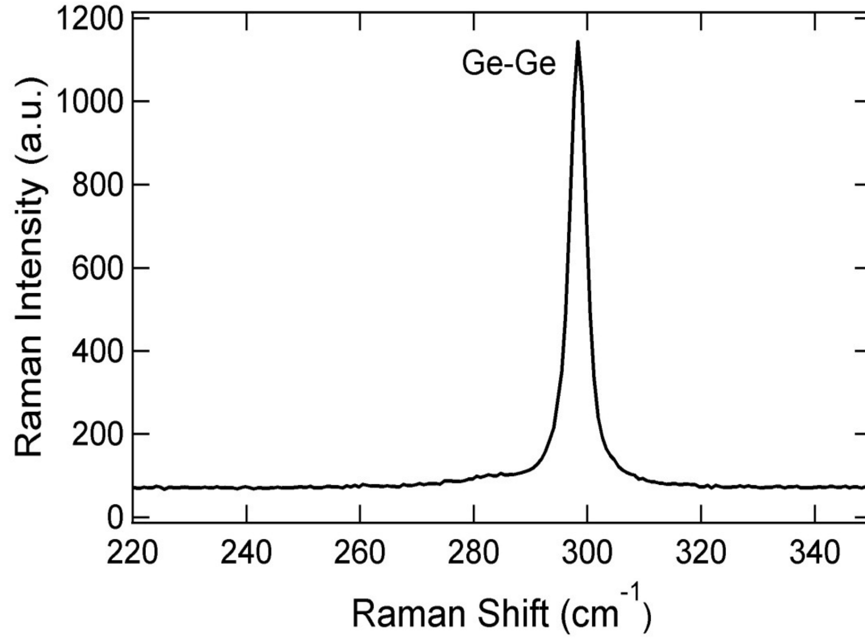

Figure 4.4 Raman spectra of $Ge_{0.985}Sn_{0.015}$ alloy in $z\,(x,y)\,\bar{z}$ geometry.

The Raman spectrum of each GeSn sample shows a strong peak corresponding to the Ge-Ge phonon mode. The reason that we do not observe the Ge-Sn and the Sn-Sn modes is due to the low Sn concentration and because the 532nm laser line is not in resonance with the $E_1/\,E_1+\,\Delta_1$ gap of the GeSn alloys. We also observe a disorder-activated (DA) Ge-Ge mode shown in figure 4.5 which was first reported for pure Ge in Si-Ge superlattices by Schorer et al[73] in the $z\,(x,\,x)\,\bar{z}$ geometry.

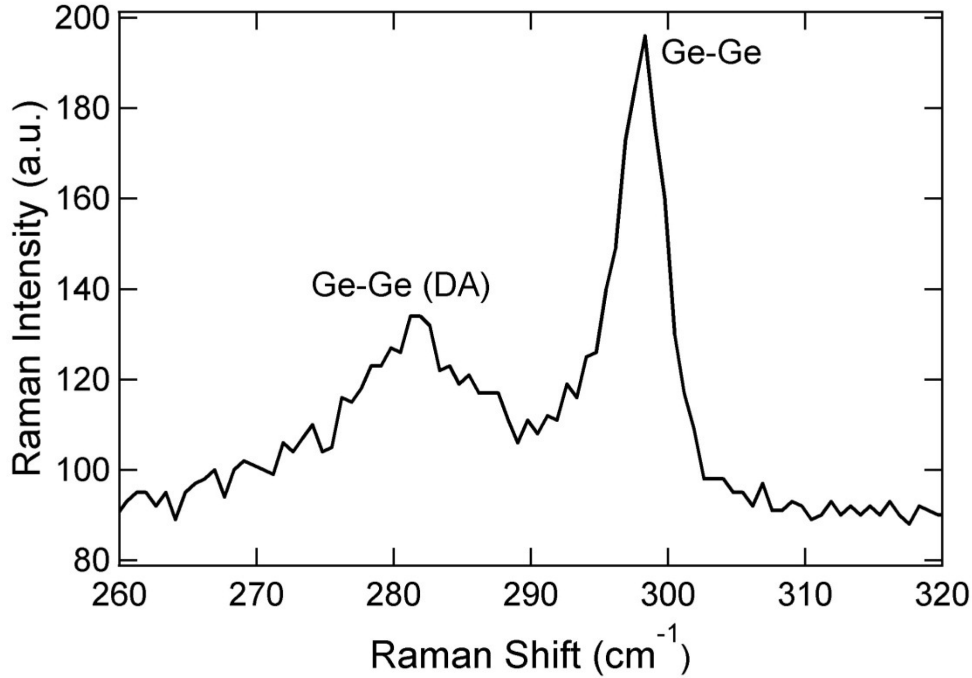

Figure 4.5 Raman spectra of $Ge_{0.985}Sn_{0.015}$ alloy in $z\ (x, x)\ \bar{z}$ geometry.

The observed Raman modes show a slight asymmetry in their shape. This is attributed to the fact that in the absence of a perfect translational symmetry in the alloy, the wavevector is no longer conserved. Also, the requirement of off-resonance Raman scattering is not strictly satisfied. The laser energy used is higher than the band gap energy of the GeSn alloys. The strong absorption of the laser light acts mathematically as adding an imaginary component to the photon wave vector, and this relaxes the wavevector conservation condition, activating other optical phonons with frequencies below that of the Γ- point phonon[74], contributing to the asymmetry in the Raman line shape.

The Raman spectra of bulk Si, Ge, and α-Sn are well approximated by a Lorentzian lineshape. The experimentally observed spectrum is the convolution of this Lorentzian with the instrument's response function, which can be reasonably well described by a Gaussian. The resulting Voigt profile[75] is available as a fitting function in most commercial data analysis software packages, so that the intrinsic widths can be extracted directly from fits with these functions. Alternatively, it has been shown that the intrinsic component of the width is related to the width of the instrument resolution function by[76]

$$\Gamma = \Gamma_{exp} - \frac{\Gamma_G^2}{\Gamma_{exp}} \tag{4.5}$$

where Γ is the intrinsic (approximately Lorentzian in the case of a perfect crystal) full width at half maximum (FWHM), Γ_G the FWHM of the instrument resolution function, and Γ_{exp} the measured FWHM. This formula can then be used to obtain Γ from the measured data without formally fitting with a Voigt profile.

The analysis of the lineshape of alloy modes is much more complicated because, in addition to the lifetime and instrument resolution broadening, there is a broadening contribution from the intrinsic disorder and the relaxation of the wave vector conservation rule as just discussed. Unfortunately, there are no realistic analytical models that can be used to fit the data and correct for the instrument resolution. Therefore, we adopted the following approximate procedure. We first determine the FWHM of the Raman peaks by fitting with any function that gives good agreement with the data (usually a Voigt profile [75] if the peak looks symmetric or an exponentially-modified Gaussian[76] if the peak is

asymmetric). Then we assume that we can still use equation (4.5) to correct for the instrumental broadening, even though equation (4.5) has been shown to be valid when the intrinsic lineshape is Lorentzian. This approach may introduce a small systematic error, but it will not alter the results in any significant way. In fact, the qualitative conclusions of this work would not change if we were to ignore instrumental broadening altogether and assume it part of the intrinsic width.

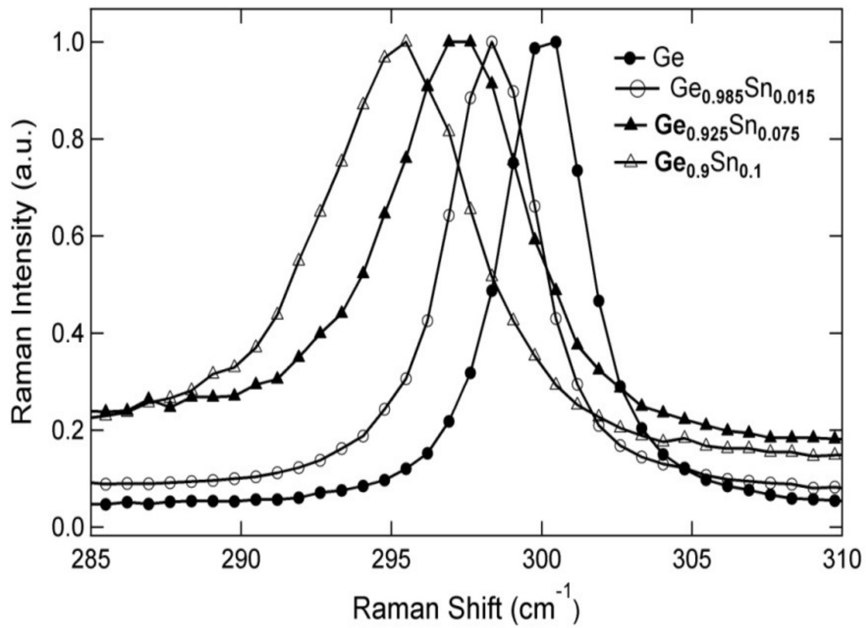

Figure 4.6 Normalized Ge-Ge mode in $Ge_{1-x}Sn_x$ alloys.

Figure 4.6 shows the Ge-Ge vibrations in the GeSn alloys for various Sn concentrations. The spectra were recorded in the $z\,(x,\,y)\,\bar{z}$ configuration. The Ge-Ge peak for each alloy configuration is downshifted with respect to pure Ge. The

vibrational frequencies decrease with increasing Sn concentrations. This decrease in frequency is due to the effect of mass substitution and Ge-Ge bond distance elongation which decreases the phonon frequency.

Since the alloys have a small amount of strain, strain corrections are applied to the Raman frequencies. Strain-induced shifts are calculated by assuming a tetragonal distortion and then subtracting them from the observed Raman shifts. This gives the Raman shifts of the relaxed alloy. Strain induced shifts are calculated using the formula derived in chapter 2

$$\Delta\omega = b\varepsilon_{\parallel} \tag{4.6}$$

The value of b, the phonon strain coefficient, is approximately the same for all group-IV semiconductors. Hence we have used Ge values obtained experimentally in chapter 3.

To determine the strain present in the alloys, lattice constants were measured by HR-XRD using a PANalytical diffractometer. Reciprocal space maps of the (224) reflection were used to determine the a (in-plane) and c (perpendicular) tetragonal lattice parameters of the GeSn samples. Then the relaxed cubic lattice constant was calculated using the equation

$$a_0 = \frac{c + \frac{2C_{12}}{C_{11}} a}{1 + \frac{2C_{12}}{C_{11}}} \tag{4.7}$$

where C_{11} and C_{12} are the cubic elastic constants. Kouvetakis et al [77] have given the elastic constant ratio as

$$\frac{C_{12}}{C_{11}} = 0.3738 + 0.1676x - 0.0296x^2 \tag{4.8}$$

The strain is then calculated using the formula

$$\varepsilon = \frac{a-a_0}{a_0} \tag{4.9}$$

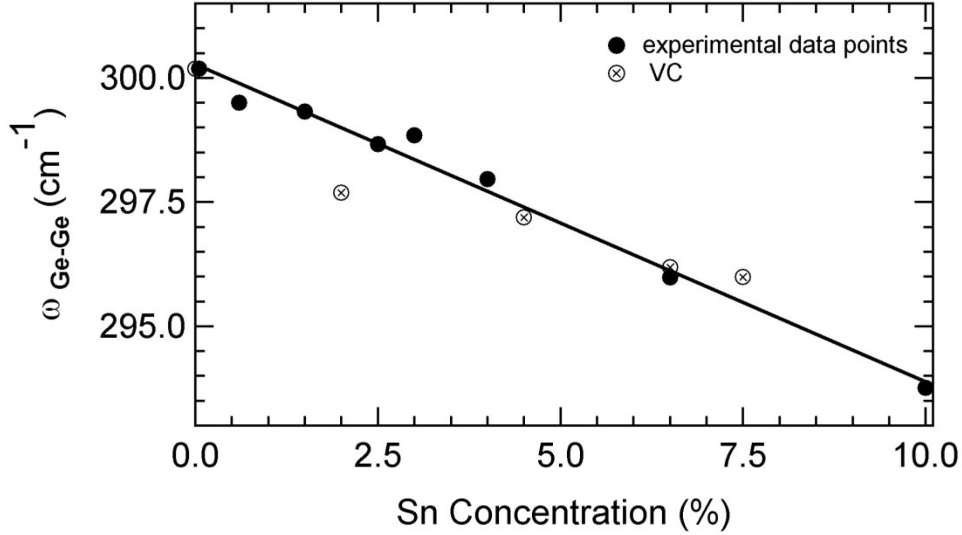

Figure 4.7 Dependence of Ge-Ge mode in the $Ge_{1-x}Sn_x$ on Sn concentration from reference 81 and present data.

Figure 4.7 is a plot of the Ge-Ge mode frequency as a function of Sn concentration. The compositional dependence of Raman peaks in alloy semiconductors can be explained as a combined effect of mass and bond disorder[27]:

$$\Delta\omega(x) = \Delta\omega^{mass}(x) + \Delta\omega^{bond}(x) \tag{4.10}$$

where $\Delta\omega^{mass}$ is the Raman shift due to mass disorder which arises from different masses of the atoms involved and $\Delta\omega^{bond}$ is the Raman shift due to bond disorder which arises when the atoms try to adjust their bond length mismatch during alloying.

Different masses cause a localization of the vibrations. If we consider the Ge-Ge mode, the Sn atoms will be unable to follow the motion of the Ge-Ge mode because of their heavier mass compared to that of Ge. Since some Ge atoms have Sn neighbors, this leads to a localized Ge-Ge vibration. This localization leads to a reduction of the Ge-Ge mode frequency. Meléndez-Lira[30] found the mass term to be proportional to the alloy fraction $\boldsymbol{x}$

Due to bond distortion a microscopic strain is introduced in the alloy. If a tensile strain is produced by the lengthening of the bonds, it will result in the reduction of the frequency of the associated Raman mode and vice versa. The bond distortion was calculated by Gironcoli[78] by considering the displacements of only near-neighbor bonds. So the compositional dependence of the corresponding Raman peak can be written as[79]

$$\Delta\omega(x) = -A\omega_0 x - B\omega_0 \frac{\Delta R(x)}{R_0} \qquad (4.11)$$

where A and B are constants. For the Ge-Ge mode, $\boldsymbol{x}$ is the Ge concentration, ω_0 is the bulk Ge Raman frequency and R_0 is the bulk Ge bond length. Here $\Delta R(x) = R(x) - R_0$, and $R(x)$ is the Ge-Ge bond length in the alloy. The bond length can be written [80] in terms of the lattice constant $a(x)$ and the bond rigidity parameter a^{**}[32] as

$$\frac{\Delta R(x)}{R_0} = (1 - a^{**})\frac{\Delta a(x)}{a_0} \qquad (4.12)$$

Here $\Delta a(x) = a(x) - a_0$, and $a(x)$ is the lattice constant of Ge in the alloy.

So equation (4.11) can be rewritten as

$$\Delta\omega(x) = -A\omega_0 x - B\omega_0(1 - a^{**})\frac{\Delta a(x)}{a_0} \qquad (4.13)$$

Hence we fit the data in figure 4.7 with an expression of the form[81]

$$\omega_{Ge-Ge}(x) = \omega_0 - \beta x \qquad (4.14)$$

From the model fit we obtain the expression

$$\omega_{Ge-Ge}(x) = 300.3 \pm 0.1 - (64.0 \pm 3.2)x \qquad (4.15)$$

which is in close agreement with Li's [83] fit of

$$\omega_{Ge-Ge}(x) = 301 - 68x \qquad (4.16)$$

The difference between the two expressions may be explained by the strain correction applied in our analysis which was not included by Li et al. In figure 4.7 we have plotted the Raman shifts obtained by V. d'Costa [81] as a function of Sn concentrations.

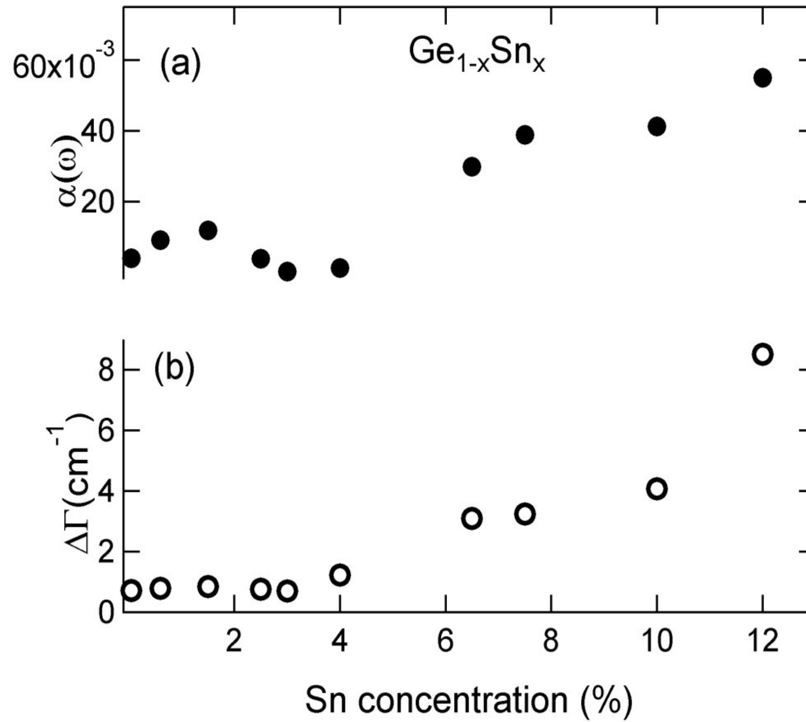

Figure 4.8 (a) Plot of the asymmetry in the lineshapes as a function of Sn concentration and (b) Plot of the difference between the linewidths of the Ge-Ge Raman peaks and bulk Ge.

Figure 4.8 (b) shows the plot of the difference between the linewidths of the Ge-Ge mode and bulk Ge. It appears that the broadening is approximately constant for $0 < x < 0.04$, and it grows rapidly for $x > 0.04$. This coincides with the appearance of the typical alloy asymmetries in the lineshapes, consisting of a broadening of the low-energy side. One way to quantify this asymmetry is to fit the experimental spectrum with a symmetric lineshape $I_{sym}(\omega)$ and define an asymmetry indicator $\alpha(\omega) = [I_{sym}(\omega_0+\Gamma_{exp}) - I(\omega_0+\Gamma_{exp})]/I_{sym}(\omega_0+\Gamma_{exp})$. This function is shown in figure 4.8(a). The observation of asymmetric Raman peaks is a manifestation of the relaxation of the wave vector conservation rule. Vibrational

modes with frequencies close to the bulk Raman mode become Raman-active, but since the bulk Raman mode corresponds to the highest frequency optical phonon, all activated modes have lower frequency, thus appearing as a broadening of the low-energy side of the Raman peak [82].

4.7 Conclusion

We have measured the vibrational properties of $Ge_{1-x}Sn_x$ alloys using Raman spectroscopy. We observe the Ge-Ge and the disorder-activated Ge-Ge mode at ~ 280 cm^{-1}. We have determined the compositional dependence of the Ge-Ge mode. This can act as a reference for accurately determining the composition of a given $Ge_{1-x}Sn_x$ alloy by measuring its Raman spectrum.

CHAPTER 5

TEMPERATURE DEPENDENCE OF THE RAMAN MODES IN GeSn AND SiGeSn ALLOYS

5.1 Introduction

Temperature dependent Raman scattering provides a very useful tool for the study of anharmonic properties of crystal vibrations[83, 84, 85] and has been used in diagnostic applications, like *in situ* measurements of temperature [86]. Raman spectroscopy acts as a temperature microprobe. This microprobe can be used to measure the local temperature of devices under operation[87]. Since heating is one of the main causes for device failure, measurement of the local temperature is of great significance. Such measurements have been made in biased laser diodes using a Raman microprobe[88]. Temperature measurements can be done by measuring the Stokes / anti-Stokes intensity ratio[89]. However, these temperature measurements might not be accurate as several corrections need to be applied. Raman frequency and linewidth are also strongly temperature dependent [21] and hence can be used as parameters for temperature measurements with greater simplicity and accuracy. Ostermeier et al [88] have used the temperature dependence of phonon frequencies to study the temperature distribution in Si-MOSFETs.

The use of temperature dependent frequency and linewidth for diagnostic studies require a knowledge of the evolution of these parameters with temperature for the material under study. We have established in the previous chapter, the role GeSn alloys are going to play in devices in the near future. It is also of benefit to

present the temperature dependent frequency and linewidth measurements for GeSn alloys for device applications. These studies are important for understanding the vibrational properties of the GeSn alloys and would help in understanding/manipulating the heat dissipation in devices based on these materials.

In this chapter we have studied the temperature induced changes in the Ge-Ge mode of $Ge_{1-x}Sn_x$ and $Si_{1-x-y}Ge_ySn_x$ in the temperature interval 10K to 450K.

5.2 Alloy Vibrational Structure

Localized optical vibrations are characteristic of alloys on account of the mass difference of the alloy components. But these do not convey the full complexity of the alloy vibrational structure. In fact, in many alloy systems it is possible to define "quasi-dispersion" relations for optical and acoustic phonon branches[90, 91]. The approximate validity of this concept in $Si_{1-x}Ge_x$ alloys and similar systems is apparent when one studies the lineshape of their Raman modes, which are broader than those in the perfect crystals but much narrower than the Raman bands observed in amorphous materials. This indicates that the crystal momentum conservation rule $\boldsymbol{q_0} \approx 0$, valid for the wave vector of Raman-active modes in perfect solids, is only partially relaxed in tetrahedral semiconductor alloys. Similarly, phonon confinement effects akin to those observed in single crystal materials are seen in thin alloy films [92].

The quasi-dispersion concept is expected to play an important role in the lifetime broadening of the Raman modes. In perfect Ge and Si crystals, the width of the Raman peak at room temperature and below is essentially determined by the anharmonic decay of the Raman-active phonon of frequency ω_0 into pairs of phonons of frequencies ω_1 and ω_2[21]. Energy conservation requires $\omega_1 + \omega_2 = \omega_0$, and crystal momentum conservation implies $\boldsymbol{q_1} + \boldsymbol{q_2} = \boldsymbol{q_0} \approx 0$. In alloy systems the energy conservation rule remains valid, but the crystal momentum rule could be relaxed. Debernardi et al. have used ab initio methods to study anharmonic phonon decay in Si and Ge[25]. They find that the many pairs of modes which satisfy the two conservation conditions cluster around frequencies $\omega_1 = 0.35\omega_0$ and $\omega_2 = 0.65\omega_0$, as previously proposed to explain the temperature dependence of the Raman linewidths [27]. At these frequencies the phonon density of states for transverse acoustic (TA) and longitudinal acoustic (LA) phonons are quite high, suggesting that a relaxation of the momentum conservation rule by the alloying effect should activate many nearby states which have the “right” frequencies but the “wrong” wave vectors to participate in the decay. This should result in a stronger temperature dependence of the Raman linewidth. Calculated phonon density of states (dashed line) and the *frequency-resolved final state spectrum* (which is the probability per unit time that the LTO phonon decays into one mode of frequency ω and one of frequency $\omega_0 - \omega$) are plotted in figure 5.1 for Ge [25].

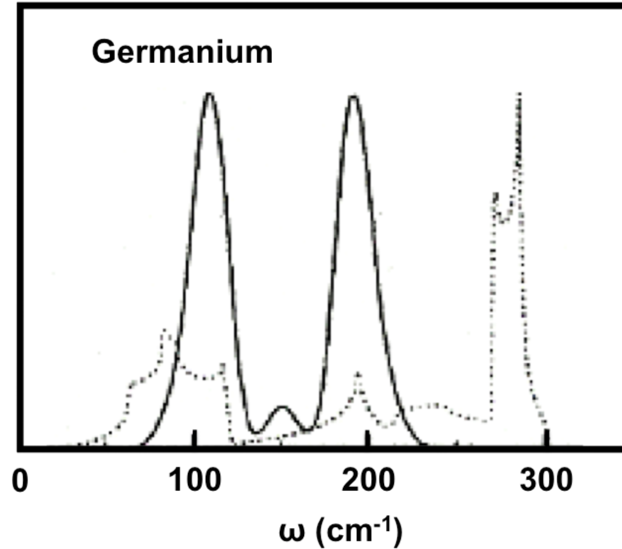

Figure 5.1 Calculated phonon density of states (dashed line) and *frequency-resolved final state spectrum* for Ge (solid line) at zero temperature and pressure. Reprinted with permission[96] . Copyright (1995) by the American Physical Society.

The temperature dependence of the Raman spectrum of $Si_{1-x}Ge_x$ alloys has been studied in detail by Burke and Herman[92]. Quite surprisingly, these authors find that the linewidth of the Si-Si and Ge-Ge modes in the alloy has essentially the same temperature dependence as in bulk Ge and Si. On the other hand, differences in the temperature dependence of the alloy modes relative to the parent semiconductors have been observed by Jiménez and co-workers[93] for the GaAs-like modes in Al-rich $Al_xGa_{1-x}As$ alloys as well as by Verma et al for P-implanted GaAs[94]. These examples suggest that the alloy perturbation might be too weak in $Si_{1-x}Ge_x$ alloys to affect the temperature dependence of the Raman widths. Our study of the temperature dependence of the Ge-Ge mode shifts and

widths in Ge_{1-x} Sn_x and $Si_{1-x-y}Ge_ySn_x$ alloys will put this hypothesis to test.

5.3 Experiment

Our $Ge_{1-x}Sn_x$ samples were grown using the Chemical Vapor Deposition method (as in the previous chapter) introduced by Bauer *et al*[16]. The films are deposited directly on Si using via reactions of Ge_2H_6 with appropriate amounts of SnD_4 at ~350 °C. The ternary $Si_{1-x-y}Ge_ySn_x$ alloys were grown by the same method using SnD_4, Ge_2H_6 , and Si_3H_8 [17]. Raman measurements were performed from 10K to 450K in the near backscattering configuration (Raman setup shown in figure 3.6), $z\ (x, y)\ \bar{z}$; where x, y and z correspond to the 100, 010 and 001 crystal directions respectively using the 532nm line of a doubled Nd:YAG laser with excitation power of 25mW. The samples were mounted strain free in a closed cycle variable temperature cryostat. The collected scattered light was analyzed using an Acton 500 mm spectrometer and a Si CCD detector.

5.4 Results

Figure 5.2 shows the evolution of the Raman spectrum of a $Ge_{0.98}Sn_{0.02}$ sample as function of temperature. The spectra were recorded in the $z\ (x, y)\ \bar{z}$ configuration.

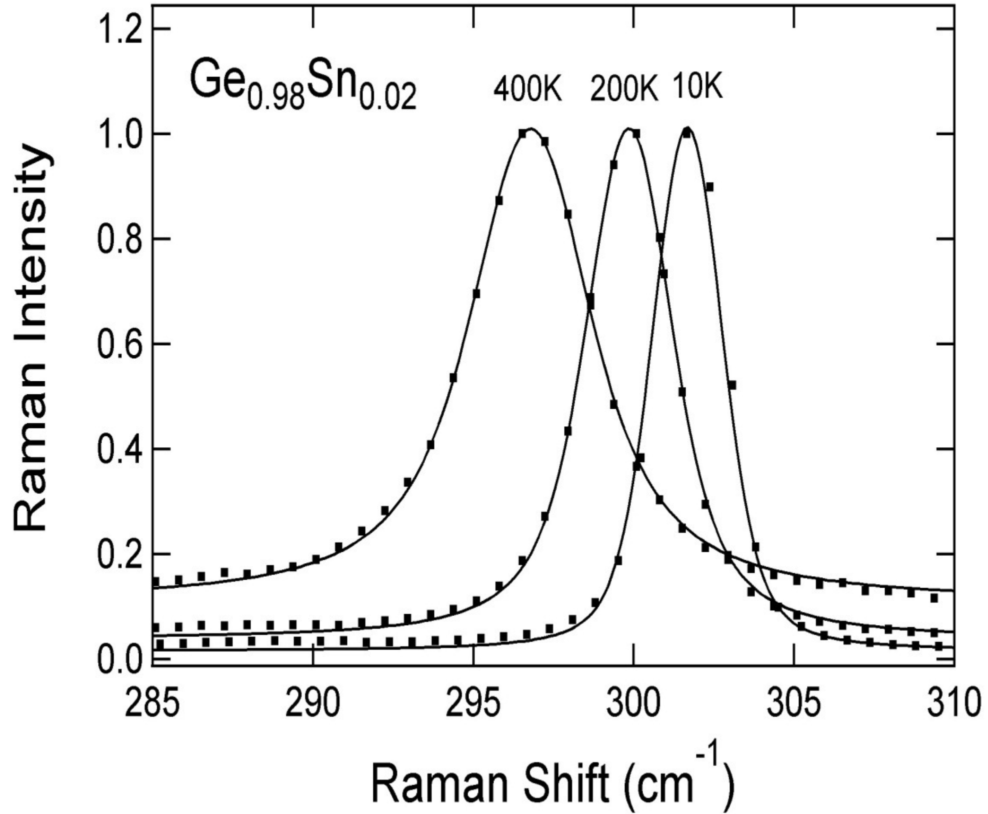

Figure 5.2 Raman spectrum of $Ge_{0.98}Sn_{0.2}$ obtained with 532 nm excitation at temperatures 10K, 200K and 400K.

We fitted the data using equation (4.5) from the previous chapter

$$\Gamma = \Gamma_{exp} - \frac{\Gamma_G^2}{\Gamma_{exp}} \tag{5.1}$$

where Γ is the intrinsic (approximately Lorentzian in the case of a perfect crystal) full width at half maximum (FWHM), Γ_G the FWHM of the instrument resolution function, and Γ_{exp} the measured FWHM, and followed the procedure therein to calculate the linewidths.

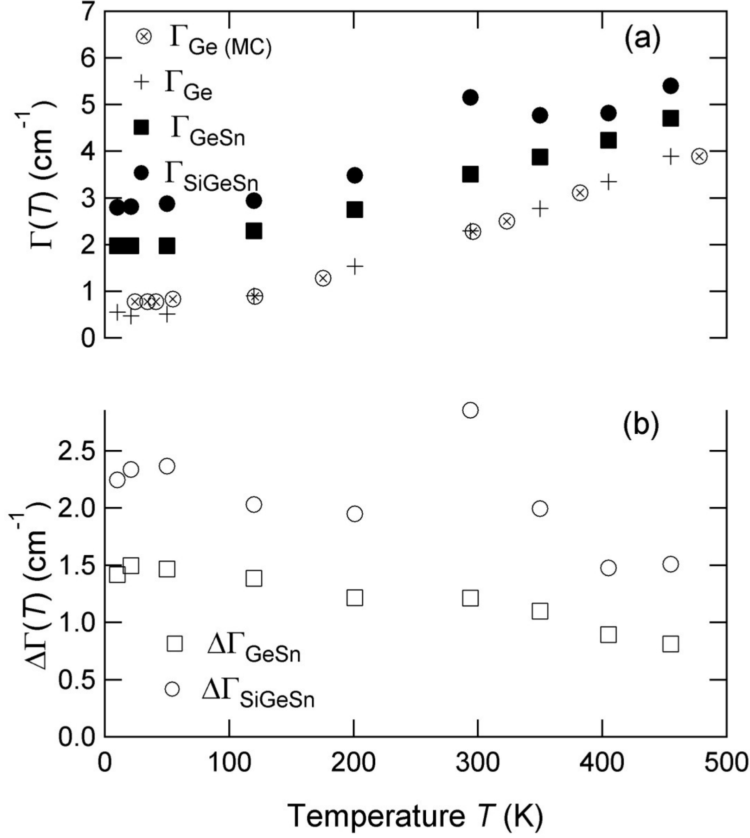

Figure 5.3 (a) Linewidths (FWHM) $\Gamma(T)$ for Ge (from Ref 21), Ge (present data), $Ge_{0.98}Sn_{0.02}$ and $Si_{0.09}Ge_{0.887}Sn_{0.023}$ as a function of temperature T. (b) Linewidth difference $\Delta\Gamma(T)$ between $Ge_{0.98}Sn_{0.02}$ and Ge and between $Si_{0.09}Ge_{0.887}Sn_{0.023}$ and Ge.

In figure 5.3 we plot the linewidths $\Gamma_{GeSn}(T)$, $\Gamma_{SiGeSn}(T)$, and $\Gamma_{Gen}(T)$ together with the differences $\Gamma_{GeSn}(T)-\Gamma_{Ge}(T)$ and $\Gamma_{SiGeSn}(T)-\Gamma_{Ge}(T)$, where all widths have been obtained following the procedure described in chapter 4.

In figure 5.4 we show the corresponding line shifts $\omega_{GeSn}(T)$, $\omega_{SiGeSn}(T)$, and $\omega_{Ge}(T)$ together with the differences $\omega_{GeSn}(T)-\omega_{Ge}(T)$ and $\omega_{SiGeSn}(T)-\omega_{Ge}(T)$ We see that all these differences are remarkably constant over the entire range of

temperatures studied here.

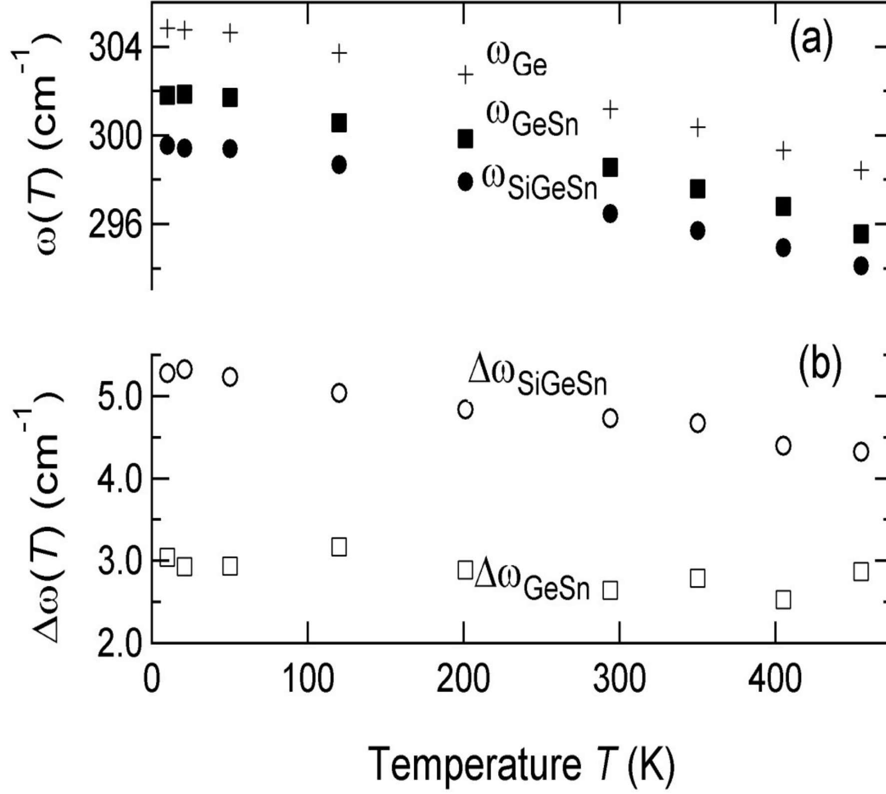

Figure 5.4 (a) Peak frequencies ω(*T*) of the Raman modes in Ge, $Ge_{0.98}Sn_{0.02}$ and $Si_{0.09}Ge_{0.887}Sn_{0.023}$ as a function of temperature *T*. (b) Line shift difference Δω(*T*) between $Ge_{0.98}Sn_{0.02}$ and Ge and between $Si_{0.09}Ge_{0.887}Sn_{0.023}$ and Ge.

In the case of the linewidth, it has been proposed that when an optical phonon of frequency ω_0 decays into two phonons of frequencies ω_1 and ω_2, the temperature dependence of the linewidth can be fit with an expression of the form[21]

$$\Gamma(T) = \Gamma_0\left[n(\omega_1) + n(\omega_2) + 1\right] \tag{5.2}$$

where $n(\omega) = \left[\exp\left(\frac{\hbar\omega}{kT}\right) - 1\right]^{-1}$ is the Bose-Einstein expectation number for a phonon of frequency ω_0 and Γ_0 is the linewidth at $T = 0$. In a rigorous derivation, the anharmonic linewdith is actually a sum of terms of the form (5.2), one for each pair of modes with frequencies ω_1 and ω_2 into which the Raman phonon of frequency ω_0 can decay [95]. However, this sum can be replaced by a single term if the possible decay frequencies cluster around a single value, as indicated above for the case of diamond-structure semiconductors. Under this simplification the coefficient Γ_0 is proportional to the sum of the squared moduli of the anharmonic matrix elements for each individual decay channel[21]. These matrix elements contain the crystal momentum conservation principle, that is, they vanish if $\boldsymbol{q}_1 + \boldsymbol{q}_2 \neq 0$. In the case of our alloys, we would expect the square bracket in Eq. (5.2) to remain the same as in bulk Ge, because the two frequencies $\omega_1 = 0.35\omega_0$ and $\omega_2 = 0.65\omega_0$ correspond to regions with high phonon density of states, and the density of states will not be dramatically altered by alloying. However, precisely because the density of states is high, there are many nearby phonon states whose matrix element cancels out due to crystal momentum conservation but should be able to participate in the decay process if this rule is relaxed by alloying. Thus we might expect an increase in Γ_0 as the main effect of alloying. However, this contradicts the results in figure 5.2, which clearly indicate that Γ_0 remains approximately the same as in bulk Ge. Thus the anharmonic decay process appears to be extremely robust against perturbations such as alloying.

The third-order anharmonic lineshift is Kramers-Kronig related to the third-order contribution to the lineshift [25], so we expect the differences $\omega_{\mathrm{GeSn}}(T) - \omega_{\mathrm{Ge}}(T)$ and $\omega_{\mathrm{SiGeSn}}(T) - \omega_{\mathrm{Ge}}(T)$ to be constant in view of the results for the linewidth. This is approximately the case from an inspection of figure 5.3. In the case of the $\omega_{\mathrm{SiGeSn}}(T) - \omega_{\mathrm{Ge}}(T)$ difference, we see a small deviation from the constant-shift behavior that can be approximated by a linear *T*-dependence. This may be due to the fact that thermal expansion and fourth-order terms, unrelated to the third-order perturbation, make a non-negligible contribution to phonon shifts[21].

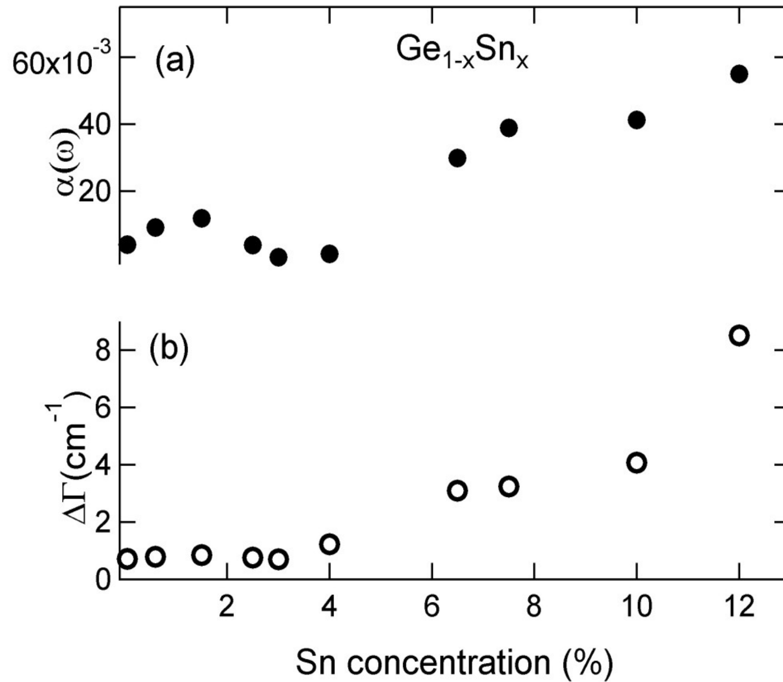

Figure 5.5 Plot of the difference between the linewidths of the Ge-Ge Raman peaks and bulk Ge and plot of the asymmetry in the lineshapes as a function of Sn concentration.

The temperature-independent difference between the width of the alloy Raman peaks and those of bulk Ge represent the alloy contribution to the width. This contribution is plotted in figure 5.4 (also plotted in figure 4.8 in chapter 4). For this plot we chose arbitrarily the value at 300 K, but in view of the lack of temperature dependence we could have chosen any other temperature. The broadening coincides with the appearance of the typical alloy asymmetries in the lineshapes. The observation of asymmetric Raman peaks is a clear manifestation of the relaxation of the wave vector conservation rule. Thus, while clear evidence is seen for a relaxation of the wave vector conservation rule in the Raman scattering process—corresponding to a (electron-mediated) photon-phonon interaction—there is no indication of a similar relaxation for the anharmonic decay process—corresponding to phonon-phonon interactions. While the first of these relaxations can be simulated by computing the Raman spectrum of large supercells with phonons calculated using *ab initio* methods, the latter requires an *ab initio* calculation of the anharmonic decay in large cells. Such calculations, which to the best of our knowledge have never been carried out, would shed light on the surprising temperature dependences reported here.

5.5 Conclusion

The lattice mismatch between Ge and α-Sn is 14%, as opposed to 4% in the Si-Ge system, so that Sn represents a much larger perturbation in Ge than Ge in Si. Even stronger disorder is present in the ternary alloy, where Sn atoms coexist with Si atoms. In spite of this enhanced alloy disorder, however, we find

that the temperature dependence of the Raman width and shift is the same, within experimental error, as the temperature dependence observed in bulk Ge. These results, combined with the earlier work of Burke and Herman [92], suggest that anharmonic decay in group-IV alloys is extremely robust against wave vector relaxation effects.

CHAPTER 6

CONCLUSIONS

6.1 Introduction

In this dissertation Raman spectroscopy has been used to study the vibrational properties of strained Ge films and GeSn alloys.

6.2 Strain-shift coefficient

The Raman shifts associated with strain are not related to the geometrical deformations in any obvious way, so that careful calibrations are needed to determine the anharmonic coefficients that relate strain to Raman shifts. In diamond structure systems, there are three such coefficients, denoted as p, q, and r, which are the components of a deformation potential tensor with the same symmetry as the elastic constants tensor, where the equivalent components are C_{11}, C_{12}, and C_{44}. We present a new set of measurements of the Raman shift in strained Ge films grown on relaxed SiGe buffer layers deposited on Si substrates. Combining these results with prior measurements and the accurate determination of the pressure dependence of Raman modes, we propose a new consistent set of values for the parameters p and q for Ge. While our proposal does not include the remaining quantity r, p and q are the only parameters needed to predict phonon shifts for strained-layer epitaxy.

6.3 Vibrational properties of GeSn alloys

The Raman spectra of the GeSn alloy shows the presence of the Ge-Ge optical mode and a disorder-activated Ge mode. We discuss the compositional

dependence of the Ge-Ge mode on the basis of a simple alloy model. We have also studied the temperature dependence of the lineshifts and the linewidths of the Ge-Ge mode. The broadening as a function of temperature is explained in terms of the thermal occupation number. The temperature dependence of the Raman spectrum of Ge-rich $Ge_{1-y}Sn_y$ and $Ge_{1-x-y}Si_xSn_y$ alloys has been determined in the 10 K -450 K range. The Raman line shift and width changes as a function of temperature are found to be virtually identical to those observed in bulk Ge, This result shows that the anharmonic decay process responsible for the temperature dependence is extremely robust against the alloy perturbation, so that the expected relaxation of the wave vector conservation rule does not affect the spectra in any noticeable way.

The temperature-independent difference between the width of the alloy Raman peaks and those of bulk Ge has been studied as a function of Sn concentration (x). It appears that the broadening is approximately constant for $0 < x < 0.04$, and it grows rapidly for $x > 0.04$. This coincides with the appearance of the typical alloy asymmetries in the lineshapes, consisting of a broadening of the low-energy side. The observation of asymmetric Raman peaks is a clear manifestation of the relaxation of the wave vector conservation rule. Vibrational modes with frequencies close to the bulk Raman mode become Raman-active, but since the bulk Raman mode corresponds to the highest frequency optical phonon, all activated modes have lower frequency, thus appearing as a broadening of the low-energy side of the Raman peak. Thus, while clear evidence is seen for a

relaxation of the wave vector conservation rule in the Raman scattering process—corresponding to a (electron-mediated) photon-phonon interaction—there is no indication of a similar relaxation for the anharmonic decay process—corresponding to phonon-phonon interactions. While the first of these relaxations can be simulated by computing the Raman spectrum of large supercells with phonons calculated using *ab initio* methods, the latter requires an *ab initio* calculation of the anharmonic decay in large cells. Such calculations, which to the best of our knowledge have never been carried out, would shed light on the surprising temperature dependences reported here.

REFERENCES

1. E. H. Parker, and E. Whall, Solid State Elec. 43, 1497 (1999).

2. R. Soref, IEEE J. 12, 1678 (2006).

3. B. Jalali, M. Paniccia, and G. Reed, IEE Microwave Magazine 7, 1440 (2006).

4. C. Auth, M. Buehler, A. Cappellani, C. Choi, G. Ding, W. Han, S. Joshi, B. McIntyre, M. Prince, P. Ranade, J. Sanford, and C. Thomas, Intel Tech. Journal 12, 77 (2008).

5. D. J. Paul, Semicond. Sci. Tech. 19, R75 (2004).

6. Y. Sun, S. E. Thompson, and T. Nishida, *Strain Effect in Semiconductors: Theory and Device Applications* (Springer Science+Business Media,) p 291. (2010)

7. E. A. Fitzgerald, Y.-H. Xie, M. L. Green, D. Brasen, A. R. Kortan, J. Michel, Y.-J. Mii, and B. E. Weir, Appl. Phys. Lett. **59**, 811 (1991).

8. E. A. Fitzgerald, Y.-H. Xie, D. Monroe, P. J. Silverman, J. M. Kuo, A. R. Kortan, F. A.Thiel, and B. E. Weir, J. Vac. Sci. Technol. B **10**, 1807 (1992).

9. A. R. Kortan, F. A. Thiel, J. Welser, J. L. Hoyt, and J. F. Gibbons, IEEE Electron Device Lett.15, 100 (1994).

10. M. T. Currie, C. W. Leitz, T. A. Langdo, G. Taraschi, E. A. Fitzgerald, and D. A. Antoniadis, J. Vac. Sci. Technol. B 19, 2268 (2001).

11. L. M. Lee, W. C. Leitz, Z. Cheng, A. J. Pitera, G. Taraschi, A. D. Antoniadis, E. A. Fitzgerald, *Materials Research Society Symposium - Proceedings*, v 686, p 39-43 (2002)

12. E. Annastassakis, and M. Cardona, Semicond. Semimet. 55, 17 (1998).

13. E. Anastassakis, A. Cantarer, and M. Cardona, Phys. Rev. B 41, 7529 (1990).

14. D. J. Lockwood and J. M. Baribeau, Phys. Rev. B 45, 8565 (1992).

15. F. Pezzoli, E. Bonera, E. Grilli, M. Guzzi, S. Sanguinetti, D. Christina, G. Isella, H. von Kanel, E. Wintersberger, J. Strangl, and G. Bauer, J. Appl Phys. 103 (9), 093521 (2008).

16. M. Bauer, J. Taraci, J. Tolle, A. V. G. Chizmeshya, S. Zollner, D. J. Smith, J. Menendez, C. Hu, and J. Kouvetakis, Appl. Phys. Lett. 81, 2992 (2002).

17. G. He, and H. A. Atwater, Phys. Rev. Lett. 79, 1937 (1997).

18. A. H. Mahan, D. L. Williamson, and A. Madan, Appl. Phys. Lett. 44, 220 (1984).

19. V. R. D'Costa, C. S. Cook, A. G. Birdwell, C. L. Littler, M. Canonico, S. Zollner, J. Kouvetakis, and J. Menéndez, Phys. Rev. B 73, 125207 (2006).

20. J. Mathews, R. T. Beeler, J. Tolle, C. Xu, R. Roucka, J. Kouvetakis, and J. Menendez, Appl. Phys. Lett. 97, 221912 (2010).

21. J. Menéndez and M. Cardona, Phys. Rev. B 29, 2051 (1984).

22. P. Giannozzi, S. de Gironcoli, P. Pavone, S. Baroni, Phys. Rev. B 43, 7231 (1991).

23. P. A. Temple, C.E. Hathaway: Phys. Rev. B 7, 3685 (1973).

24. J.Kash, J.Tsang: in Light Scattering in Solids VI, ed. by M.Cardona, G.Güntherodt(Springer, Berlin) Vol. 68, p. 423 (1995).

25. A. Debernardi, S. Baroni, and E. Molinari, Phys. Rev. Lett. 75, 1819 (1995).

26. G. Deinzer, and D. Strauch, Phys. Rev. B 69, 045205 (2004).

27. J. Menéndez. Raman Scattering in Materials Science, volume 42. Springer, Berlin,(2000).

28. C. Kittel:Introduction to Solid State Physics (Wiley, New York 1996).

29. F.Cerdeira, C.J.Buchenauer, F.H.Pollack, and M.Cardona, Phys. Rev. B 5, 580 (1972).

30. M. Meléndez-Lira, J. Menéndez, W. Windl, O. F. Sankey, G. S. Spencer, S. Sego, R. B. Culbertson, A. E. Blair, and T. L. Alford, Phys. Rev. B, 54, 12866 (1997).

31. J. L. Martins, and A. Zunger, Phys. Rev. B 30, 6217 (1984).

32. Y. Cai, and M. F. Thorpe, Phys. Rev. B 46, 15872 (1992).

33. J. Menéndez, A. Pinczuk, J. Bevk, J. P. Mannaerts, J. Vac. Sci. Technol. B 6, 1306 (1998).

34. I. Aberg, C. Ni Chleirigh, and J.L. Hoyt, IEEE Trans. Electron Devices 6, 1021 (2006).

35. Materials Science in Semiconductor Processing, 11, 271, (2008).

36. O. Madelung, *Introduction to Solid-State Theory* (Springer-Verlag, Berlin, 1978).

37. A. Debernardi, and M. Cardona, Physica B 263-264, 687 (1999).

38. A. Debernardi, Solid State Communications 113, 1 (2000).

39. M. Chandrasekhar, J.B. Renucci, and M. Cardona, Phys. Rev. B 17, 1623 (1978).

40. M. Holtz, W.M. Duncan, S. Zollner, and R. Liu, J. Appl. Phys. 88, 2523 (2000).

41. J.F. Nye, *Physical Properties of Crystals* (Clarendon Press, Oxford, 1957)

42. P.Y. Yu and M. Cardona, Fundamentals of Semiconductors (Springer-Verlag, Berlin, 1966).

43. E. Anastassakis, A. Pinczuk, E. Bursten, F. H. Pollack, and M. Cardona, Solid State Commun. 8, 133 (1970).

44. F. D. Murnaghan, Proceedings of the National Academy of Sciences of the United states of America, 30(9), 244 (1944).

45. B. A. Weinstein, and G. J. Piermarini, Phys. Rev. B 12, 1172 (1975).

46. C.Ulrich, E. Anastassakis, K. Syassen, A. Debernardi, and M. Cardona, Phys. Rev. Lett. 78 (7), 1283 (1997).

47. H. J. McSkimmin, J. Appl. Phys. 24 (8), 988 (1953).

48. J. Z. Hu, L. D. Merkle, C. S. Menoni, and I. L. Spain, Phys. Rev. B 34 (7), 4679 (1986).

49. M. Balkanski, R. F. Wallis, and E. Haro, Phys. Rev. B 28, 1928 (1983).

50. L. H. Wong, C. C. Wong, J. P. Liu, D. K. Sohn, L. Chan, L. C. Hsia, H. Zang, Z. H. Ni and Z. X. Shen, Jap. J. Appl. Phys. 44, 7922 (2005).

51. S. Nakashima, T. Mitani, M. Ninomiya, and K.Matsumoto, J. Appl. Phys. 99 (5), 053512 (2006).

52. D Olego and M.Cardona, Phys. Rev. B 25 (2), 1151 (1982).

53. C.S. Menoni, J.Z. Hu, and I.L. Spain, Phys. Rev. B 34 (1), 362 (1986).

54. S. de Gironcoli, Phys. Rev. B 46, 2412 (1992).

55. O. H. Nielsen, and R. M. Martin, Phys. Rev. B 32, 3792 (1985).

56. M. Methfessel, C. O. Rodriguez, and O. K. Anderson, Phys. Rev. B 40, 2009 (1989).

57. M. Z. Hossain, and H. T. Johnson, J. Appl. Phys. 107, 073515 (2010).

58. F.K. LeGoues, B.S. Meyerson, and J.F. Morar, Phys. Rev. Lett. 66, 2903 (1991).

59. C. Y. Peng, C. F. Huang, Y. C. Fu, Y. H. Yang, C. Y. Lai, S. T. Chang, and C. W. Liu, J. of App. Phys. 105, 083537 (2009).

60. D. W. Jenkins and J.D. Dow, Phys. Rev. B 36, 7994 (1987).

61. K. Nishioka, T. Takamoto, T. Agui, M. Kaneiwa, and Y. Uraoka, Sol. Energ. Mat.Sol.C. 90, 1308 (2006).

62. J.R. Chelikowsky, and M. L. Cohen, Phys. Rev. B 14, 556 (1976).

63. M. Fox, Optical Properties of Solids (Oxford, New York, 2001), p. 63.

64. R. A. Soref, and L. Friedman, Superlattice Microst.14, 189 (1993).

65. Y. Ishikawa, K. Wada, J. Liu, D. D. Cannon, H. C. Luan, J. Michel, and L. C. Kimerling, J. Appl. Phys. 98, 013501 (2005).

66. Y. Huo, H. Lin, R. Chen, M. Makarova, Y. Rong, M. Li, T. I. Kamins, J. Vuckovic, and J. S. Harris, Appl. Phys. Lett. 98, 011111 (2011).

67. B. Y. Tsaur, J. C. C. Fan, and R. P. Gale, Appl. Phys. Lett. 38, 176 (1981).

68. J. C. Bean, T. T. Sheng, L. C. Feldman, A. T. Fiory, and R. T. Lynch, Appl. Phys. Lett. 44, 102 (1983).

69. S. Groves, and W. Paul, Phys. Rev. Lett. 11, 194 (1963).

70. L. Vegard, Z. Phys. 5, 17 (1921).

71. L. Pauling, The Nature of the Chemical Bond, Cornell University Press, Ithaca, 1967.

72. V. R. D'Costa, J. Tolle, C. D. Poweleit, J. Kouvetakis, J. Menendez, Phys. Rev. B 76, 035211 (2007).

73. R. Schorer, W. Wegscheider, and G. Abstreiter, J. Vac. Sci. Tech. B 11, 1069 (1993).

74. J. M. Zhang, M. Giehler, A. Gobel, T. Ruf, M. Cardona, E. E. Haller, and K. Itoch, Phy. Rev. B 57, 1348 (2004).

75. J. F. Kielkopf, J. Opt. Soc. Am. **63**, 987 (1973).

76. D. J. Lockwood, and Z. R. Wasilewski, Phy. Rev. B 70, 155202 (2004).

77. J. Kouvetakis, J. Menendez, and A. V. G. Chizmeshya, Annual Review of Materials Research 36, 497 (2006).

78. S. de Gironcoli, Phys. Rev. B 46, 2412 (1992).

79. S. F. Li, M.R. Bauer, J. Menendez, and J. Kouvetakis, Appl. Phys. Lett. 84, 867 (2004).

80. R. Carles, G. Landa, and J. B. Renucci, Solid State Comm. 53, 179 (1985).

81. V. R. D'Costa, J. Tolle, R. Roucka, C. D. Poweleit, J. Kouvetakis, and J. Menendez, Solid State Communications 144, 240 (2007).

82. P. Parayanthal, and F. H. Pollack, Phys. Rev. Lett. 52, 1822 (1984).

83. K. Park, Phys. Lett. 25A, 490 (1967).

84. A. S. Pine, and P. E. Tannenwald, Phys. Rev. 178, 1424 (1969).

85. T. R. Hart, R. L. Aggarwal, and B. Lax, Phys. Rev. B1, 638 (1970).

86. G. D. Pazionis, H. Tang, and I. P. Herman, IEEE J. Quantum Electron 25, 976 (1989).

87. R. Ostermeier, K. Brunner, G. A. Abstreiter, and W. Weber, IEEE Trans. Electron Dev. 39, 858 (1992).

88. R. Puchert, A. Barwolff, U. Menzel, A.Lau, M. Voss, and T. Elsaesser, J. Appl. Phys. 80, 5559 (1996).

89. R. Merlin, A. Pinczuk, and W. H. Weber, in *Raman Scattering in Materials Science*, edited by W. H. Weber and R.Merlin (Springer, Berlin, 2000), Vol. 42, p 12.

90. S. Baroni, S. de Gironcolli, and P. Giannozzi, Phys. Rev. Lett. 65, 84 (1990).

91. S. de Gironcolli, E. Molinari, R. Schorer, and G. Abstreiter, Phys. Rev. B 48, 8959 (1993).

92. H. H. Burke, and I. P. Herman, Phys. Rev. B 48, 15016 (1993).

93. J. Jimenez, E. Martin, A. Torres, and J. P. Landesman, Phys. Rev. B 58, 10463 (1998).

94. P. Verma, S. Abbi, and K. Jain, Phys. Rev. B 51, 16660 (1995).

95. R. F. Wallis and M. Balkanski, *Many Body Aspects of Solid State Spectroscopy* (North-Holland, Amsterdam, (1986)

96. K. Omote, J. Phys: Condens. Matter 22 (47), 474004 (2010).

97. J. C. Tsang, P. M. Mooney, F. Dacol, and J. O. Chu, J. Appl. Phys. 75 (12), 8098 (1994).

APPENDIX

PERMISSION FOR REPRINTS

From: **Permissions Europe/NL** <Permissions.Dordrecht@springer.com>
Date: Wed, May 25, 2011 at 4:20 AM
Subject: RE: reprint of two figures for my Ph.D. thesis
To: sbagchi@asu.edu

Dear Sampriti Bagchi,

With reference to your request (copy herewith) to reprint material on which Springer Science and Business Media controls the copyright, our permission is granted, free of charge, for the use indicated in your enquiry.
This permission
-allows you non-exclusive reproduction rights throughout the World.
-permission includes use in an electronic form, provided that content is password protected; at intranet;
-excludes use in any other electronic form. Should you have a specific project in mind, please reapply for permission.
-requires a full credit (Springer/Kluwer Academic Publishers book/journal title, volume, year of publication, page, chapter/article title, name(s) of author(s), figure number(s), original copyright notice) to the publication in which the material was originally published, by adding: with kind permission of Springer Science and Business Media.
The material can only be used for the purpose of defending your dissertation, and with a maximum of 100 extra copies in paper.
Permission free of charge on this occasion does not prejudice any rights we might have to charge for reproduction of our copyrighted material in the future.

Kind regards,
—
Maaike Duine
Springer
Rights and Permissions
—
Van Godewijckstraat 30 | 3311 GX
P.O. Box 17 | 3300 AA
Dordrecht | The Netherlands
tel
+31 (0) 78 657 6537
fax
+31 (0) 78 657 6377

maaike.duine@springer.com
-----Ursprüngliche Nachricht-----
Von: SpringerAlerts@springeronline.com
[mailto:SpringerAlerts@springeronline.com]
Gesendet: Sonntag, 15. Mai 2011 03:55
An: Holzhaus, Christoph, Springer Medizin DE
Betreff: reprint of two figures for my Ph.D. thesis

I would like reprints ofthe following two figures from the book ' Electronic Structure and Optical Properties of Semiconductors', page 92:

1) Energy versus wave vector diagram showing the electronic band structure of Ge

2) Energy versus wave vector diagram showing the electronic band structure of alpha-Sn.

Thank you
Sampriti Bagchi
Graduate student
Arizona State University, Tempe, AZ, USA

[Subject: reprint of two figures for my Ph.D. thesis
Sender name: Sampriti Bagchi
Sender email: sbagchi@asu.edu
Page name: Advertising & Corporate Sales Journals, Academic Books & Online Media | Springer
Page url: http://www.springer.com/advertisers?SGWID=0-110-12-69415-0]

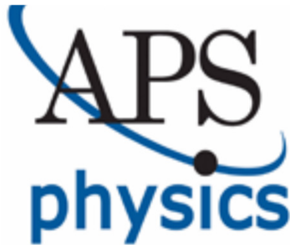

AMERICAN PHYSICAL SOCIETY
One Physics Ellipse, College Park, MD 20740 · http://www.aps.org
August 29, 2011
Sampriti Bagchi
sbagchi@asu.edu
Ref # 10532

Thank you for your permission request dated on August 24, 2011. We are pleased to grant you a non-exclusive, non-transferable permission, English rights, limited to **print and electronic format**, provided you meet the criteria outlined below. Permission is for a one-time use and does not include permission for future editions, updates, databases, translations, or any other matters. Permission must be sought for each additional use. This permission does not include the right to modify APS material.

Please print the required copyright credit line on the first page that the material appears: "Reprinted (abstract/excerpt/figure) with permission from [FULL REFERENCE CITATION] as follows: authors names, journal title, volume number, page number and year of publication. Copyright (YEAR) by the American Physical Society.

The following language must appear somewhere on the website: "Readers may view, browse, and/or download material for temporary copying purposes only, provided these uses are for noncommercial personal purposes. Except as provided by law, this material may not be further reproduced, distributed, transmitted, modified, adapted, performed, displayed, published, or sold in whole or part, without prior written permission from the American Physical Society."

Provide a hyperlink from the reprinted APS material (the hyperlink may be embedded in the copyright credit line). APS's link manager technology makes it convenient and easy to provide links to individual articles in APS journals. For information, see: http://link.aps.org/

You must also obtain permission from at least one of the authors for each separate work, if you haven't done so already. The author's name and address can be found on the first page of the published Article.

Use of the APS material must not imply any endorsement by the American Physical Society.

Permission is granted for use of the following APS material only Fig. 1, 4, Phys. Rev. B, Vol. 75, 1819 (1995)

Fig. 1, Phys. Rev. B Vol. 43, 7231 (1991)

Permission is limited to the single title specified or single edition of the publication as follows:

A PhD dissertation to be published by Sampriti Bagchi.

If you have any questions, please refer to the Copyright FAQ at: http://publish.aps.org/copyrightFAQ.html or send an email to Hassocpub@aps.org

Sincerely,

Eileen LaManca

Publications Marketing Coordinator

NATURE PUBLISHING GROUP LICENSE
TERMS AND CONDITIONS

May 22, 2011

This is a License Agreement between Sampriti Bagchi ("You") and Nature Publishing Group ("Nature Publishing Group") provided by Copyright Clearance Center ("CCC"). The license consists of your order details, the terms and conditions provided by Nature Publishing Group, and the payment terms and conditions.

All payments must be made in full to CCC. For payment instructions, please see information listed at the bottom of this form.

License Number	2674331120409
License date	May 22, 2011
Licensed content publisher	Nature Publishing Group
Licensed content publication	Nature Photonics
Licensed content title	High-performance Ge-on-Si photodetectors
Licensed content author	Jurgen Michel, Jifeng Liu and Lionel C. Kimerling
Licensed content date	Jul 30, 2010
Volume number	4
Issue number	8
Type of Use	reuse in a thesis/dissertation
Requestor type	academic/educational
Format	print and electronic
Portion	figures/tables/illustrations
Number of figures/tables/illustrations	1
High-res required	no
Figures	Figure 2: The effect of tensile strain on the band e of Ge. page 528
Author of this NPG article	no
Your reference number	
Title of your thesis / dissertation	Effect of anharmonicity on Raman-active phonons
Expected completion date	Jun 2011
Estimated size (number of pages)	200

Total 0.00 USD

Terms and Conditions

Terms and Conditions for Permissions

Nature Publishing Group hereby grants you a non-exclusive license to reproduce this material for this purpose, and for no other use, subject to the conditions below:

1. NPG warrants that it has, to the best of its knowledge, the rights to license reuse of this material. However, you should ensure that the material you are requesting is original to Nature Publishing Group and does not carry the copyright of another entity (as credited in the published version). If the credit line on any part of the material you have requested indicates that it was reprinted or adapted by NPG with permission from another source, then you should also seek permission from that source to reuse the material.

2. Permission granted free of charge for material in print is also usually granted for any electronic version of that work, provided that the material is incidental to the work as a whole and that the electronic version is essentially equivalent to, or substitutes for, the print version. Where print permission has been granted for a fee, separate permission must be obtained for any additional, electronic re-use (unless, as in the case of a full paper, this has already been accounted for during your initial request in the calculation of a print run). NB: In all cases, web-based use of full-text articles must be authorized separately through the 'Use on a Web Site' option when requesting permission.

3. Permission granted for a first edition does not apply to second and subsequent editions and for editions in other languages (except for signatories to the STM Permissions Guidelines, or where the first edition permission was granted for free).

4. Nature Publishing Group's permission must be acknowledged next to the figure, table or abstract in print. In electronic form, this acknowledgement must be visible at the same time as the figure/table/abstract, and must be hyperlinked to the journal's homepage.
5. The credit line should read:

   Reprinted by permission from Macmillan Publishers Ltd: [JOURNAL NAME] (reference citation), copyright (year of publication)

   For AOP papers, the credit line should read:

Reprinted by permission from Macmillan Publishers Ltd: [JOURNAL NAME], advance online publication, day month year (doi: 10.1038/sj.[JOURNAL ACRONYM].XXXXX)

6. Adaptations of single figures do not require NPG approval. However, the adaptation should be credited as follows:

   Adapted by permission from Macmillan Publishers Ltd: [JOURNAL NAME] (reference citation), copyright (year of publication)

7. Translations of 401 words up to a whole article require NPG approval. Please visit http://www.macmillanmedicalcommunications.com for more information. Translations of up to a 400 words do not require NPG approval. The translation should be credited as follows:

   Translated by permission from Macmillan Publishers Ltd: [JOURNAL NAME] (reference citation), copyright (year of publication).

We are certain that all parties will benefit from this agreement and wish you the best in the use of this material. Thank you.

Special Terms:

v1.1

Gratis licenses (referencing $0 in the Total field) are free.

Please retain this printable license for your reference. No payment is required.

If you would like to pay for this license now, please remit this license along with your payment made payable to "COPYRIGHT CLEARANCE CENTER" otherwise you will be invoiced within 48 hours of the license date. Payment should be in the form of a check or money order referencing your account number and this invoice number RLNK10991564.

Once you receive your invoice for this order, you may pay your invoice by credit card.Please follow instructions provided at that time.

Make Payment To:
Copyright Clearance Center
Dept 001
P.O. Box 843006, Boston, MA 02284-3006

For suggestions or comments regarding this order, contact Rightslink Customer Support: customercare@copyright.com or +1-877-622-5543 (toll free in the US) or +1-978-646-2777.